Flexible Fiber-Shaped Supercapacitor for Wearable Electronics

Doctoral Dissertation
Doctoral Program in Material Science and Technology (31st Cycle)

Flexible Fiber-Shaped Supercapacitor for Wearable Electronics

Amjid Rafique

* * * * * *

Supervisor
Dr. Andrea Lamberti

Doctoral Examination Committee:
Dr. Alessandra Sanson CNR Faenza, Italy.
Dr. Francesco Lufrano, CNR Messina, Italy
Dr. Doriano Brogioli, Bremen University, Germany
Dr. Simone Marasso, CNR Parma, Italy.
Dr. Paola Prete, CNR Lecce, Italy.

Politecnico di Torino
November 15,2018

I hereby declare that, the contents and organization of this dissertation constitute my own original work and does not compromise in any way the rights of third parties, including those relating to the security of personal data.

…….....

Amjid Rafique

Turin, November 15,2018

Abstract

The depleting natural resources and ever-increasing needs of energy led to environmental issues which attract immense attention of the researchers for future technology advancement in the field of energy conversion and storage. The supercapacitor also known as electrochemical capacitors (SCs), being a part of the electrochemical energy storage devices, attracted great attention owing to it high power delivery > 100 time higher than battery, long cyclic life >10^5 and high efficiency. In recent year some flexible wearable electronics have evolved in leaps and bounds and emerged as new market of portable and wearable electronics. To meet the requirement of this new market, fiber shaped SCs have been considered among flexible and stretchable solutions. This dissertation presents the fabrication, electrochemical performance testing and performance optimization of different flexible substrates for fiber shaped SCs. Nanoscale materials offer advanced and exciting fabrication techniques of SC electrodes for high-performance electrochemical energy storage devices. In material science, major challenge is to synthesize the nanomaterials with desirable chemical properties and to engineer the nanostructures in an appropriate way.

This thesis exhibits the successful fabrication and applications of very promising materials in electrochemical SCs for energy storage, including ZnO/Graphite composite, manganese dioxide deposition on carbon fibers (CFs), Fe_2O_3 composite with rGO aerogel and MoS_2. The prime objective is to understand their synthesis processes and electrochemical performance in supercapacitor devices. First of all, two parallel electrode configuration devices were assembled in gel-polymer electrolyte using ZnO/graphite as active material dip-coated on copper wire. The assembled device exhibits excellent performance as compared to bared graphite powder-based electrode in term of specific capacitance, energy and power density. The cyclic and bending stability has also been evaluated. Moving towards flexibility, other flexible substrates, transition metal oxides and their composites are

investigated as electrode material for SCs. Here, CFs were selected as flexible substrate and MnO_2 as active material. MnO_2 is electrodeposited (ED) on CFs using both potentiostatic and galvanostatic techniques. After comparing electrochemical performance, best performing deposition technique (galvanostatic deposition) was optimized by tuning deposition parameters such as, time and current density. The morphology of the nanostructures and their electrochemical performance (specific capacitance, cycling effects and bending stability) which contribute to the understanding of the energy storage mechanism of MnO_2 based SCs is thoroughly investigated. In addition to single step deposition, the performance of MnO_2 on CFs (MnO_2/CF) electrode is further improved using 2-step ED of MnO_x by achieving the full coverage of the substrate and connectivity of the nanostructured material. The performance of the material was also improved by introducing oxygen vacancies on the MnO_x surface by hydrogenation process (obtaining Mn_3O_4) and subsequently optimized by electrochemical conversion of this spinel structure into Sodium Birnessite. Electrochemical performance and energy density of the supercapacitor is also enhanced by exploiting asymmetric configuration of the device in PVA based gel-polymer electrolytes. In this dissertation two asymmetric devices are assembled: i) MnO_x/CF and Fe_2O_3/rGO, ii) H-MnO_x and MoS_2 with former as positive electrode and later as negative material respectively. Both the devices have shown excellent electrochemical performance along with wide voltage windows 1.2 V and 1.8 V respectively which is fundamental for high energy density devices. The synthesis of electrodes described in this thesis exploiting electrodeposition technique is simple, cost effective, and environmental friendly approach. It possesses great potential to fabricate low-cost and high specific energy density SCs.

Acknowledgment

Summarizing few things in the acknowledgement is apparently a difficult task. Nevertheless, this is probably the most suitable place to thank most of the contributor who continuous motivated me during the whole PhD candidature.

First and foremost, I express my deepest gratitude to Andrea Lamberti for his kind supervision during my doctoral period. His clairvoyance on physical and chemical phenomenon and its rigorously related theoretical concepts, has substantially influenced me in scientific field. I am grateful for his kind guidance, patience discussion and valuable suggestions carrying out my thesis research during entire course of my PhD study. I have been really very fortunate to work with him. His hardwork, enthusiasm and endless quest to perform high quality research influenced me deeply and set a great benchmark for my career.

I want to express my immense gratitude to “Higher Education Commission of Pakistan” for financial support throughout my doctoral studies and provide an enormous platform to begin my research career.

I also would like to extend my gratitude to the DISAT (Material Science and Technology department), nano-science laboratory (Materials and Microsystems group): Paola and Alesandro and electrochemical characterization lab.

Appreciation also goes to following people for their constant support and valuable contribution: Stefano Bianco, Marco Fontana, Mara Serrepede, Andrea Massa, Simeleys Hernandez for results and discussions.

Special thanks to all my friends in Politecnico di Torino, Alberto, Pietro, Tayyab, Umair, Umer, Usman, Yasir and office colleagues.

Finally, without tremendous support of my family, it was inevitable to complete my doctoral studies. Countless regards to my late parents, wife Zakia,my daughter Yashfa, brothers (Zahid, Sajid, Majid), sisters (Sobida,Noreen) and parents in laws. My parents always support me and respect my choices; they give me love and support unconditionally. My wife always supports and encourages me and stood by through thick and thin. My brother Dr. Abid, he is so kind, patient and lovely, and inspires me to complete this work and make my dream in reality.

Amjid Rafique
Turin, 2018.

To my late parents (Muhammad Rafique and Ulfat Jan),
my family members especially my wife,my daughter and
my brother Dr. Abid Rafique.

List of Tables

List of Figures

Contents

Chapter 1 Motivation

"Imagination is more important than knowledge,
knowledge is limited. Imagination encircles the world".
— Albert Einstein.

1.1 Introduction

Owing to ever-expanding oil based global economy and the explosive growth rate of the population, world natural resources are depleting at greater rate. The greatest challenge of 21st century for scientific community and policy makers, is to explore new innovative, sustainable, eco-friendly alternative energy resources. One of the biggest problems related to fossil fuel is environmental pollution [1]. Therefore, there is a need to use these energy resources in an efficient and effective ways and explore alternative sources of renewable and sustainable energy. Flexible wearable, bendable, stretchable are the most common terminologies of the recent era which may intensely change one's interaction interfaces without impacting living patterns in the very near future.

In recent years, research in the field of flexible, bendable and stretchable electronic devices is blooming gradually in smart textiles or e-textiles. Particularly, in the current scenario, these wearable electronic devices are in high demand, especially in biomedical field, which presents an excellent opportunity to design and fabricate wearable devices towards predictive analytics and treatments [2], [3]. In the last decade, a new market of electronics has emerged and trending towards miniaturization, flexible, lightweight and portable electronics suited for some specific applications [4] such as laptop computer systems, mobile phones, tablets, sensors network etc. Energy storage system's characteristics have critical influence on the operability of these trending portable smart devices and greatly depends on the convenience of the storage system with eloquently enhanced energy and power density, robustness and low cost. But, the current flexible SCs are generally based on planar structures [5],[6] which are hefty and large, and difficultly meet the energy needs of portable electronics. Recently, fiber shaped SCs in the form of two twisted fiber electrodes have been explored extensively, since they can be easily woven or knitted into electronic clothes for wearable electronics [7].

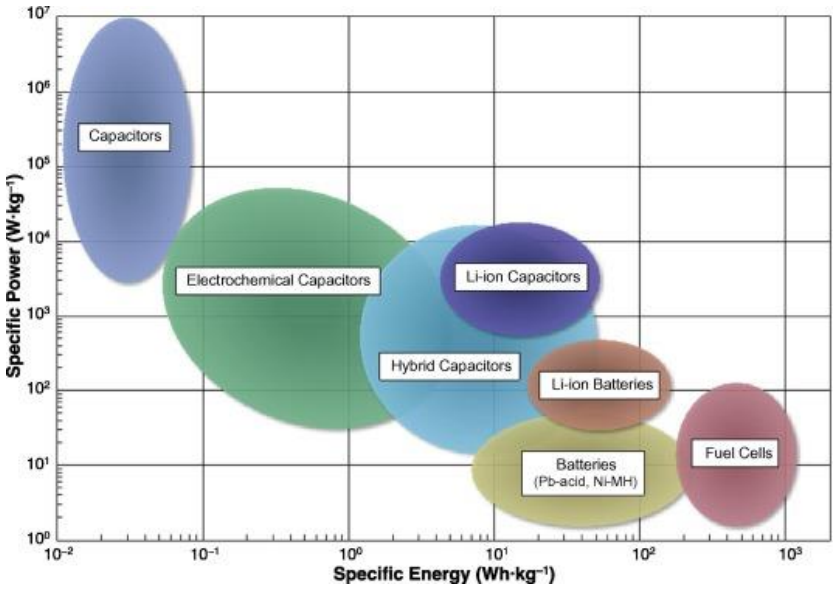

Figure.1 Ragone plot for different energy storage devices (Reproduced copyright permission) [8]

Due to faster dispensation of data (one of the key objectives of the of the portable electronics), they required more and more electronics components to process and transmit data, resulting in high power demand. Therefore, high power i.e. high delivery rate, has shorten the battery run time (the time electronic device will run before it must be recharged). But consumers want batteries to run for longer time. To solve this problem, SCs, also called electrochemical supercapacitors (ECs), can offer a complementary solution for power sources, thanks to their high-power throughput, longer cyclic life (>100000) cycles and excellent reversibility (90-95 %) [9]–[11].

SCs are divided into two main categories based on their charge storage mechanisms; electric double layer supercapacitors (ELDCs) which is normally observed in carbon based active material in which charge stored through physical adsorption and desorption at the interface between electrode and electrolyte. Second type is pseudocapacitors (PCs), which stored charge through Faradaic redox reaction and give higher specific capacitance due to intercalation/deintercalation of the of ions contained into the electrolyte. This phenomenon is observed in transition metal oxide and its composites with some carbonaceous material such as activated carbon, carbon nanotubes, carbon nanodots and graphene etc.

Ragone plot, obtained for energy storage devices, allows a comparison in terms specific energy and specific power as shown in the figure 1.1. It is clear from the plot that conventional capacitor shows higher power (> 10^6 W/ kg) if compared to conventional battery and fuel cell but lower energy density than battery and fuel cell. ECs have higher energy density then conventional capacitor because conventional capacitors store charge on low surface area while SCs store charge in EDL setup by ions adsorption/desorption at the interface between high specific surface area carbon based electrodes and electrolyte [1]. It is also found that ECs deliver thousands of times higher power than battery of similar size [9]. Eccentric charge

storage mechanisms in SCs, electrostatic in case of EDLCs (fast and reversible) and Faradaic (highly reversible redox) in case of pseudocapacitive gives SCs much longer cyclic life (>10^5 cycles) than conventional batteries which needs higher charging time with limited cyclic life(<750 cycles) [12]. In other word, SCs find a special position in Ragone plot in terms of both energy and power density respectively and bridges the gap between both conventional capacitor and batteries [1], [8], [12].
SCs, because of these distinctive properties have diverse applications:

I. Major portion of commercial SCs are used in consumer electronics, where they mainly aid as backup power source for different systems such as, memories, microcomputers and smart watches.
II. Short terms Power source for electrical vehicles, hybrid electrical vehicles, toys and starter application
III. Supercapacitors are used as an alternative power source for flexible portable electronics such as sensors, antennas, LED's and artificial skins etc.

1.2. Research objectives

In order to fulfill the power demands of portable and wearable electronics, fiber shaped flexible SCs attracting immense attentions of scientific community and researchers in the recent past. However, because of new emerging technologies and flexible electronics, existing commercial SCs fail to meet the intended market requirements because of its rigidity. Although, development of flexible fiber shaped SCs still a challenge which are compatible with flexible portable/wearable electronics. This challenge arouses a research question for scientific community that, is it conceivable to develop a complete package in form of flexible and wearable SCs? The research question can be divided into two sub-domains:

1. how to design and configure a flexible fiber shaped SCs?
2. how to fabricate high performance flexible fiber shaped electrodes and assemble SCs?

This research is mainly focusing on the design and optimization of the configuration of the green flexible electrode materials for cost-effective wearable SCs devices. Flexible wire and fiber shaped SCs were fabricated, characterized and their performance optimized using different active materials. The main objectives of this research activity were:

1. Exploring different kind of flexible substrate and optimizing the performance of the SCs
2. Synthesizing low cost materials to develop a cost-effective SCs

3. Designing different configuration (symmetric and asymmetric) to increase the specific performance of the SCs
4. Exploiting (symmetric and asymmetric) configurations of the solid state SCs to increase the working voltage windows and specific energy.

1.3. Organization of the dissertation

This dissertation is divided in 6 chapters. Starting from motivation of the research, main objectives of this PhD thesis project are discussed in Chapter 1.

Chapter 2 contains a literature review about the history of SCs, fundamental working principles, types of electrode materials, types of substrate and applications as well as the advancement trends of the SCs. The current advancement on the flexible and wearable SCs are also reviewed in this chapter.

Chapter 3 presents the design, fabrication and characterization of flexible wire-shaped SCs in which ZnO/graphite composite used as active material in symmetric configuration with gel-polymer electrolyte. The electrochemical performance of this kind of wire-shaped SCs is investigated under flat and bending conditions at different stress levels.

Chapter 4 is focused on electrodeposition (ED) of nanostructured manganese oxides and it is divided into three main subsections. Section 4.1 described the synthesis of MnO_2 on CFs, exploiting different electrochemical techniques (galvanostatic & potentiostatic), investigating the effects of key practical factors such as current density and time of deposition. The effect of calcination temperature on the morphology is also investigated. The electrochemical performance of the MnO_2/CF composite electrodes is probed including bending and cyclic stability at different stress level in symmetric conditions with gel-polymer electrolyte.

Section 4.2 presents the investigation of the two-step ED of the MnO_x on the CFs to enhance the electrochemical performance including investigation of effects of switching the step of deposition, time of deposition and effect of current densities on morphologies of the MnO_x.

Section 4.3 describe some optimization of the MnO_x electrodes. The synthesis of Mn_3O_4 by using hydrogenation process and sodium Birnessite using electrochemical activation of the Mn_3O_4 spinel structure was also discussed. In this section, the electrochemical performance of all the electrodes was evaluated using three-electrode electrochemical measurements.

Chapter 5 is focused on asymmetric devices and it is also divided into two subsections. Section 5.1 provides detailed information about asymmetric configuration of SCs devices fabrication exploiting 2-step ED MnO_x as positive and rGO/Fe_2O_3 as negative electrode material respectively. I have in detail discussed the green synthesis of rGO/Fe_2O_3 composite and have also analyzed electrochemical performance and its cyclic and bending stability.

Section 5.2 presents detailed study about fabrication of a device in an asymmetric configuration, using $H\text{-}MnO_x/CF//MoS_2/CF$ as positive and negative electrode materials respectively. I have evaluated the electrochemical performances of the both the devices in asymmetric configuration and its cyclic and bending stability. These results are very important for flexible fiber shaped SCs design, and optimization of the SCs performance. The structure of fiber shaped SCs and preparation methods are further improved to high performance SCs.

Last but not the least, in chapter 6, the main conclusions of the study and suggestions for future work are outlined.

Chapter 2 Literature review

"One never notices what has been done;
one can only see what remains to be done".
— Marie Curie.

2.1 Background

Owing to fast depletion of global natural resources and serious environmental problems, researchers are focusing on not only new energy resources to replace these conventional means but also new energy storage devices. Countless efforts have already been done to find new solutions to these energy storage problems, such as hybrid power system, chemical cells and fuel cells. However, still there are lot of challenges to realize their commercial applications such as, high cost, short lifecycle and low temperature performance. SCs, also known as ultracapacitors or electrochemical supercapacitors, are believed to be propitious candidates for storing energy owing to their characteristic features such as high-power density, excellent cyclic stability, low equivalent series resistance (ESR), superior rate capability, high temperature performance and environmental benevolence [13],[14]. However, the restriction of surface charge storage (or near surface) make their energy density much lower than batteries which may not substitute the conventional energy storage system, but can work as complementary to these conventional energy storage systems such as batteries [15].

The concept of the double layer (DL) has been investigated by chemists in 1853, when Hermann von Helmholtz, first modelled and developed the DL concept in investigations on colloidal suspensions. He has used the Faraday's laws to solve the problem of the charge storage mechanism. It leads way for the advancement of fundamental features in capacitive technology and a quantitative science of unfolding the nature of electrostatic behavior [16]. But it was 1957, when the first patent was filed by H. I. Becker at General Electric Corporation (GE), on double layer capacitor (DLC) ECs in which porous carbon was used as active material [17]. Another device was assembled using same porous carbon as electrode material in non-aqueous electrolyte by Standard Oil Company, Cleveland, Ohio (SOHIO) in 1962, and registered a patent. It was recognized that "DL at the interphase between electrode and solution acts like a capacitor of comparatively high specific capacitance"[18]. Another disc like capacitors with electrolyte-soaked carbon paste as an active material separated by an ion-permeable separator was patented by SOHIO 1970 [19]. Later in 1971, SOHIO licensed this DL capacitor technology to a Japan based Nippon Electric Company (NEC). NEC was able to efficaciously manufacture the first commercially DLC and marketed it as

"supercapacitor". Although SCs at that time had a very restricted applications and were mostly used as back-up power supplies for volatile computer memories or clock chips [16]. The capacitance performance of early generations of SCs were mainly hindered by high internal equivalent series resistance (ESR), due to the low conductivity of electrolytes and electrodes [20]. By that time, the industry scale growth of the SC had started with the development of key technologies. These problems were solved by improving the electrolyte, electrode materials and the engineering process. The Pinnacle Research Institute (PRI) developed the first high power DL capacitors named "PRI Ultracapacitors" by integrating metal-oxide in the electrode in 1982, which is mainly designed for military applications. In era of late 70's and 80's, Brain Evan Conway, a researcher at university of Ottawa, made a countless contribution to the SCs research, exploiting RuO_2 as the active material which exhibited a high specific capacitance and a low ESR [21],[22]. This material (RuO_2) store charges electrostatically (EDL) and also thanks to another phenomenon called "pseudo capacitance" resulting from faradaic reaction or underpotential deposition on the surface of electrodes. Owing to his research, the concept of SCs has been into new era, and Conway et al. elucidated the transformation between batteries and SCs in 1991 [23].
Recently, SCs are used as power sources for several fields such as, mobile phones, communication devices, digital cameras, electric hybrid vehicles, pulse laser procedures, power supplies for computers, back-up power for RAM (random access memory) devices and storage for energy harvesting by photovoltaics [13].

2.2. Charge storage mechanisms

2.2.1 Conventional capacitor

Capacitors are important electrical circuit components that store energy in the magnitude of microfarads and help in filtering. Capacitors serve two main tasks; i) charge or discharge of electricity, employed for smoothing of circuit variations of power supplies, back-up circuits of computers, ii) blocking of the DC current to eliminate or extract specific frequencies [13].
Conventional dielectric capacitors comprise of two parallel metallic plates shown in Figure 2.1 and to avoid the contact between these plates an insulating dielectric material called a "separator" is interjected between them.

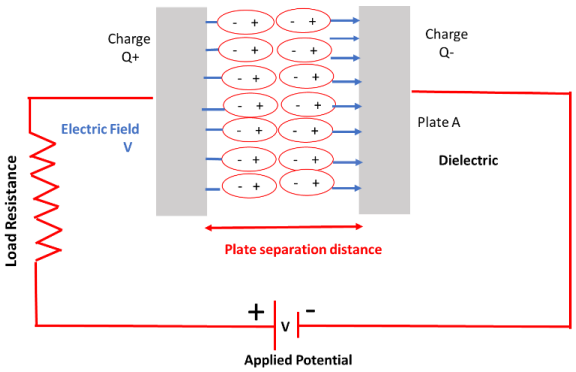

Figure 2.1 Schematic of a conventional capacitor.

When there is a potential difference across the electrode plates, a static electric field develops across the dielectric layer, leading to opposite charge accumulation on respective plates. That is the way in which a capacitor stores energy in the electrostatic field [19].

Capacitance C (F) of the electrolytic capacitor is defined as the proportion between positive charge stored Q (C) to the applied potential (V) [24]

$$C = \frac{Q}{V} . \qquad 2.1$$

For a capacitor capacitance C is directly proportional to area A (m^2g^{-1}) of each electrode and inversely proportional to the distance D (m) between electrodes [24], product of $\mathcal{E}o \text{ and } \mathcal{E}\gamma$ are the constant of proportionality and $\mathcal{E}_0$ (Fm^{-1}) is a dielectric constant or permittivity of free space and $\mathcal{E}\gamma$ is the dielectric constant of the separator between two electrodes

$$C = \mathcal{E}o\mathcal{E}\gamma \frac{A}{D} . \qquad 2.2$$

Conventional capacitors have comparatively high-power densities, but low energy densities, when compared to batteries and fuel cells as shown in Figure1.1. On other side, battery can store higher energy density than a capacitor, but there is a problem with battery since their energy delivery is very low, which corresponds to low power density. In contrast, although capacitors store relatively less energy per unit mass or volume, they have very high discharge rate and hence delivery rate of power density very high [15], [25], [26].

2.2.2 Electrochemical capacitors (supercapacitor)

The fundamental working principle for conventional capacitors is also true for SCs as shown in Figure 2.2 which is same as of schematic of conventional

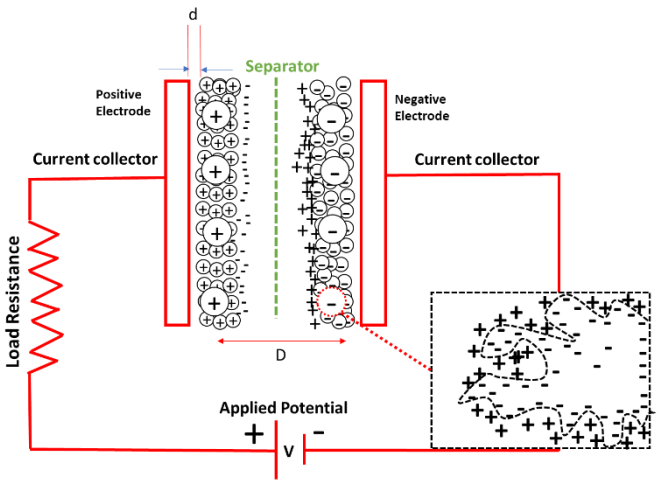

Figure 2.2 Schematic of electrochemical double layer capacitors

capacitors (Figure 2.1). SCs also comprise of two electrodes separated by a separator. The main difference between them is that, SCs electrodes normally have much higher specific surface areas than those for conventional capacitors electrodes, and an electrolyte solution in a separator between them. This leads to the formation of the so-called EDL formation during charging step separated by the distance D. Therefore, SCs have higher specific capacitance and energy density than conventional capacitors due to much higher surface area A and smaller distance D between two charge layers.

2.2.3 Type of SCs

SC is a generic term used for different types of ECs. The basic working principle of SCs is based on the storage and delivery of the ions coming from the electrolyte

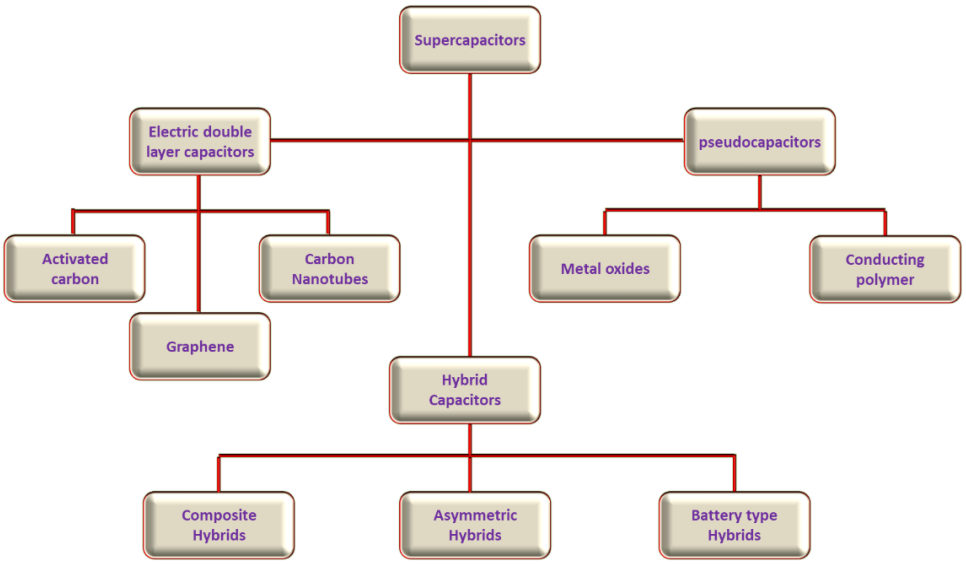

Figure 2.3 Taxonomy of SCs

onto the surface of the electrodes as shown in the Figure 2.2. According to the energy storage mechanism supercapacitors are divided into three classes: electrochemical double-layer capacitors, pseudocapacitors, and hybrid supercapacitors [27] as shown in figure 2.3**.**

2.2.3.1 Electric double layer capacitors

The design and fabrication of the EDLC is similar to batteries. It consists of two electrodes (usually carbon-based on metallic current collectors), an electrolyte and ion permeable separator enclosed in suitable package [10] as shown in Figure 2.4. The concept of EDL was first coined and modelled by Helmholtz, when he studied the distribution of opposite charges formed at the interface between electrode/electrolyte which are at an atomic distance from each other as shown in Figure 2.5a. This model is same as two plate conventional capacitor. This model was further studied and improved by Gouy and Chapman by considering the continuous distribution of anions and cations of the electrolyte driven by thermal motion, named as diffusion layer (DL) as shown in Figure 2.5b which leads to overestimation of the EDL capacitance.

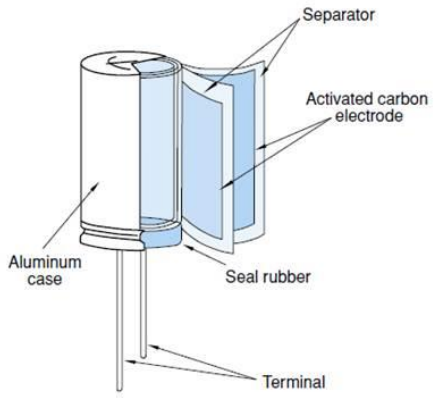

Figure 2.4 Schematic of EDLC adapted [Tecate group website]

As the capacitance increases inversely with distance (separation between two electrodes), charges close to the electrode surface exhibit higher capacitance as compare to distance charges [28], [29]. Later, Stern came with new solution by combining these two models and present a new model. In his model, he recognized two regions of electrolyte ions distribution, named inner line a compact layer (because of very strong absorption of ions) and outer line as diffusion layer as shown in Figure 2.5c [30]. He introduced two new terms, inner Helmholtz plan (IHP), the distance of closest approach of specifically adsorbed ions (generally anions) and outer Helmholtz plan (OHP) are non-specifically adsorbed ions, d is the DL distance defined by the Helmholtz model. It is clear from the Figure 2.6 that, during charging process, the electrons move from negative to positive electrodes

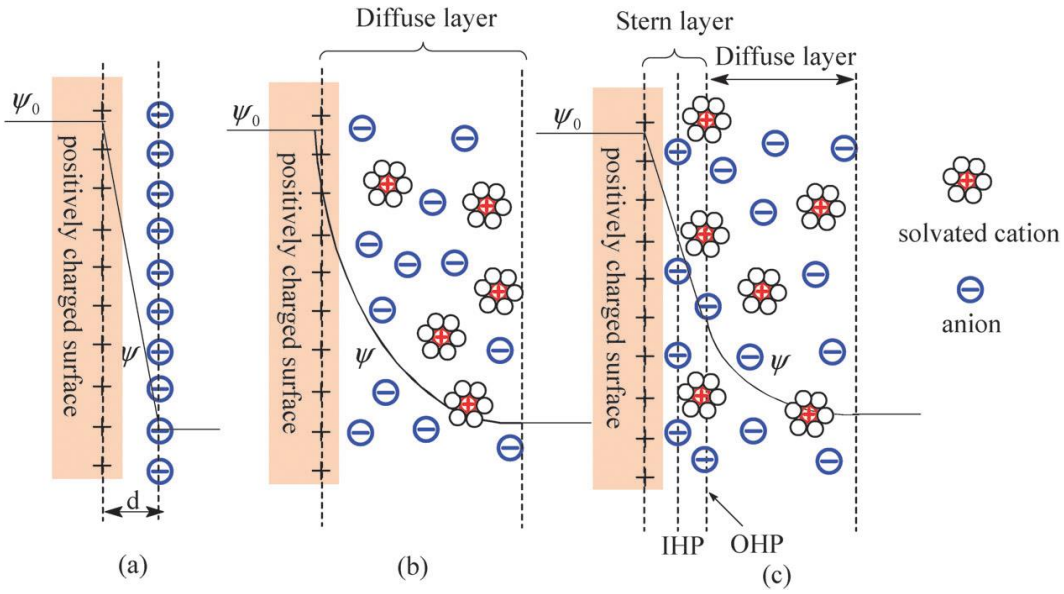

Figure 2.5 Models of the EDL: a) the Helmholtz model, b) the Gouy–Chapman model, c) the Stern model, showing the inner Helmholtz plane (IHP) and outer Helmholtz plane (OHP). (Reproduced copyright permission) [28]**.**

through external load. The electrolyte ions (cations/anions) will accumulate electrostatically at the respective electrodes surfaces and create DL to offer electroneutrality of the SCs [9], [13]. This EDLCs thickness will be influenced by many factors such as, size of electrolyte ions, electrolyte concentration, the solvent in which electrolyte dissolved, chemical affinity between the electrolyte ions and electrode surface [28], [31]. The thickness of the EDL can be quantified by the Debye length λ_d according to the expression 2.3 [31],

$$\lambda_d = K^{-1} = \sqrt{2e^2 c_o / \mathcal{E}\mathcal{E}_o k_B T} \qquad 2.3$$

This Debye length gives characteristic length by which thickness can be calculated. The Debye length plays a critical role in determining the size of EDL's and indicate how much charge can be stored. At low electric potential, the formula to calculate EDL is same as of two parallel plate capacitor described in equation 2.2 where d represents effective thickness of the EDL (Debye length) [28]. As there is low applied potential across the two electrodes, no chemical reaction occurs, and charge storage is non-Faradaic leaving no chance of swelling of active material like batteries during charging and discharging. The most common carbon-based materials used in EDLC are activated carbon, porous carbon, carbon nanotube and graphene oxide [32], [33]. In summary, carbon electrode materials with high surface area will lead to enhanced specific capacitance and energy density, as compared to conventional capacitors [10] but still lower than batteries.

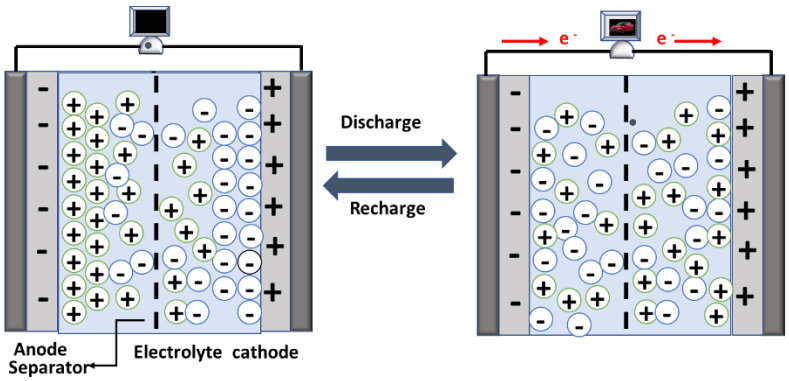

Figure 2.6 Charging and discharging of the electric double layer SCs

2.2.3.2 Pseudocapacitors

PCs is another type of SCs which, compared to electrostatic charge storage of EDLCs, store charges through Faradic reactions. In this charge storage mechanism transfer of charge between electrode and electrolyte is involved [34]. Once a voltage is applied to a PCs, redox reaction occurs on the electrode material, which undergo the passage of ions across the DL, resulting in Faradic current passing through the SCs cell. According to Zhang et al. [35] several Faradaic processes may occur such as: i) under potential adsorption, ii) redox pseudocapacitance (PC), iii) intercalation PC as shown in Figure 2.6 by an example [36]. Underpotential adsorption mechanism observed, when monolayer of electrolyte cation is adsorbed on the active material surface as demonstrated in Figure 2.7 a. The second type of redox PC will happen, when electrolyte species are electrochemically adsorbed on the surface or near surface of active material with an affiliated Faradic-charge transfer as shown in Figure 2.7b. The final type as shown in Figure 2.7c, intercalation PC is observed, when electrolyte ions insertion happens into the tunnels of electrode materials convoyed by a Faradic-charge transfer with-out any crystallographic phase transition. The occurrence of these redox processes will be influenced by physical procedure, electrode morphology and composition. These types of faradic processes are normally observed in transitional metal oxides or conductive polymers which offer them to attain greater specific capacitance and energy densities as compared to typical EDLCs. This shows that in a single electrode both the mechanism can be observe at the same time. PCs like batteries gave higher energy density but suffer with power density and cyclic stability if compare to EDLCs. Thus, this field has great potential for scientists to investigate and explore new affordable and suitable active materials for enhancing the performance of pseudocapacitive materials and device performance.

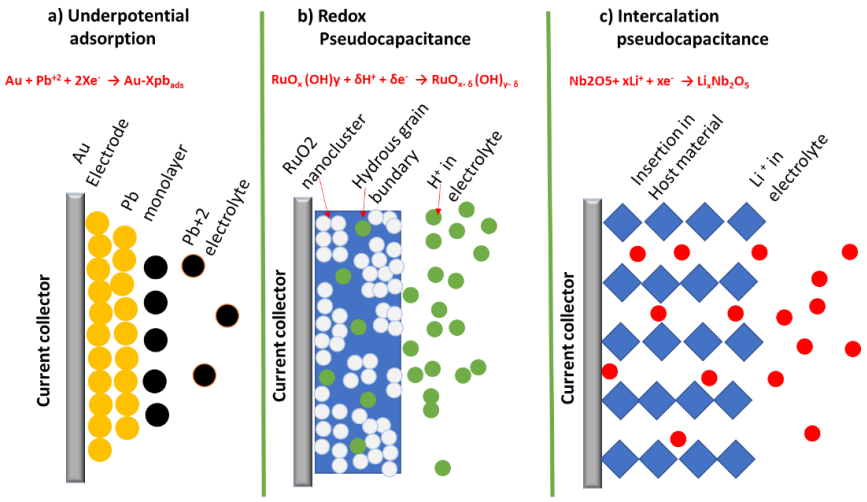

Figure 2.7 Various types of redox mechanisms in PCs: a) underpotential adsorption, (b) redox PC, (c) intercalation PC. (Reproduced copyright permission) [32].

2.2.3.3 Hybrid supercapacitors

EDLCs provide excellent cyclic stability, good high-power delivery while in the case of PCs, they provide superior specific capacitance. If we want to exploit characteristics of both EDLCs and PCs, we need to combine them, achieving the energy source of battery-like material, with a power source of capacitor-like electrode in a single cell [37]. With a precise electrode materials blend, except EDLCs and PCs, there exists another kind of SCs which is called, hybrid-capacitors. The battery-type Faradaic electrode materials in a hybrid device offer enhanced energy density for couple of reasons: firstly, the electrodes can function over double the voltage window range as compared to simple double-layer Carbon/Carbon capacitor, therefore we have double the charge stored in the hybrid device for the same amount of carbon material. Secondly, the battery-type electrode material prejudices the potential of the hybrid cell around that of its electrochemical potential. Hybrid capacitors are classified into three different categories based on electrode configuration: i) composite, ii) asymmetric, iii) Battery-type hybrid.

Composite electrodes

In composite electrode fabrication, carbon-based materials are normally combined with either transition metal oxides or conducting polymers in one electrode, resulting in an electrode working by both electrostatic and electrochemical charge storage mechanisms [24]. Recently, two different types of composites have been reported in literature: binary and ternary composites. binary composites comprise two different electrode materials carbon material and metal oxide or hydroxide [38], while in ternary case, it employs three different electrode materials to fabricate one electrode normally consists of carbon material, metal oxide/hydro-oxide and conducting polymer [14].

Asymmetric hybrid SCs

Asymmetric hybrid SCs are fabricated from two different supercapacitor-type electrodes, one electrode being of a EDL material and the other being of a PC material. In precise, the coupling of negative electrode (activated carbon) with a positive electrode (conducting polymer) has attracted countless attention by the researcher [39]–[41]. The dearth of an efficient, negatively charged, conducting polymer material has restricted the success of CP based pseudocapacitors. As conductive polymers-based electrodes have low energy density than EDLC's because of low conductivity of the conductive polymers, so this problem is tackled by designing a hybrid supercapacitor in which activated carbon is used as negative electrode and conductive polymer as positive [41] to attain higher energy and power densities than EDLCs.

Battery-like hybrid supercapacitors

As for asymmetric hybrid supercapacitors, battery-like hybrid supercapacitors are fabricated by coupling two dissimilar electrodes; but battery-like hybrid are distinctive in coupling a SCs electrodes with a battery electrode. This particular arrangement echoes the demand for high energy SCs and high-power batteries, by mingling the energy features of batteries with the cyclic life, power density and charge/ discharge time of SCs. Recently, researchers are focusing mostly on using $Ni(OH)_2$, PbO_2, and $Co_xNi_{1-x}(OH)_2$ as one electrode and rGO as the other [42]–[46]. Nowadays not many data are available on battery-like hybrid SCs as compare to other type of SCs, but the available data recommends that these hybrid SCs may be possible solution to cover the gap between SCs and batteries as shown in Ragone plot in Figure 1.1. In spite of the convincing research outcomes, the common agreement is that more focus studies will be essential to discover the full potential of battery-like hybrid SCs [42], [43].

2.4. Basic tools for SCs performance evaluation

Various test methods have been devised and applied to measure the electrochemical performance of SCs such as Cyclic voltammetry (CV), constant current charge/discharge (CCCD). All these tools are used to measure specific capacitance, ESR, energy density, power density.

2.4.1. Cyclic Voltammetry (CV)

CV characterization employ a linear changed of potential between negative and positive electrodes in two electrodes device or between working electrode and

reference electrode in case of three electrodes system. The rate of change of potential is measured in mV s^{-1} is (called sweep rate or scan rate) and denoted by, "v" and the potential between two extremes, is called voltage window or operational potential window. In cyclic voltammetry measurements, a current response is recorded against constant rate of potential is applied, during anodic and cathodic sweep to characterize the involved electrochemical reactions. The data obtained are usually plotted in graphs plotted as current (A) vs potential (V) as shown in the Figure 2.8 [47].

To study the charge storage mechanisms of SCs electrode materials where EDLC and PC types are different from each other in electrochemical behavior, CV testing with the three-electrode setup is observed as the most suitable technique [47], [48]. The qualitative analysis can be done by simply analyzing the shape of the CV:

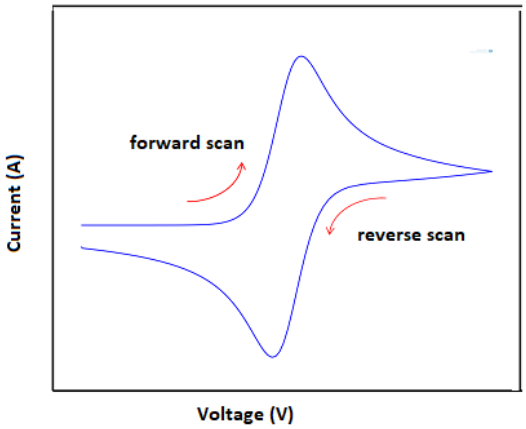

Figure 2.8 Typical cyclic voltammetry

rectangular shape is the representative of the EDLCs and shapes with pronounced anodic and cathodic peaks are representative of the PCs [49]. But, this is not enough for differentiating between ELDCs and PCs materials. The more quantitative and reliable analysis for understanding the data of CV characterization to infer the contribution from EDLCs and PCs mechanism separately is, to employ the facts that for EDLC $I(V) \propto v$ while for PCs $I(V) \propto \sqrt{v}$ [22], [36]. The problem is, that this approach also has limitation in ability to separate the contributions of reactions happening roughly at the same time scale [47] so more theoretical and experimental investigations are needed to solve this problem.

2.4.2 Constant current charge/discharge (CCCD)

CCCD characterization is most commonly used technique for SCs performance measurement under constant current [50]. It is measured by repetitive charging and discharging of SCs at constant current density in specific voltage window and graph of potential vs Time is achieved as an output as shown in Figure 2.9. Here selection of the constant current is very critical for consistent and reproducible results.

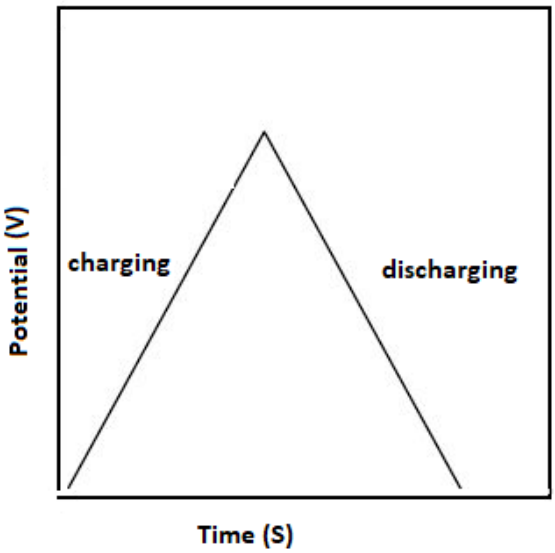

Figure 2.9 Charge and Discharge curve

CCCD is considered as the handiest and precise approach to characterize SCs devices, because all three core performance parameters C_T, R_{ES} and V_o are measured and later used to calculated other important parameter such as time constant, energy and power density. It is also used for testing cyclic stability of the device.

2.4.3 Specific capacitance

The specific capacitance of the cell can be calculated using the following equation [33],

$$C_{cell} = \frac{Q}{2V} = \frac{1}{2Vv}\int_{v-}^{v+} i(V)dV\,, \qquad 2.4$$

where C_{cell} is the cell capacitance, i is the current, v is the sweep rate, and V (V = V + - V -) represents the working potential window. The specific capacitance is computed by using the following equation [51],

$$C_{sp} = \frac{C_i}{B_i} = 2\,\frac{C_{cell}}{B_i} = 4\,\frac{C_{cell}}{B_i}\,, \qquad 2.5$$

where B_i is the mass of one electrodes. Capacitance was also calculated by using charge and discharge measurement using following equation [49],

$$C_{sp} = \frac{I}{dV/dt} \qquad 2.6$$

where I is the discharge current, V the voltage and t is the discharge time, dV/dt is obtained from the slope of the charge/discharge curve.

2.4.4 Energy density and power density

The two primary traits of the SCs are specific energy and specific power density. For either attributes, density can be calculated dividing each quantity by per unit mass or per unit volume (depending on the SC technology also per unit area of unit length). The energy E of the capacitor can be computed using the following relation, which is directly proportional to the capacitance [33],

$$\mathrm{E} = \frac{1}{2}\,\mathrm{C_{cell}}\,\mathrm{V}^2 \qquad 2.7$$

$$\mathrm{E_i} = \frac{1}{2}\,\frac{\mathrm{C_{cell}}}{\mathrm{B_i}}\,\mathrm{V}^2 \qquad 2.8$$

Where C_{cell} is the capacitance calculated by using equation (2.4), E and E_i are energy and energy density respectively, B_i is the mass of active materials (two electrodes). The power density P can be calculated by dividing energy density E per unit time T. But for power density computation, one aspect must be considered that capacitors are characterized as circuit connected in series with external load resistance, "R" as depicted in Figure 2.1.

The internal resistance, which is computed in aggregate by a number known as an equivalent series resistance (ESR), comprises of resistance of internal components of capacitor, such as current collector, electrode and dielectric material. The voltage during discharge is determined by these resistances when, measured at corresponding impedance (R = ESR), the maximum power density P for a SCs can be calculated as follows [24], [26], [33],

$$P = \frac{V^2}{4ESR} = \frac{\mathrm{E}}{\mathrm{t_{discharge}}} \qquad 2.9$$

$$P_i = \frac{V^2}{4ESR} \quad = \frac{P}{B_i} \qquad 2.10$$

$\mathrm{t_{discharge}}$ is the time of discharge of the device, B_i is the mass of the electrodes, P and P_i are the power and power density respectively. This relationship shows that power density is inversely proportional to the ESR and effect the maximum power density.

2.5 Material for supercapacitors

As discussed above, specific capacitance, energy and power density are strongly dependent on capacitance, so electrodes material have vital role in performance

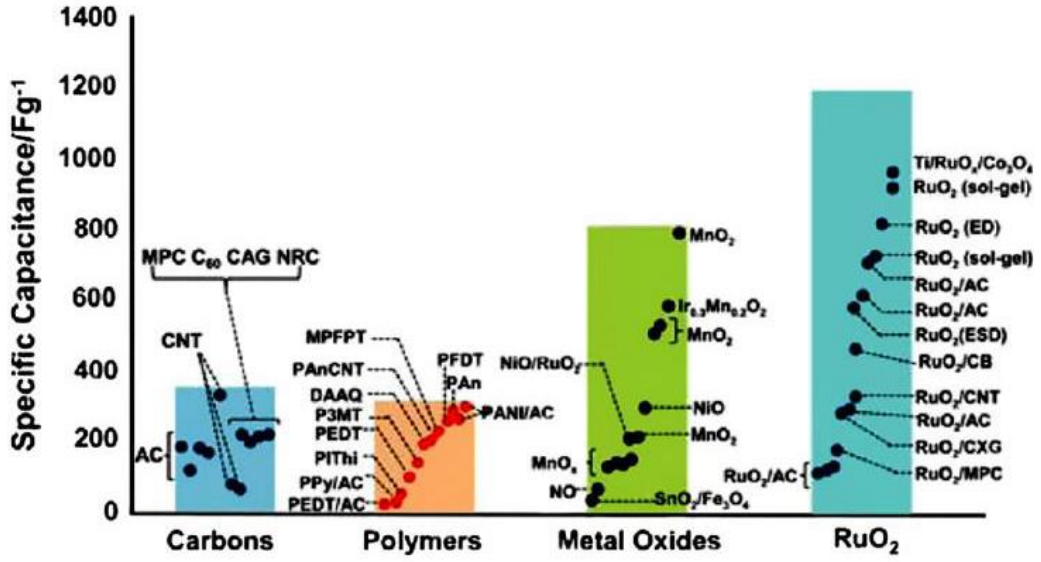

Figure 2.10 The specific capacitance values of various materials for both EDLCs electrode and PCs electrodes. (Reproduced copyright permission) [52].

of the SCs as shown in the Figure 2.10 below in which the specific capacitance of the electrode material compared with the type of the material used [52]. As it is clear from the Figure 2.10 Ruthenium dioxide and its composite electrodes shows the highest specific capacitance of almost 1000 F g^{-1}. The high specific capacitance of RuO_2 correspond to high conductivity and highly reversible charge and discharge [53]. But the problem with RuO_2 based electrodes (critical raw material for ECs) is, its high toxicity and cost which limit its application in SCs [54]. Recently, researchers are focusing their studies on inexpensive and non-toxic electrode materials to explore new cost-effective and environment friendly materials. In the coming section, I will discuss some of the most used materials and their behavior as SC's electrode.

2.5.1 Carbon based materials for EDLC's behaviors

Carbonaceous materials are characterized as most used class of material for SCs, since they offer a high specific surface area, high conductivity, high stability, non-toxicity and easy fabrication, which are vital parameters to enhance the EDLC. Because of these characteristics, carbon material has attracted immense attention of the researchers of its application in SCs as electrode material especially in EDLCs. Normally carbon-based SCs display a pure rectangular shape of CV and symmetrical triangular distribution in CCCD profile which is characteristic of EDLCs [55]. A material is considered to be a good material for EDLCs, if it exhibits excellent interparticle conductivity in porous matrices and easy approachability of the electrolyte ions to active sites of material [22]. High specific surface area of carbonaceous materials along with appropriate pores size distribution, pore volume, particle size, electrical conductivity, surface functional groups, allow to achieve high specific capacitance, high specific power and cyclic life [56]. Most commonly

used carbon materials as active material for SCs are, activated carbon, carbon aerogels, carbon nanotubes (CNTs), porous carbons and carbon nanofibers, all of them characterized by high specific surface areas [57]. As described in literature, both activated carbon and carbon aerogels exhibit a maximum specific capacitance in the range of 40-160 F g^{-1} [57] and carbon nanotubes (CNT) electrodes demonstrated a highest specific capacitance of 180 F g^{-1} in aqueous electrolyte potassium hydroxide (KOH) [32], [58].

According to the studies in literature, even if carbon materials with high specific surface area and excellent electrolyte accessibility to active sites is used, the cell can exhibit a relatively low specific capacitance. This is because, their high resistivity, owing to the contact resistance among carbon particles, activate a high intrinsic series resistance, and also some inaccessible active site of the carbon material which leads to a reduced SCs performance. It is supposed that future research on carbon materials will be on fabrication of carbon-based electrodes with high surface area, rationale pore distribution, and reasonable surface variation so as to improve overall specific capacitance and conductivity without damaging stability of the electrodes [59].

2.5.2 Faradic material

Carbon based materials used for EDLCs have problems of low specific capacitance and low energy density. There is another class of electrode materials called, Faradic materials, commonly employed as active electrode materials for PCs, for which the charge storage mechanisms are based on the fast and reversible surface redox reactions (Faradic reactions) and offer 10-100 times higher specific capacitance than EDLCs. Currently, lot of research groups are studying faradaic materials to change and synthesize the appropriate materials for PCs [59]. There are two types of faradic materials: i) Conducting polymers and ii) transition metal oxides.

2.5.2.1 Conducting polymers (CPs)

CPs are attracting great attention in recent years because, they offer high charge density, low-cost, substantial structural variety, environment friendliness, high electrical conductivity in a doped condition, high porosity/ excellent reversibility, and adaptable redox reactions through chemical alteration, which characterized them suitable as electrode materials for SCs [60], [61]. As compared to high specific surface-area carbon electrode based EDLCs, CPs based PCs accumulate higher amount of charges electrostatically (EDLCs) and via fast reversible faradaic processes, since CPs used both surface (as EDLC) as well as bulk of the material for pseudocapacitance [61]. First application of CPs was confirmed for SCs in the 1990s [62], when CPs display pseudocapacitance via doping/de-doping of the polymer, which results in electrolyte ions intercalation/de-intercalation inside the polymer electrodes to keep charge neutrality [63], [64]. The most common CPs

used, namely polyaniline (PANI), poly(3,4-ethylenedioxythiophene) (PEDOT), and polypyrrole (PPy), to exhibit specific capacitance equivalent to or higher than many transition metal oxides, the second main class of pseudocapacitive materials. Nonetheless, CPs employed as electrode materials often endure notable degradation, because of the mechanical instability instigated by oxidation and reduction during the charge/discharge procedures. This mechanical instability of CPs, during charging and discharging which, results in the poor cyclic life of the CPs based electrodes, has seriously limited their practical applications. This is because of CPs agglomerate during electrode fabrication and material tend to strip off from the substrate [61]. All those above-mentioned problems have restrained CPs to be exploited as active electrode material in SCs in pristine form. Hence, it is very important to combine CPs with other materials to fabricate a CPs composite, which is advantageous for the manufacturing of electrode materials with a high specific capacitance and excellent cycling stability.

2.5.2.2 Transition metal oxide (TMOs)

TMOs are characterized as the best potential electrodes material for electrochemical SCs because they offer very high specific capacitance coupled with a low resistance ensuing a high power density than a conventional carbon material, which attract great attention in commercial application [65]. Like CPs, they also not only accumulate charges electrostatically as in carbon-based electrode materials but also demonstrated electrochemical faradaic-reactions between TMOs electrode materials and electrolyte ions within suitable voltage windows [66]. The pre-requisites for TMOs to be potential candidate for SCs electrodes are [67]: i) metal oxides should have low electrical resistance, ii) the metal shall have two or more oxidation states that co-exist with stable phase including irreversible variations of a 3D crystal-structure, iii) ions can spontaneously intercalate into lattice crystal structures on reduction reaction (or deintercalated on oxidation) permitting facile transition of $O_2 \leftrightarrow OH^-$. To date, most studied TMO materials are, RuO_2, MnO_2, Fe_3O_4, Co_3O_4, NiO and V_3O_5 which are used for PCs. Among the above mentioned TMOs, RuO_2 is the best performant electrode material, owing to its high specific capacitance, long cyclic life, low resistance, excellent electrochemical reversibility and its high rate capability [59]. As mention above, the outstanding performance of RuO_2 in SCs (with theoretical capacitance of 1358 F g^{-1}) has captivated many scientists, but the dearth of abundance, toxic nature and high-cost of Ru are major shortcomings for commercialization of RuO_2 based electrodes for SCs and has limited its applications [66].

Owing to high-cost consideration, unfriendliness of RuO_2, researchers have put substantial efforts to explore cheaper and environment friendly alternative materials which exhibit same electrochemical behavior as of RuO_2. Some of those new alternative materials are: TiO_2, NiO, MnO_2, $MnFe_2O_4$, Fe_3O_4, WC, V_2O_5 and ZnO. But these alternatives have their own limitations such as, low specific capacitance,

poor cyclic stability, and low electrical conductivity. To elucidate these problems of low electrical conductivity and cycling stability of TMOs, it is advantageous to prepare composites with carbon-based materials in order to make use of synergistic effects.

2.5.3 Carbon material composite with transition metal oxide

Many investigations have been conducted by researchers to enhance the performance of inexpensive TMOs based electrodes including compositing the TMOs with carbonaceous materials and CPs which has helped them to overcome the problem of low conductivity of the TMOs [59]. Because it helps to shorten diffusion path length of metal oxides for electrons and cations of the electrolyte and allow more current to flow which results in higher specific capacitance.

Manganese oxides (MnO_x) presently considered to be relatively low-cost, no toxicity, and environment friendly inexpensive alternative TMOs with high theoretical capacitance value ranging from 1100 to 1300 F g^{-1} [68]. Nanostructured manganese dioxide electrode materials had shown exceptional electrochemical properties. However, their conductivity is generally low, which seriously affects their specific capacity, cyclic life, and scalability [69].

MnOx is available in different stable crystalline phases, such as MnO, Mn_2O_3, Mn_3O_4, and MnO_2. First application of the MnO_x as an electrode material in SCs was reported by lee et al. in 1999 [70] has captivated key consideration and is accepted a promising substitute class of pseudocapacitve materials for SCs at a starting point. The specific capacitance of the MnO_x mainly comes from the pseudocapacitive charge storage mechanism which is escribed to be reversible oxidation/reduction transitions including mutual exchange of proton and/or cations with electrolyte solution and usually underwent transitional changes from M(III)/Mn(II), Mn(IV)/Mn(III), and Mn(VI)/Mn(IV) within the electrode potential window of the electrolyte [59], [71], [72]. The potential charging and discharging reaction occur for Mn are as follows,

$$MnO_{x\ surface/\ bulk} + C^{+} + e^{-} \leftrightarrow Mn\ (OOC)_{surface/\ Bulk} \qquad 2.10$$

where C^+ shows the protons and alkali-metal cations (Li^+, Na^+, K^+) in the electrolyte solution and MnO_x & Mn (OOC^+) show $MnO_2.nH_2O$ in oxidation and reduction states, respectively. It is clear from the literature, that electrochemical performances of MnO_x electrodes are highly contingent on the morphology, crystal structure, defect interaction, porosity and surface which have very prominent role defining the electrochemical properties [73]. Highly dedicated and focus investigation have been conducted for regulating the synthesis conditions to optimize capacitance and power density performance of MnO_2 with appropriate morphology and crystal structure [59].

Many techniques have been used to synthesize MnO_2, such as, sol gel technique [74], [75] solution-based chemical routes [76], thermal decomposition [77], co-precipitation [78]. Unfortunately, most of these synthesis method have some problems: firstly they employ dangerous, lethal solvent and reducing mediators [79]. Secondly, the thickness of active materials loaded using hydrothermal or sol-gel method is hard to control [59].

Electrodeposition (ED) method is considered to be the best method for the synthesis of the MnO_2 as active material for SCs which offer many advantages over the above-mentioned techniques. Owing to robust environmental directive, current emphases are on classifying alternate methods through environmental benign green chemistry methods. Electrochemical deposition has several distinct advantages for the preparation of the thin film material [79]: *i)* technique setup is not capital intensive, ii) low temperature deposition (room temperature) minimize interdiffusion, *iii)* uniform film deposition on substrate of complex shape with high degree of reproducibility, *iv)* film thickness can be controlled by changing the current density and time of deposition *v)* ED certifies a high density of loading of deposited material within the voids of the substrate, *vi)* the composition and defect chemistry can be controlled by changing applied potential. ED is very flexible in the diversity of choice of reagents that can be employed because abundant metals, alloys, oxides, semiconductors, and CPs can be deposited from solution under conditions that are well-matched with the substrate. To get excellent electrochemical properties, continuous and interconnected particles film of manganese oxides must be deposited on substrate. Babakhani & Ivey (2010) [79] have investigated different parameters of deposited MnO_2 employing galvanostatic ED techniques. By altering the deposition parameters such as current density, deposition time, electrolyte concentration, deposition temperature and solution pH, a series of nanocrystalline MnO_2 electrodes with different morphologies can be synthesized. The best performance in terms of capacitance was achieved to be ~230 F g^{-1} with capacitance retention of ~88 % after 250 cycles in 0.5M sodium sulfate electrolyte at sweep rate of 20 mV s^{-1} [80]. From the literatures, it is clear that, ED method always exhibits higher specific capacitance but it is still much lower than its theoretical capacitance [81]. This lower specific capacitance is owed to its poor electrical conductivity (~10^{-7} to 10^{-3} S cm^{-1}) [36].

In addition to MnO_x, ZnO is also consider as an alternative substitute material for SCs. Zinc oxide (ZnO) has wide band-gap and behave as a n-type semiconductor, thanks to the intrinsic doping induced by oxygen positions or zinc interstitials. It is categorized by excellent electron transport properties and, together with the other metal oxide e.g. TiO_2, it can be considered the most diverse TMO in energy and sensor applications. Owing to its unusual properties, ZnO has been successfully employed as electrode for dye-sensitized solar cells [82], piezoelectric nanogenerators [83], Li-Ions batteries [84] , memristors[85] and various types of sensors [86], [87]. Furthermore, it can be easily synthesized into diverse

nanostructures such as nanotetrapods, nanotubes, nanoparticles, nanowires, nano rods, nanoflakes and nanosheets. Lu et al. [88] reported a specific capacitance of 61.7 F g^{-1} for graphene-ZnO composite synthesized by ultrasonic spray pyrolysis and Jayalakshmi et al. in another report [89] showed a maximum specific capacitance of 21.4 F g^{-1} for ZnO/Carbon composite in aqueous electrolytes.

In summary SCs are supposed to circumvent the problem of ever increasing energy needs owing to their higher specific power density and longer cyclic life than batteries. The electrode materials of SCs are one of the vital aspects to realize high energy and power density devices. Several electrode materials have been exploited for SCs including carbon-based materials, TMOs and CPs. However, the pristine active materials showed poor electrochemical performance. Therefore, compositing electrode materials is an effective alternative to enhance the electrochemical performance of the electrodes. Various composite materials and synthesis procedures will result in different film morphologies which will affect the electrochemical performance. The drawbacks pristine electrode material (MnO2, ZnO, etc.) is effectively overcome by composite it with several other TMOs or carbonaceous materials.

2.6. State of the art fiber-like flexible supercapacitors

The quest of reduced, slimmer, significantly lightweight, and flexible portable electronics has just appeared as hot topic of research and application tendency. Eccentric device configurations have unlocked a new vision of future flexible wearable electronics such as body-compatible implantable sensors, intelligent skins, and

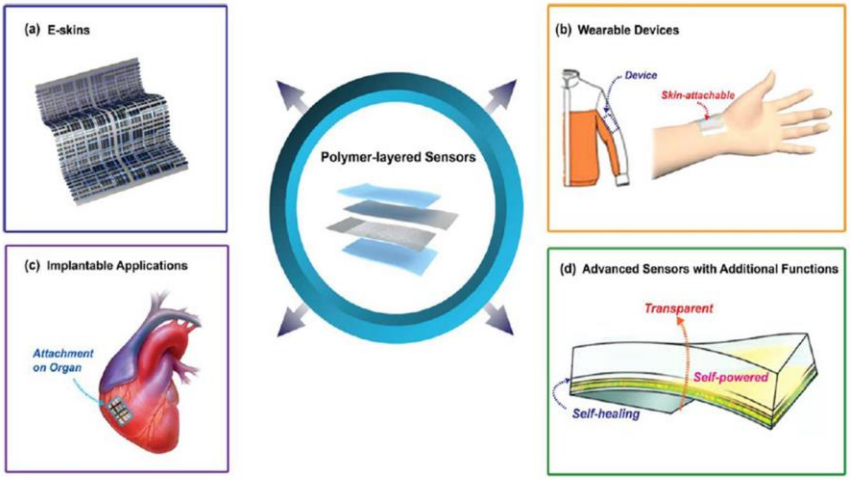

Figure 2.11 Different applications of the supercapacitors. (Reproduced copyright permission) [90]

elastic electronics (Figure 2.11) [91]. For example, an intelligent skin may possibly offer a solution for real time body sensing that can help in controlling biological signals and healthcare information of human body while supporting human beings

in diverse conditions and happenings [81]. Wearable electronics entail evolution and fabricating an efficient electronic component such as flexible displays, transistors, energy harvesting and storage devices on a single electrode substrate to realize an entirely self-powered and cost-effective integrated devices [92]. The conventional SCs based on liquid electrolyte are large in size (due to encapsulation package for safety from dangerous electrolytes), heavy weight and rigid which make it difficult for conventional SC to meet the requirements of flexible electronics. Although, in the recent past,researchers have been succeeded in developing all-solid-state planar-shape SCs [93] but these devices do not allow the sweat and air to pass from the human body freely and limited the wearability for different applications [25]. In this situation, new class of flexible fiber shaped SCs (FFSS) has emerged, which has diameter ranging from micrometer to millimeter, are light

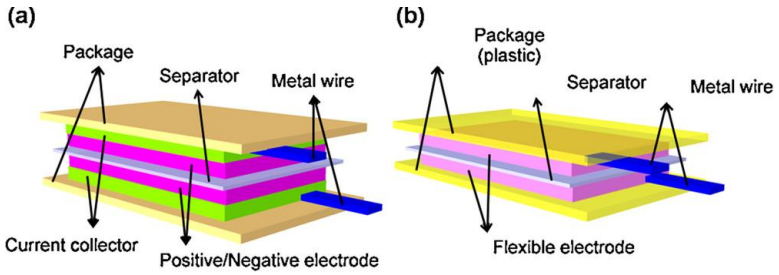

Figure 2.12 (a) 3D schematic illustration of conventional SCs and (b) Flexible SCs. (Reproduced copyright permission) [83].

weight and smaller in size. Fiber shaped SCs due to their unique structure are highly flexible and can be integrated into textile through knitting or weaving easily. A FFSS like typical conventional SCs comprises: wrapping package, flexible current collector (wire, carbon fibers), electrolyte (solid state polymer), negative and positive electrodes, separator as shown 2.12a. The assembly of flexible SCs is shortened with integrated electrode (no need of separate current collectors and binders) as shown in Figure 2.12b, because the carbon-based current collector, with higher electrical conductivity and flexibility, function as both the flexible current collector and active electrode [94].

2.6.1. Flexible substrates for flexible supercapacitors

A crucial approach to enhance the specific energy density of the fiber SCs is to develop fiber electrodes with high specific capacitance. Additionally, flexible fiber-based electrodes with robust mechanical properties are required for flexible and wearable applications. Substantial investigation efforts have been devoted for the fabrication of these electrode. Based on recent advances, fabrication of the flexible electrode can be classified into two main groups: (i) flexible freestanding films of active materials and (ii) substrate-supported active materials on flexible current collector [95].

2.6.1.1. Freestanding films of active materials

Recently, a new technique was reported to fabricate self-supporting and self-standing films of active materials. This technique helps evading usage of current collector, additive and binder free active materials which results in reducing the mass of the loaded active material leads to enhanced specific capacitance and energy density respectively [96]. One of the greatest advantages of the self-supporting film is that, it helps in fabricating solid state SCs devices demonstrating excellent strategy for best material exploitation for SCs applications[97]. Countless solution and processing techniques have been demonstrated to manufacture self-supported carbon-based electrode materials for SCs [96], specially carbon nanotubes nanoparticles [98], and graphene [99] and compared to all these carbon materials, carbon nanotube is the best performing electrode material owing to its large specific surface area (1200-2200 $m^2 g^{-1}$), high conductivity (10^4-10^5 S cm^{-1}), well controlled regulated pore structure [100]. The thickness of the film deposited on flexible substrate in freestanding electrodes is very crucial and it is normally in the range (< 50 µm). One of the problems with the freestanding electrodes is that film is very delicate and can strip off from the surface of the substrate during extended bending stress.

2.6.1.2. Substrate-supported flexible electrodes

To counter the problems arose in freestanding electrodes, many experiments have been performed to support the active electrode material loaded on the flexible substrate. This method comprises growth and coating of active electrode materials on porous, lightweight and flexible current collectors such as: i) flexible metal wires, Copper (Cu), Nickel (Ni), Stainless steel (SS), Titanium (Ti) etc. ii) carbon-based electrodes and porous material (conventional paper, textiles, cable-type electrodes and bendable plastics) [95].

i) Wire shape flexible electrodes

Flexible metal wire-base current collectors (Figure 2.13) have been widely employed as conductive substrate for SCs because they exhibited very low resistance, higher electrical conductivity and good mechanical stability. Various flexible metal wire-based current collectors have been reported in literature such as: SS [101], Cu[102], (Ni) [103] and Ti [104] wires, which offer not only good mechanical strength but also easy production process. In addition to ease of manufacturing process, the direct synthesis of the electrode material on the surface of the substrate results in flexibility, higher specific capacitance and specific energy density. On contrary the synthesis of electrodes material in powder form need additional binders for electrode material to adhere with substrate which results in low

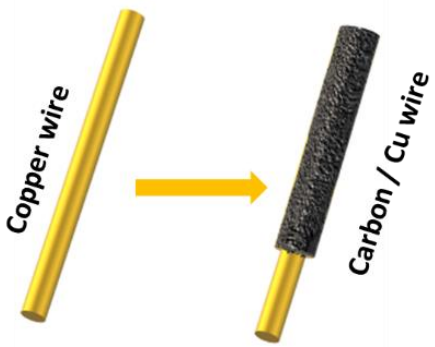

Figure 2.13 Wire-based electrodes

specific capacitance, low energy density and mechanical robustness [105]. Despite these improvements, the metal wire-based substrates used in flexible wires shape SCs electrodes are generally quite thick and bulkier than the loaded active material. Therefore, as gravimetric specific capacitance depends only on mass of the loaded active material, so optimized mass loading is required in order to get higher value of specific capacitance. Moreover, the charge transportation in the thick electrode materials is not convenient to the surface of the current collector because of large diffusion path length, thereby greatly reducing the rate capability and specific capacitance of SCs [105]. This problem was elucidated by manufacturing 3D foam and mesh like structures who help in loading optimum mass of the active material and results in improved electrochemical performance.

ii Carbon flexible electrodes (carbon fibers, fabric, carbon paper)

Metallic porous substrate, owing to their conductivity and porosity, are considered excellent candidates for flexible SCs application but their low corrosive

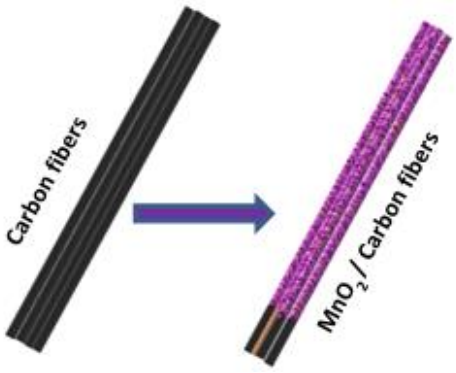

Figure 2.14 Carbon fiber substrate

resistance confines their applicability as substrate [94] and make the device bulkier because of their high density. On contrary, carbon-based flexible substrates (Figure 2.14) , such as carbon fiber, fabric, paper and foam demonstrate higher

electrical conductivity and most prominently, high flexibility and lower weight to make them better contender for flexible fiber-shaped SCs application [106]. Here, I present the current developments in the carbon-based flexible substrates for FSSCs. Carbon materials with outstanding chemical properties and exciting chemical constituents offers large surface areas, excellent conductivity, and discrete carbon atoms, which can be coupled to formulate pore channels to transport electron and ions of electrolyte effectively [35]. Owing to high porosity, mechanical veracity and good electrical conductivity, they have been extensively used as substrates in energy applications such as fuel cells and SCs [107]. For instance, Kang et al. described the synthesis of MnO_2/carbon nanofibers nanocomposites as freestanding electrodes and achieved the maximum capacitance of 365 F g^{-1} at a current density of 1 A g^{-1}. This freestanding electrode also exhibited good rate capability in terms of power density of 13.5 kW kg^{-1} and energy density of 20.9 W h kg^{-1} at 30 A g^{-1} along with excellent cycling stability, capacity-retention 94% of its original capacitance after 1500 cycles [101-102]. Similarly, Zhi et al. [103] reported very conductive carbon MnO_2/nanofiber coaxial cables in which single electrospun carbon-nanofibers were deposited with an ultrathin hierarchical MnO_2 layer which exhibits a capacitance of 311 F g^{-1} at the scan rate of 2 mV s^{-1}.

2.6.2 Architecture of flexible supercapacitors

One of the key factors affecting SC's performance is the architecture of the device. With regard to the device architecture, flexible SCs are mainly classified into three groups. I) fiber or wires shaped supercapacitors, ii) parallel plates flexible SCs and iii) interdigitated SCs

2.6.2.1 Parallel plates flexible supercapacitors

The very concept of the parallel plate capacitor was first introduced in 18th century [13] for conventional capacitors in which two plates are placed parallel to each other as decribed in detail in section 2.2. In this configuration, when the potential is applied across two plates like electrodes, an intrinsic electrostatic field will be generated across the dielectric with differing polarity to that of the applied electrical field. But parallel plate flexible SCs are fabricated by placing two flexible electrodes parallel to each other on a planar substrate and separator or gel-polymer electrolyte between these two electrodes to avoid the short circuit as shown in figure 2.15a [108]. Here, the charges are stored using (EDL or faradaic reactions depending on the active material used as the electrode) at the interface between electrode and electrolyte which are separated by a distance of < 1 nm. In order to enhance specific capacitance beyond the level of the traditional parallel plate

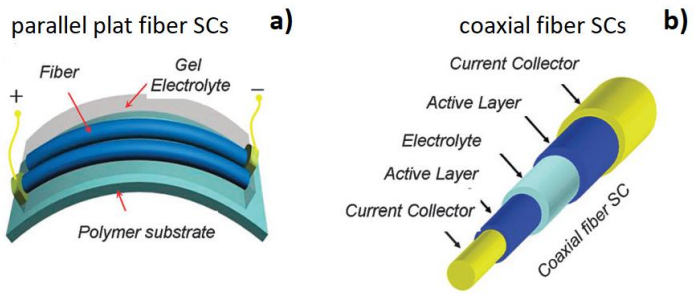

Figure 2.15 Architecture of parallel plate flexible SCs a), coaxial fiber SCs b). (Reproduced copy-right permission) [108]

capacitor, we have to increase the surface area of the electrodes to store more charge particles.

2.6.2.2 Wires or fiber-shaped supercapacitors (co-axial)

Apart from parallel plate SCs comprise of two fibers electrodes twisted together, there have been a few efforts of evolving coaxial fiber-like SCs fabrication as shown in figure 2.15b [108]. Compared with two-parallel plate flexible SCs, the production procedure of coaxial fiber-like SCs is more complex and special actions must be taken to confirm the micrometric thickness of the gel-polymer electrolyte layer, certainly averts the chance of short-circuit among the core electrode and the exterior electrode during the whole device length [91]. Nevertheless, a coaxial fiber-like SC is an innovative energy storage device assembled on a single fiber structure, and there will be no potential problem of delamination of two fiber electrodes in commercial application as is in case of two parallel plate flexible SCs. Investigation towards this direction is just on an early stage.

2.6.2.3 Interdigitated supercapacitors

Interdigitated electrode fabrication method is a normally used for micro SCs, where the electrodes stick side-by-side and infuse together on a current collector or substrate as shown in the Figure 2.16. In comparison to traditional sandwich-like SCs and fiber-shaped architectures, micro-SCs generally selected a planar configuration with in-plane interdigital electrode interstices, which offers several advantages [14]. Firstly, the in-plane architecture configuration can increase the approachability of the active materials, as the protruding edges of the active elec trodes are directly exposed to electrolyte.

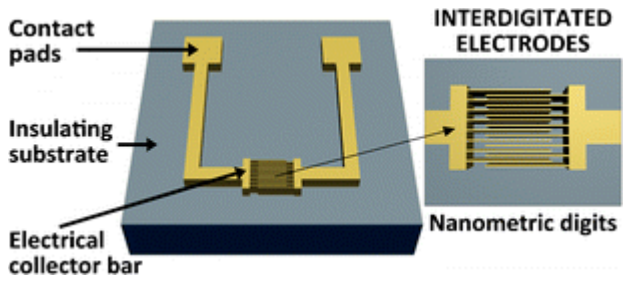

Figure 2.16 Interdigitated electrode. (Reproduced copyright permission) [109]

Consequently, an ultrahigh specific power density is achieved which is many orders of magnitude larger than that of conventional SCs and batteries. This is mainly significant for the cases where the electrodes are fabricated from 2D layered materials [110]. Secondly, owing to the trivial interspace amid electrode finger arrays, and elimination of the separators (necessary in SCs with conventional sandwich architectures), cell electrolyte ion-transport resistance can be reduced, and a high-frequency response can be obtained. This is critical factor for future miniaturized portable electronics [111]. Thirdly, interdigitated electrodes architectures help to integrate micro-SCs into on-chip integrated circuits [14]. All of these advantages render micro-SCs with in-plane interdigitated electrodes architectures as influential candidates in miniaturized portable electronic devices application, especially on-chip electronic device.

2.7 Applications of supercapacitors

SCs can offer higher power densities than batteries and accumulate great amount

Figure 2.17 Application of supercapacitors in different fields. (Reproduced copyright permission) [112]

of energy than conventional capacitors. Meanwhile, other advantages such as a high charge/discharge rate and a long cyclic life, SCs can be used for the following applications. Figure 2.17 shows some of the potential application of the supercapacitors in different fields, such as biomedical, smart grids, hybrid electrical vehicles, E-textile, wearable fitness tools, and Airplane industry etc.

2.8 Summary

Earlier research present in literature on operating principle, electrode material composition, different categories and potential applications of SCs were summarized in this section. The imminent technological growths of SCs are advancing towards flexible SCs. The flexible SCs exploration has become a comparatively new area of scientific interest. Recent studies in this arena were also reviewed. Maximum studies were focus on, how to enhance the electrochemical performance of the SCs either synthesizing and developing new electrode material or how to design the novel configurations of the flexible SCs. It is believed that the advancements in the investigations of flexible SCs will enrich knowledge of this novel and emerging field. This will also empower for further progress of highly flexible energy storage device and put development of smart energy source technology on fast-track.

Chapter 3 Wire shaped electrode exploiting graphite/ZnO composite electrode

"I could trust a fact and always cross-question an assertion"
— Michael Faraday.

3.1 Introduction

Wearable SCs play a crucial role as reliable flexible power supplier for replacing batteries which has safety and compatibility issue (e.g. bulkiness, rigidity) with flexible and portable electronic systems[113],[114]. In this chapter, parallel wire-shaped SCs were fabricated using low cost, environment friendly material exploiting simple facile dip-coating technique on copper wires. Metal-wires (MWs) are characteristically introduced as the flexible current collector and framework for fabricating electrode materials for flexible fiber shaped supercapacitors, due to their high conductivity [115]. Here, ZnO nanoparticles are added in different concentrations (1 %, 5 %, 10 % and 20 % respectively) to fine graphite powder to enhance the specific capacitance of the active electrode material. The SCs devices are assembled in a two-parallel wire configuration engaging a gel-polymer electrolyte which acts both as separator and ionic mediator. The electrochemical performance is evaluated by using cyclic voltammetry, exhibiting the excellent energy storage properties of the device under bending stress conditions and textile-integrated conditions. Part of this study has been published [116].

3.2. Experimental section

This section contains the detail about the fabrication of the electrodes and device.

3.2.1. Graphite-based Electrode (EDLC)

Electrode fabrication

Graphite pellet (Supreme Mineral) are ball-milled (Pulverisch 7, Fritsch, Germany) to obtain ultrafine graphite powder at speed of 850 rpm for 15 minutes, both clockwise and anticlockwise. The carbon-based slurry was prepared using 1 g of ultrafine graphite powder mixed with 3 ml Polyvinylidene fluoride (PVDF) solution

(2 wt.% PVDF in N-Methyl-2-pyrrolidone (NMP)) and ultra-sonicated for 10 min (Lab Sonic LBS-2 22.5 FALC) at 59 Hz frequency and 100 W power. Copper wires, selected as flexible substrate, are cut into 2.5 cm length pieces and prudently cleaned with acetone and ethanol for 5 minutes respectively. Electrodes are manually fabricated by simple dip-coating technique into container comprising active material slurry. The mass of the loaded active material on substrate is controlled by keeping a fix ratio (i.e. 1:3) between active material and solvent to get an optimized viscosity of the slurry, hence reproducible film of active material on substrate (Cu wire). As coated samples are dried on heat plate at 100 ^{o}C for 15 min to evaporate excess of solvent. Mass of the loaded active material is evaluated by weighing before and after coating flexible substrates for specific capacitance calculation.

Synthesis of gel-polymer electrolyte

Gel-polymer used is comprise of PVP in 1 M NaCl solution. Gel-polymer electrolyte is prepared by dissolving (Polyvinyl pyrrolidone (PVP-10, Sigma Aldrich) in 1 M of NaCl in water while continuous stirring. Solution is heated for 4 hours until a clear solution is obtained.

Assembly of device

Graphite coated copper wire electrodes are soaked into gel-polymer electrolyte for 15 minutes and after this they are put on hot plat for 5 min to semi-solidify the polymer electrolyte. After cooling these electrodes are assembled into device in two electrodes parallel configurations.

3.2.2. Graphite / ZnO based nanocomposite electrodes (PCs)

Electrode fabrication

In order to fabricate a nanocomposite slurry of ultrafine graphite and ZnO same procedure is repeated as mentioned above. 1 g of ball-milled ultrafine graphite powder is mixed with commercial ZnO nanoparticles (Zinc Oxide, APS powder - Nanotek, Alfa Aesar) in solvent (2 wt. % PVDF in NMP). Varied amount of ZnO nanoparticles are mixed into the as prepared paste: 1 %, 5 %, 10 % and 20 % of ZnO nanoparticles upon weight of graphite respectively. After mixing all these ingredient, it is ultra-sonicated for 15 min to get a uniform slurry. Same copper wires, chosen as flexible substrate, are cut into 2.5 cm length pieces and prudently cleaned with acetone and ethanol for 5 minutes respectively. Electrodes are manually fabricated by simple dip-coating technique into container comprising

composite slurry of graphite/ZnO. The further process is repeated as mentioned above.

Device assembly

Same procedure was used to assemble a device as employed in case of simple graphite/Cu wires device. Here graphite/ZnO nanocomposite was used as active material. After dipping these electrodes into gel-polymer electrolyte (mention above), they were placed on hot plate for 5 min for electrolyte to semi-solidify. After cooling these electrodes were placed on a planer substrate and sealed properly to avoid the drying of electrolyte and device.

3.3 Characterization of the materials

The crystallographic characterizations of the as-synthesized samples were performed with a Panalytical X'Pert MRD Pro X-ray duffractometer in Bragg/Brentano configuration with a Cu Kα X-ray source.
Raman spectrum was achieved using Renishaw InVia Reflex micro-Raman spectrometer (Renishaw plc, Wottonunder-Edge, UK), equipped with a cooled CCD camera, with a laser excitation wavelength of 514.5 nm and a laser spot size of 10 μm.
The characterization of morphology was carried out by means of a Field-Emission Scanning Electron Microscope (FESEM Supra 40, manufactured by Zeiss), equipped with an Oxford instruments EDX Si(Li) detector (10 mm^2 detection area). The images which contain elemental information were acquired by adjusting the collector bias voltage of the Everhart-Thornley detector in order to produce pseudo-backscattered electron images.
Electrochemical performance of the supercapacitors was evaluated by cyclic voltammetry performed with a Metrohm Autolab PGSTAT128 potentiostat / Galvanostat. Galvanostatic charge/discharge measurements are obtained with an Arbin Instrument Testing System model BT-2000. Both above-mentioned measurements are performed in device configuration (e.g. two symmetric electrodes).

3.4 Results and discussions

In this section, I discuss the details about the morphology, physical characterization (XRD, Raman) and electrochemical characterization.

3.4.1 Surface morphologies

Figure 3.1a shows the schematic representation of the preparation of the ultrafine graphite powder from granular graphite, employing ball milling machine following

coating of ultrafine graphite slurry on current collector (copper wire substrate). After the coating process, the morphology of the obtained wire-shaped electrode is examined by FESEM measurement as shown in Figure 3.1b, low-magnification top-view images exhibit the uniform deposition of composite active material on

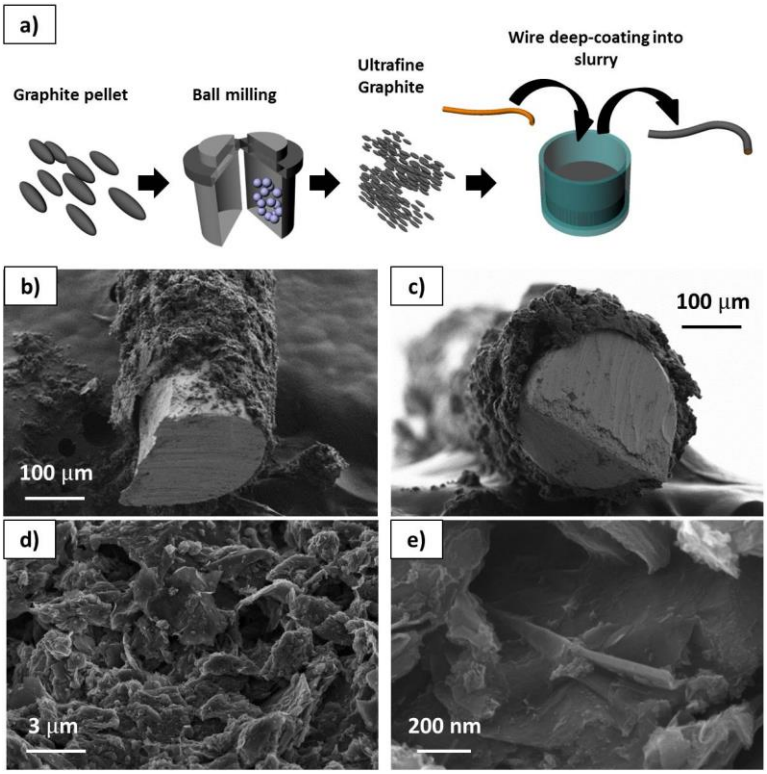

Figure 3.1 a) Shows Scheme of the coating of slurry on copper wire, b-c) shows the FESEM images of the coated wire-electrodes in top and cross section view respectively, d-e) higher magnification images of the graphite slurry. (Reproduced copyright permission) [116]**.**

the wire-based electrodes. In Figure 3.1c, from the cross-sectional view, it is possible to evaluate the thickness of the active material covering, which is in the order of tens of µm. The variation of active material layer thickness could be the consequence of deposition method or due to the manual cutting for cross-section exposure prior to FESEM measurements. Regarding the deposition technique, it is a very simple and scalable method to coat the flexible current collector with the active material with almost insignificant variation in the material loading. Certainly, more than 50 electrodes samples were fabricated using this method with an average active mass deposition of 2.0 ± 0.2 mg cm^{-1} and the variation in the deposition of active mass is not more than 10 %. Figure 3.1d-e show higher magnification images of morphology of the ball-milled fine graphite nanoparticles, which constitute the layer of active material. It is clear from Figure 3.1d that, shape of the fine graphite nanoparticle obtained is not exactly flat but rather consists of round shape particles. The edges of the nanoparticles got damaged owing to abrasion during the ball milling procedure [85]. The nanoparticle has varied size distribution, with lateral size varying from the scale of nanometer (nm) to the

micrometer(μ) and variable in thickness. It is worth noting, the porous nature of the deposited active material, which is vital to allow the diffusion of the electrolyte ions through the whole 3D carbonaceous network letting charge buildup for energy storage purpose. The aforesaid graphite-based electrode fabricated by decorating with ZnO nanoparticles, to enhance its electrochemical performance as SCs electrode via pseudocapacitive behavior. Four different types of composite slurries were prepared and investigated (see Figure 3.2a FESEM image) by adding different amount, (e.g. 1%, 5%, 10% and 20 % respectively), of commercial ZnO upon weight of graphite. ZnO nanoparticles of different aspect ratio and variable morphology (see Figure 3.2a) are employed for the decoration of the graphite nanoparticles at four different amounts: 1%, 5%, 10% and 20% ZnO upon weight of graphite are investigated.

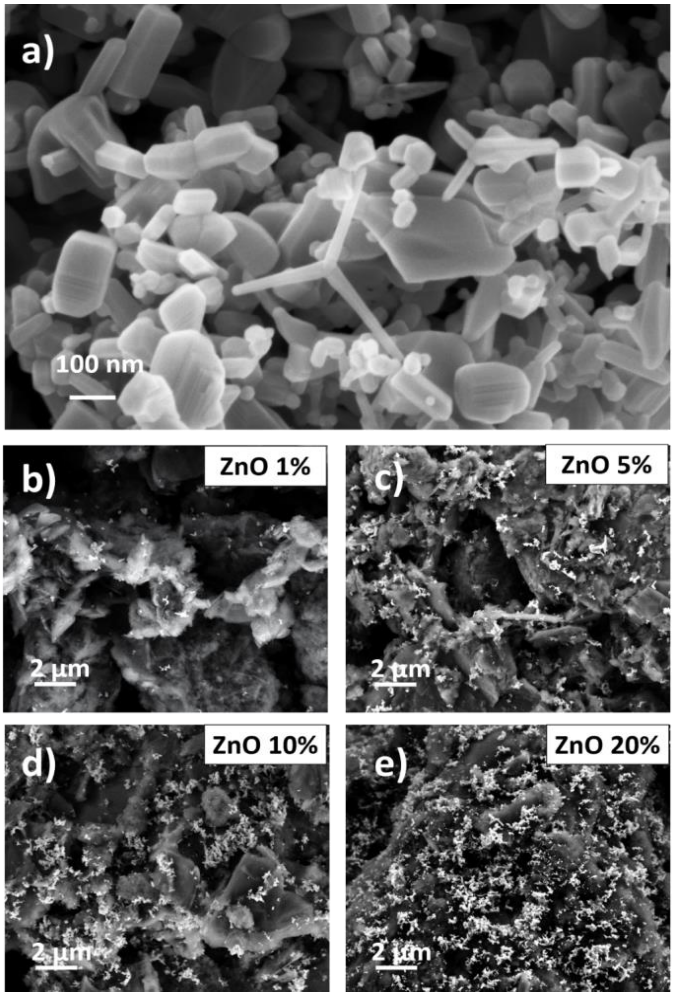

Figure 3.2 a) Shows the FESEM images of the morphology of commercial ZnO nanoparticles, b-e) Panels are low-magnification FESEM images of composite slurry prepared by mixing 1 %, 5 %, 10 % and 20 % of ZnO nanoparticles with graphite respectively. (Reproduced copyright permission) [116]**.**

Low magnification FESEM images (Figures 3.2b-e) present ZnO nanoparticlesat different amount can be depicted at high-intensity (almost white) structures. These

sights of the amalgam pastes slurries permit to appreciate the uniform and homogeneous scattering of ZnO nanoparticles over sections several hundred μm^2 wide, where the ZnO nanoparticles are arranged in small sub-micrometric agglomerates in all four slurries as shown in Figure 3.3a-d.

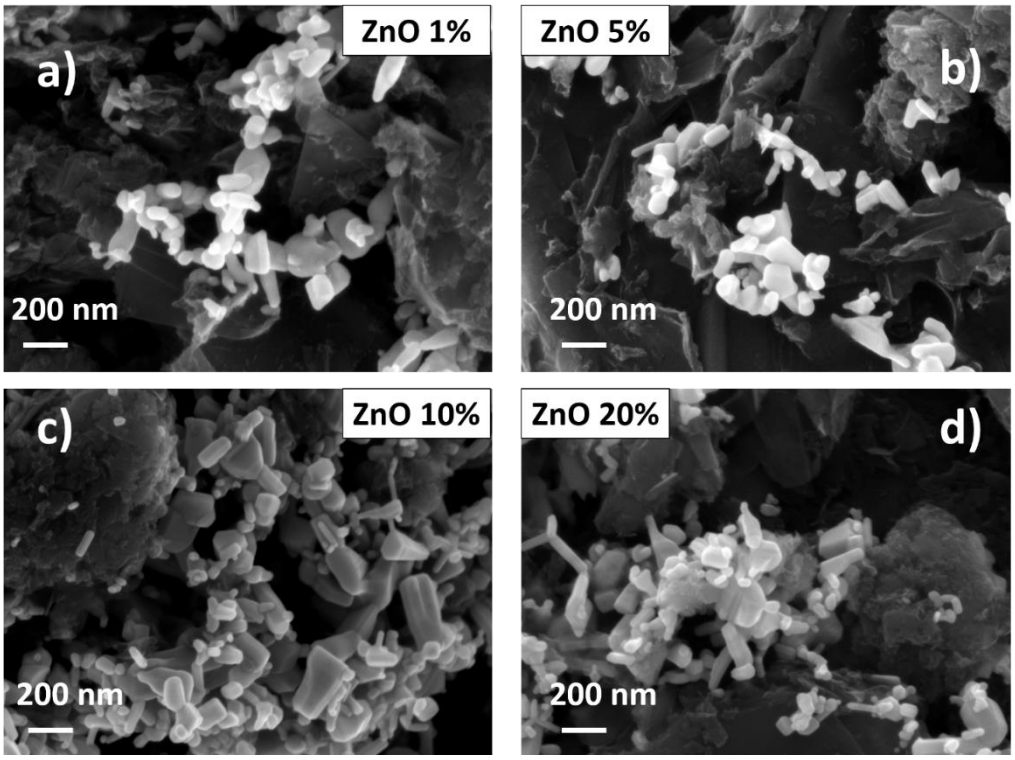

Figure 3.3 a-d) Higher magnification images of the all four slurries. (Reproduced copyright permission) [116]

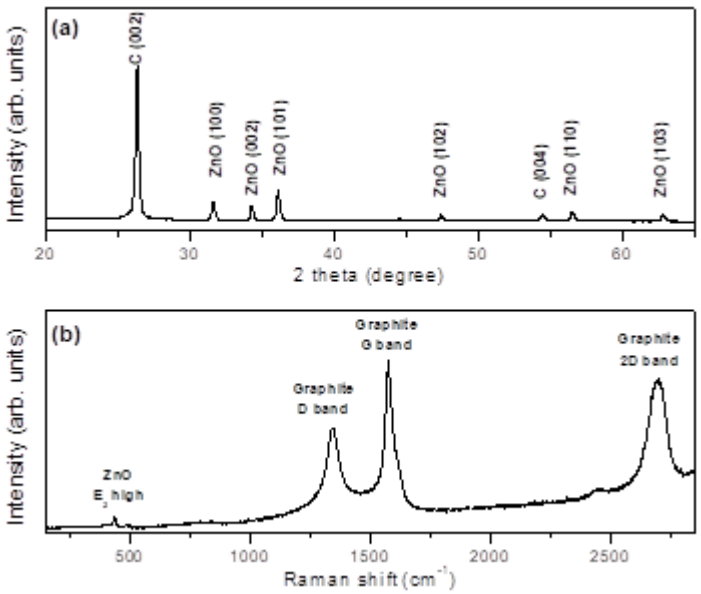

Figure3.4 X-ray diffraction (a) and Raman (b) spectra of graphite/ZnO composite. (Reproduced copyright permission) [116]**.**

The crystallographic structural properties of the active electrode materials are assessed through X-ray diffraction and Raman spectroscopy. Figure 3.4a shows the diffraction spectra of the composite material in which the graphite shows a very strong (002) peak at ~26.3 ° (2 theta), agreeing to an interlayer spacing of d_{002}=0.338 nm, characteristic of bulk graphite [117]. The ZnO shows a pure hexagonal wurtzitic crystal structure in a randomly oriented polycrystalline network (a=0.3253 nm, c=0.5215 nm, space group P63mc, JCPDS card: 89-0511). The mean crystallite dimension, as determined by Scherrer formula, is almost equal to 30 nm, in line with the FESEM measurements previously reported in Figure 3.2a. Figure 3.4b shows Raman spectra, which is dominated by the structures coming for the graphitic features, with D peak at 1340 cm^{-1}, G peak at 1580 cm^{-1} and 2D peak at 2695 cm^{-1} respectively. The D peak depicts the presence of defects on in-plane sp^2 domains, while the G peak instigated from a first order inelastic scattering procedure including the degenerate iTO and iLO phonons at the G point (E_{2g} mode) and the 2D peak is associated with the 2nd-order zone- boundary phonons [118]. The weak signal at ~438 cm^{-1} initiated from the oxide decoration of the carbon structure, being related with the active branch of the non-polar optical phonon E_2 high mode, related with zinc and oxygen of wurtzitic ZnO [119].

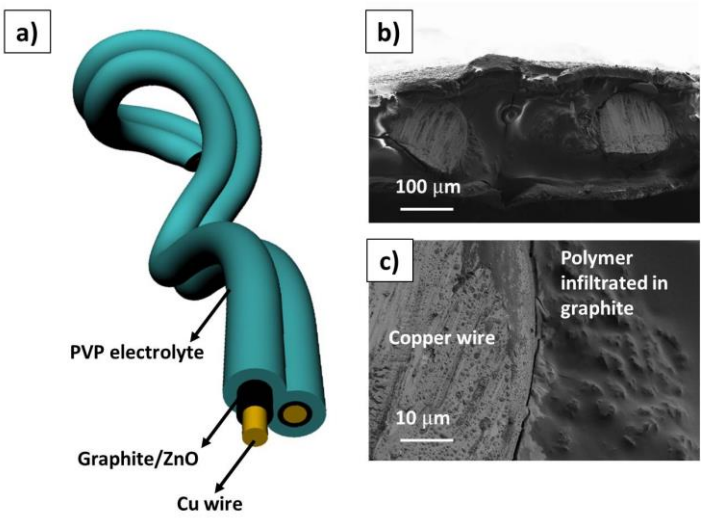

Figure 3.5 a) Show 3D representation of two parallel electrode arrangement, b) cross-sectional FESEM images at lower (b) and higher (c) magnification of the PVP gel-polymer electrolyte-coated electrodes. (Reproduced copyright permission) [116]**.**

3.4.2. Electrochemical characterization

Figure 3.5a shows the 3D schematic representation of the two parallel-electrodes configurations of assembled supercapacitor device. The copper wires-based electrodes covered with active material were dipped in polymer electrolyte to wrap the electrodes with solid polymer electrolyte, has dual functionality, polymer electrolyte as well as separator between two electrodes to evade short circuit. Figure

3.5 b-c, shows the FESEM images of the assembled devices, demonstrating the formation of a compact structure, with securely sandwiched between two parallel electrodes. Higher magnification images were also obtained to shows the cross-sectional view (Figure 3.5c) of the electrodes, permitting to appreciate the good interface between the copper wire and the electrode active material as well as the perfect diffusion of the gel-polymer electrolyte into the porous carbonaceous network. These two interfaces are the most significant in the SCs devices since the latter permits ions storage into the pores of the conductive materials while the former allows charge transfer to the substrate. Cyclic voltammetry is performed to evaluate the specific capacitance both in plane condition and under bending conditions.

3.4.2.1 Graphite-based electrodes

Carbonaceous materials characterize the most used class of electrode materials

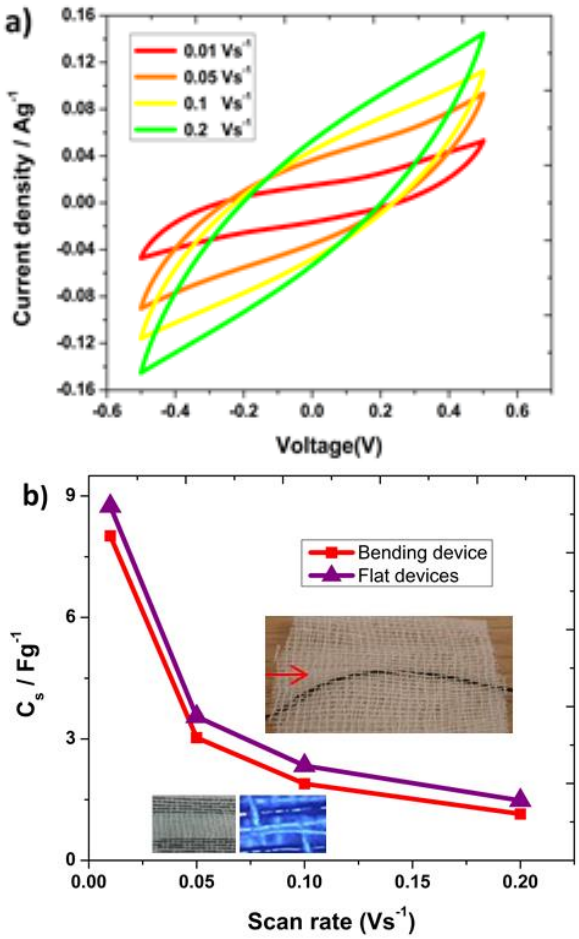

Figure 3.6 a) Shows the CVs recorded at different scan rates, b) comparison of specific capacitance as function of scan rate of plane and bended wire-based SCs. (Reproduced with copyright permission) [116]

exploited for SCs fabrication, since they can deliver a high electrical conductivity and high specific surface area, fundamental to enhance the EDLC. Electrochemical double layer SCs are based on the EDL principle as described in detail in chapter 2 Figure 2.1. In ELDC's energy storage is obtained by electrostatic process by separating charges at the interface between the surface of a conductive electrode and an electrolyte without faradaic reactions. This stored energy in EDLCs mainly depends on the available active surface sites for electrolyte ion adsorption/desorption, pore structure of the active material and the conductivity of the material, which affects the transfer of electrolyte ions and electrons. Therefore, high-surface-area of porous ultrafine graphite powder used as electrodes to obtain higher EDLC. As from carbon based EDLC'S, we can obtain high power density and attain outstanding cycling stability, but system suffer from low energy density due to a limited specific capacitance of carbon materials [116], [119]. Two different graphite electrodes based symmetric devices were assembled in planar configuration and electrochemical performance was evaluated for both devices in flat position as well as in bending conditions. Standard cyclic voltammograms were recorded at different sweep rates (10, 50, 100 and 200 mV s^{-1} respectively), as shown in Figure 3.6a in a voltage window of 0.5 V. The capacitance of the cell is computed following the procedure described in chapter 2, using equations 2.4, 2.5, 2.6, 2.7 and 2.8 respectively. The specific capacitances computed is 8.88 F g^{-1} for free device and 8.70 F g^{-1} for the device integrated into textile at 10 mV s^{-1}. These data established that the full charge storage capacity of the SCs device maintained after being incorporated into the textile (plane) as shown in Figure 3.6b along with high magnified microscopic images. Figure 3. 6b shows the comparison of the specific capacitance as the function of the scan rate for both plane as well as bended devices. It is depicted from the plot that there is insignificant variation in the specific capacitance of the device under different stress levels in bending position. The small variation in the specific capacitance performance (lower than 8 %) can be attributed to inefficient contact between current collector and active material while in bending condition causing the change of surface exposure of the electrodes (less surface area exposed for charge storage), which diminishes the specific capacitance of the material.

3.4.2.2 ZnO/graphite composite electrodes

A symmetric device of graphite/ZnO based electrode are assembled, and CV characterizations are performed to study the effect of the ZnO nanoparticles on the capacitance recorded at different sweep rates (10, 50 and 100 mV s^{-1} respectively) in a working voltage window ranging -0.5 V to 0.5 V. The composite slurries of various ratios of graphite and TMO's are prepared by adding: 1, 5, 10 and 20% of ZnO upon weight of graphite respectively. The CVs are recorded at 10 mV s^{-1} for different ratios of graphite/ZnO nanocomposites as shown in Figure 3.7a. The curves show distorted conventional rectangular shape behavior (brinjual like

shape of CV) due to ohmic like contributions [120], without discrete Faradaic redox peaks imputable to the intercalation and de-intercalation of sodium ions in the bulk of the ZnO from the electrolyte. Indeed, the enhanced performance of the nanocomposite by increasing the amount of the ZnO nanoparticles attributed to the combined effect of the EDL capacitance and PC related with surface redox-type reactions in the TMOs [119].

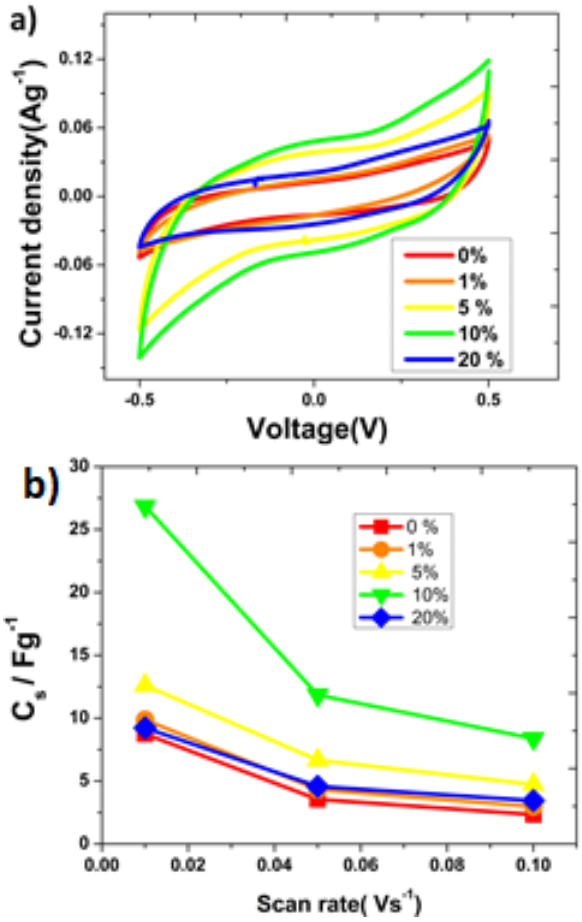

Figure 3.7 (a) Shows the CVs recorded at 10 mV s^{-1}, b) comparison of specific capacitance vs scan rate of varying the ZnO amounts. (Reproduced copyright permission) [116]

The voltammograms comparison of all the composite slurries show that the composite electrode with 10 % of ZnO nanoparticles gives the best electrochemical performance. This indicate a substantial enhancement in capacitance performance at this ratio, but when the ratio of the TMOs nanoparticles increased to 20 % ZnO nanoparticles, the area of the cyclic voltammogram is reduced and semiconductor behavior become prominent and hence results in low specific capacitance. In comparison to pristine graphite electrodes, graphite/ZnO composite electrodes exhibited remarkable increase in specific capacitance, i.e. 350% higher values. Figure 3.7b shows the specific capacitance as the function of the scan rate, exhibiting strikingly high value of specific capacitance for a fiber-shaped SCs: 27 F g^{-1} at 10 mV s^{-1} for slurry comprising 10 %

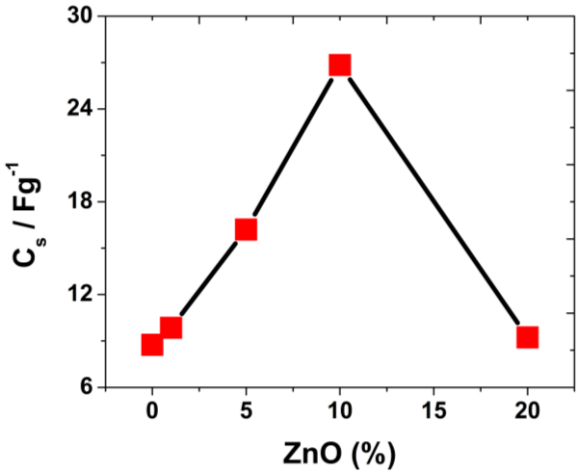

Figure 3.8 Shows the trend of specific capacitance vs various amount of ZnO. (Reproduced copyright permission) [116]

of ZnO nanoparticles. These specific capacitance values are also in agreement with the literature [121]–[124]. In comparison to graphite specific capacitance, ZnO nanoparticles give four-time higher specific capacitance, since nanoparticles offer more favorable sites for pseudocapacitive redox reactions. This porous structure of graphite /ZnO nanocomposite electrodes permit the charge particles to diffuse easily into the bulk of the structure of the electrodes active material and the addition of the ZnO nanoparticles show synergic effect and the total specific capacitance of the device increases up to 10 % of ZnO concentration in graphite. However, it reduced exponentially, when amount of ZnO nanoparticle increased to 20 % as shown in Figure 3.8. This decrease of specific capacitance can be attributed to the bigger agglomerates of the ZnO nanoparticles on the graphitic surface (as shown in the Figure 3.2a-b). These aggregates of ZnO nanoparticles forms a non-conducting layer on the surface of the graphite, increasing its resistance and decreasing its charge storage capacity [116]. Moreover, these aggregated layers are linked to the surface area of the electrode and limit the interaction sites of the active material for electrolyte ions adsorption on electrode surface. It is also described from Figure 3.7b that specific capacitance is a function of the scan rate, as we increase the scan rate, the specific capacitance decreases, because at higher scan rates, electrolyte ions have limited time to diffuse into pores of active electrode material. This will lead to lower storage capacity and results in lower specific capacitance [116].

3.4.3 Galvanostatic charge/ discharge & Cyclic stability

Cyclic stability is most important feature for commercial application of the SCs, so galvanostatic charge/discharge technique is used to demonstrate the cyclic-stability of the SC devices [116]. These measurements are performed at constant

current of 10 µA between working voltage window ranging from 0 V to 1 V. The measurements are performed to check stability for different cycles; e.g. 100, 200, 300, 400 and 500 cycles respectively and device exhibits a capacitance retention of above 95%, even after 500 cycles as depicted in Figure 3.9a. These findings designate that a nanocomposite comprises graphite with ZnO nanoparticles and gel-polymers electrolyte (PVP/NaCl) establish high specific capacitance as well as high cyclic stability. Galvanostatic constant current charge/discharge characterization are also conducted on the optimized electrodes (10% ZnO nanocomposite) at various currents, 10, 100, 500 µA respectively as shown in Figure 3.9b [119]. The charge and discharge plot exhibited almost perfectly triangular symmetric shape at all currents. Specific capacitance has also been computed using equation 2.6 and achieved a specific capacitance of 27.45 Fg^{-1}, at 500 µA current.

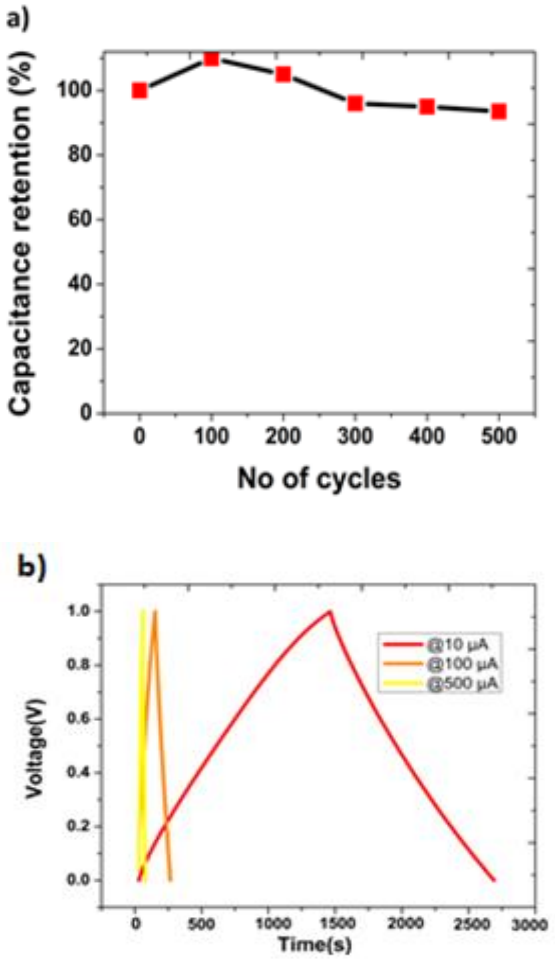

Figure 3.9 (a) Show capacitance retention of the device against no of cycles, (b) charge/discharge cycles at three different current density for 10 % ZnO device. (Reproduced copyright permission) [116]**.**

3.4.4 Supercapacitors in parallel configuration

Supercapacitors, like any electrical components, can be connected to other electronics elements either in series or in parallel configuration depending on its applications [114]. Sometimes it is useful to connect several SCs in parallel in order

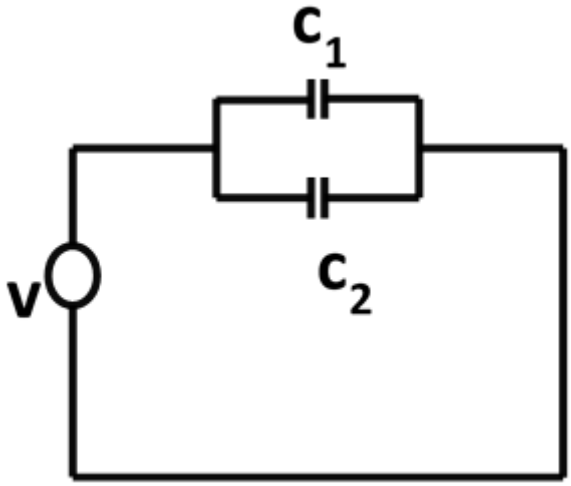

Figure 3. 10 Schematic of the parallel supercapacitors

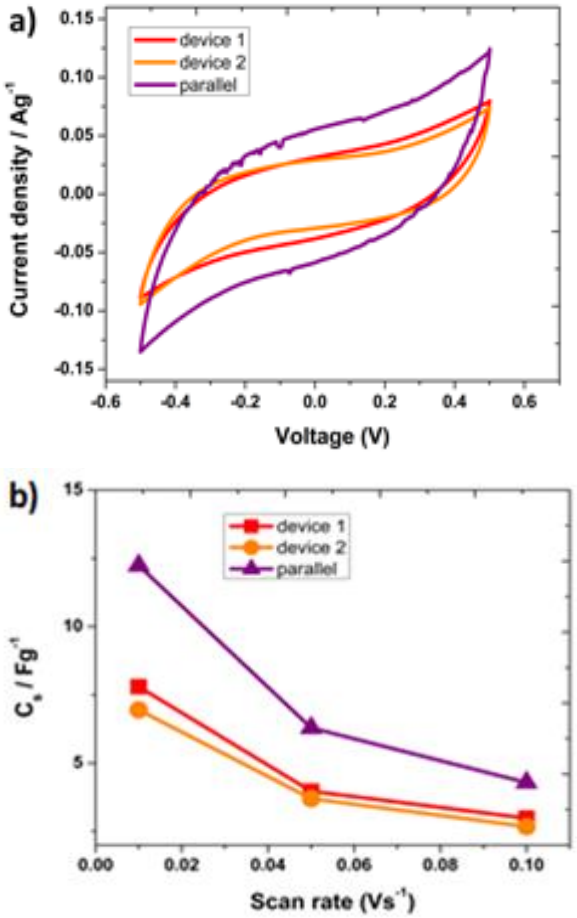

Figure 3.11 a) CVs comparison of current density vs voltage of the parallel supercapacitors, b) comparison of the capacitance as function of scan rates.

to make a functional block such as the one in the Figure 3.12a in order to investigate their properties. In such cases, it is important to know the equivalent capacitance of the parallel connection block. From the CV curves, the output current of the two parallel connected units were measured at 10 mV s^{-1} and it is found that

Table 3. 1 Summary of specific capacitance of parallel configuration

Scan rate (V s^{-1})	C_s / F g^{-1}	C_s / F g^{-1}	C_s / F g^{-1}
	Device 1	Device 2	Parallel Device
0.01	6.95	7.79	12.23
0.05	3.70	3.97	6.29
0.1	2.69	2.98	4.29

current has increased by almost a factor of two as compared with a single unit shown in figure 3.13a-b and also, total capacitance of the device is almost double the capacitance of individual electrodes. Current densities for all capacitors remain same but overall capacitance density doubled, as summarized in Table 3.1. This designated that our devices follow the theory of typical parallel capacitors [114].

3.4.5 Bending stability

In order to fabricate a fully developed fiber-based supercapacitor, it is necessary to check the stability of the SCs in bending conditions, verifying that fibers SCs does not lose capacitance during Bending conditions [125]. Flexibility is one of the core property for wearable SCs because, when it is integrated into textile, it is prone to multiple stresses. In order to study the effect of repeated bending stresses on device performance and its performance degradation, I conducted several bending tests under various stress levels and the results are shown in Figures 3.10a-b. The fiber-shaped SC is bended at various stress levels (bending angle) starting from 30^o up to 180°, then planarized and then bent again at 180° [119]. The device showed a retention of almost the 80% of the initial capacitance value under these severe stress levels. These results of bending stability are very promising for the further integration of such devices into textile and in agreement with hitherto reported performance of wearable SCs in bending conditions [125].

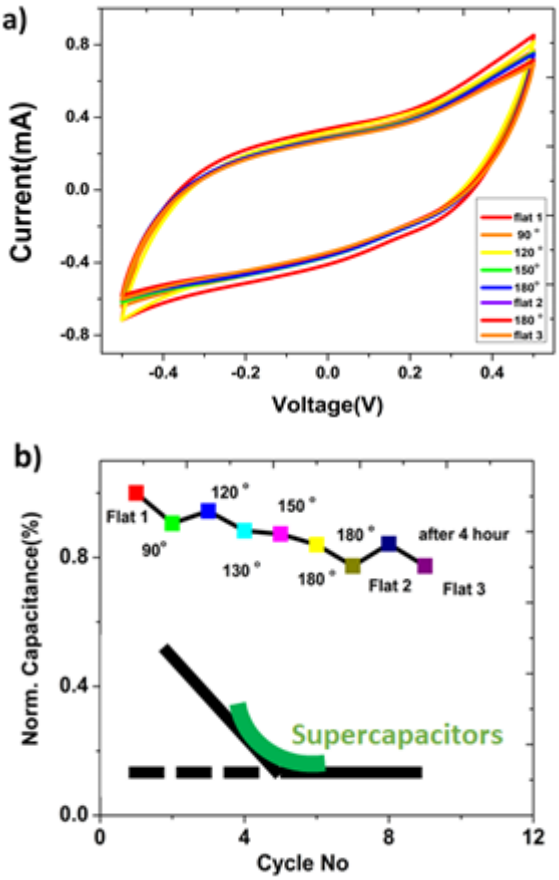

Figure 3.12 a) CVs of first measurement to last measurement of repeated bending, b) normalized capacitance at different bending angles (inset shows bending at 60°). (Reproduced copyright permission) [116]

The values of power density and energy density were also computed for both pristine graphite-based electrodes and graphite/ZnO composite electrodes using

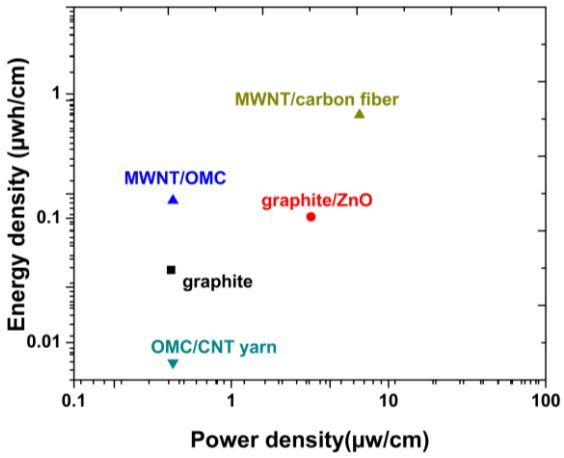

Figure 3.13 Show the Ragone plot and comparison of results with other fiber-shaped SCs from the literature. (Reproduced copyright permission) [116]

equations 2.8 and 2.9. A Ragone plot is drawn in order to compare the result of wire-shaped SCs in gel-polymer electrolyte as shown in Figure 3.11. The results of the specific energy and specific power are comparable with other flexible material used as electrode for the flexible wire-based SCs and graphite/ZnO composite electrode offers higher power density than OMC/CNT yarn [126] and MWNT/OMC electrodes [127] and comparable to MWNT/carbon fibers [128].

3.5 Conclusion

Composite electrodes of graphite/ZnO nanoparticles are fabricated and wire-based SCs are successfully assembled. The structural analysis and electrochemical properties of the graphite/ZnO nanocomposite electrodes are investigated. In comparison with the pristine graphite electrodes, the graphite/ZnO nanocomposite electrodes demonstrated an enhanced electrochemical performance. The electrodes with 10 % of ZnO demonstrated almost 4-time higher specific capacitance than pristine graphite electrodes, and almost same improvement factor is achieved in energy density and power density. Furthermore, it is found that SCs devices maintain good cyclic and bending stability in repeated bending condition. The performance of the SCs devices was also evaluated by connecting them into parallel configuration and devices have shown almost double current density and specific capacitance. All improvements described above are achieved by simple strategies in the fabrication process.

This study offers useful basis to employ other high porous carbon materials with various other TMOs or dicalcogenides to improve the specific capacitance of the wearable wire-based PCs.

Chapter 4 Electrodeposited MnO_2 nanoflakes on carbon fibers for SCs

"Work, finish and Publish".
—— Michael Faraday.

In recent past, a countless attention has arisen on the advancement of cost-effective, non-toxic and environment friendly substitute materials [129], [130], such as manganese dioxide, used as alternative to the expensive ruthenium oxide [131]. Since manganese oxide-based electrodes have a high theoretical capacitance (approx. 1400 F g^{-1}), low-cost, natural bounty and good environmental compatibility [132], [133]. The combination of these two active materials (carbon fiber and manganese dioxide) provide a synergic effect to significantly improve the supercapacitor performance [131]. Additionally, using a pseudocapacitive material such as manganese dioxide with CFs as composite electrode material with a gel-polymer electrolyte permits to elucidate the draw backs of electrolyte fading and large size of the devices employing a liquid electrolyte [134] in commercial applications [135].

4.1 One step electrodeposition (ED) of MnO_2

4.1.1 Introduction

In this study, a simple approach is used to synthesize composite electrodes comprising of MnO_2 nanosheets deposited on carbon fibers by an anodic ED method without any template and binder. Here, the core CFs serves as both current collector and structural spine for the MnO_2 active material. Two electrodes parallel configuration is used to assemble a semi-solid-state SC, with gel-polymer electrolyte acting both as ion mediator and separator. The effect of both the electrodeposition current density and time on the MnO_2 mass deposited and corresponding electrochemical performance of the devices are fully investigated, along with the electrolyte composition. Thanks to these attributes, the composite shows a high specific capacitance, enhanced rate capability, excellent cycling and bending stability. Part of this work is already published [136].

4.1.2. Experimental section

This section contains details about the ED, fabrication of electrode and assembling of the device.

4.1.2.1 Electrode

There are three electrodes in the experimental set up during ED process: reference, counter and working electrode respectively. CFs are inert, thus remain stable during electrolysis process against corrosion. Counter electrode is used to control the current flux passing through the working electrode in equal magnitude but in opposite direction to CFs. Reference electrode is used to maintain the constant over-potential throughout the deposition process [137].

The working electrodes used here have 3 cm length CFs substrate and they are purchased from Panex® 35, ZOLTEK. Prior to ED, the CFs are washed with a solution of water, ethanol and acetone with 1:1:1 ratio to remove wax and dried at room temperature. Platinum mesh is used as counter electrode for electrodeposition of MnO_2. Silver/Silver chloride (Ag/AgCl) was used as reference electrode for ED.

4.1.2.2 Materials

All the reagents and chemicals used for the preparation and synthesis of MnO_2 are of analytical grade and used as received without any further cleansing. The reagents and chemicals used for synthesis are: manganese acetate tetrahydrate Mn $(CH3COO)_2.4H_2O$ > (98 % Sigma-Aldrich), Na_2SO_4 (98% Sigma-Aldrich), distilled water. Polyvinyle Alcohol PVA (Mw 89,000-98,000, 99 % hydrolyzed Sigma-Aldrich) and NaCl (Sodium chloride, ≥99%, AR grade Sigma-Aldrich) are used for the preparation of the gel-polymer electrolyte.

4.1.2.3 Electrode preparation setup

All the manganese dioxide-based electrodes were prepared by ED both galvanostatic and potentiostatic techniques using a (Bio-Logic potentiostat, VMP-300). The

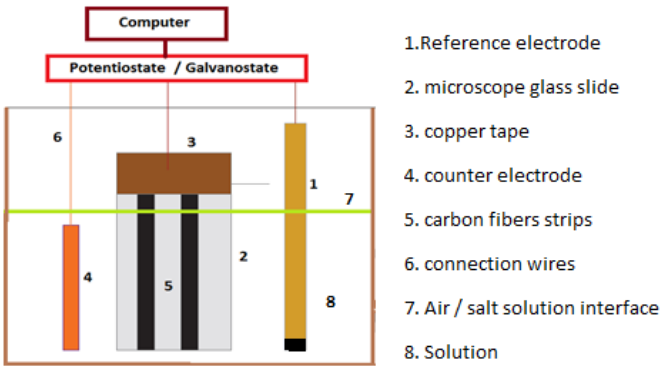

Figure 4.1 ED set up

ED set up comprises CFs substrate as working electrode, Platinum mesh as counter electrode and Ag/AgCl as reference electrode as shown in the Figure 4.1. After MnO_2 deposition, all the electrodes are washed with deionized water thoroughly

and calcinated at 300 ^{o}C for 1 hour at ramp rate 1 ^{o}C /min and cooled down to room temperature.

Fabrication of electrodes

Manganese dioxide covered CFs were obtained by electrochemical deposition. Initially both potentiostatic and galvanostatic approaches are exploited: in the first technique, a constant potential is applied to the working electrode and current response is monitored, while in the latter the current is set as a constant parameter and the potential is mutable. With the deposition time increasing, potential tends to somewhat increase in galvanostatic approach, whereas current decreases in potentiostatic arrangement, owing to the increase in the deposited oxide layer, which results in increase in the electrical resistance. Figure 4.2 displays the 3D scheme of the three electrodes arrangement (details on the electrode connection are shown in Figure 4.1). Better results were obtained with galvanostatic process, thus manganese dioxide deposition on the CFs is carried out by galvanostatic ED applying a constant anodic current of (0.7 mA) in a solution containing 0.1M manganese (II) acetate (Mn $(CH_3COO)_2$, as MnO_2 precursor, and 0.1M of sodium sulfate, as supporting electrolyte.

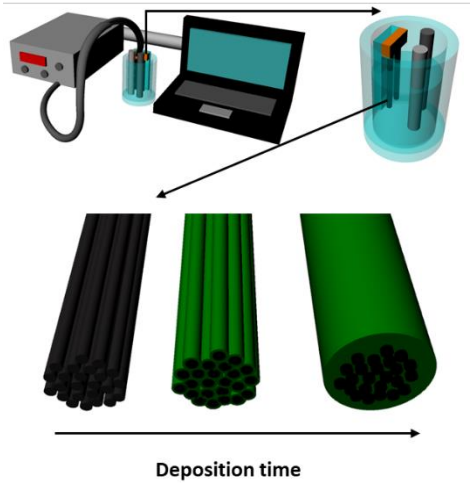

Figure 4.2 Schematic representation of the ED. (Reproduced copyright permission) [136]

Different electrode samples are synthesized, and time of deposition is optimized by varying deposition time ranging from 10 to 180 minutes at ambient condition. After the manganese dioxide deposition on the CFs, the electrodes are washed several times with distilled water and dried in ambient condition. After drying sample are subjected to calcination at 300 ^{0}C at ramp rate (1 ^{0}C/minute). The mass of the manganese dioxide deposited on the CFs substrate is evaluated by weighting the substrate before and after deposition using a microbalance (Sartorius CP225D) with capacity and accuracy of 80 and $1x10^{-4}$ g respectively.

4.1.2.4 Preparation of Gel-polymer electrolyte

The gel-polymer electrolyte is prepared by adapting the method described elsewhere [25]. Here, 1M solution of NaCl is prepared and Polyvinyl Alcohol (PVA) is added in this solution slowly while vigorously stirring. PVA + 1M NaCl gel is synthesized by dissolving 2g of PVA in 10 ml of distilled water containing 1M NaCl. After adding PVA to the solution, it is left under stirring for 4 hours on hot plate at 80 ^{o}C until homogeneous and highly viscus translate electrolytic gel is obtained.

4.1.2.5 SC Fabrication

SCs are fabricated as demonstrated schematically in the Figure 4.3. Two MnO_2 /CF electrodes are used as both current collectors and active material and the gel-polymer with dual function, electrolyte as well as separator sandwiched between two electrodes. The MnO_2 /CF electrodes are dipped into gel-polymer electrolyte for 20 minutes in order to permit a good infiltration of gel into the porous structure of MnO_2 and wrapping up of electrode. After wrapping, they are kept in ambient conditions to obtain quasi-solidification of electrolyte and then positioned onto flexible PET sheet in two-parallel electrodes arrangement. After partial gelification of electrolyte, they are enclosed in Kapton tape as packaging and bundled with copper tape to improve electrical contact for the electrochemical measurements.

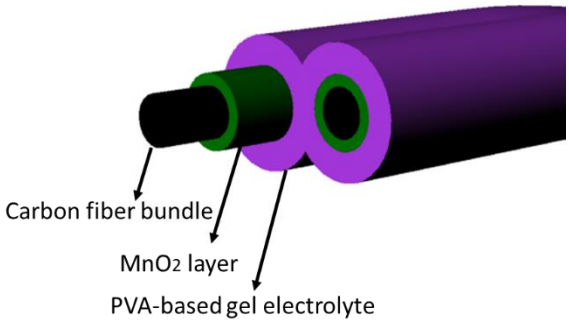

Figure 4.3 3D Schematic demonstration supercapacitor fabrication. (Reproduced copyright permission) [136]

4.1.3 Characterizations

Physical characterization (FESEM, XRD and Raman spectroscopy) performed are described in detail in chapter 3 experimental section.

TEM and STEM analyses are performed on FEI Tecnai F20 ST transmission electron microscope. Concerning sample preparation, parts of the MnO_2 layer are detached from the CFs by sonication in ethanol. Then, they are dispersed and subsequently deposited on a holey carbon copper TEM grid.

The chemical composition is investigated with a (PHI 5000) Versaprobe scanning X-ray photoelectron spectrometer using monochromatic Al [K-α] X-ray source

1486.6 (eV). The analyzed sample area is (500 (µm) × 500 (µm)). Different pass energy values are employed for survey spectra 187.85 (eV) and for high-resolution acquisitions (23.5 eV). All the spectra are acquired with simultaneous charge compensation. CasaXPS software is used for data analysis. All corelevel peak energies are referenced to C 1s peak at 284.8 eV (C-C/C-H bonds)).
The electrochemical characterization of as-synthetized MnO_2 electrodes is carried out in a two-electrode cell in gel-polymer electrolyte. The performance of the device is evaluated according to the procedure described in detail in chapter 2.

4.1.4 Result and discussion

In this section, I present details about physical characterization and discuss the results in detail. I also discuss in detail about the electrochemical characterizations.

4.1.4.1 Morphological analysis

Figure 4.2 shows the 3D schematic of electrochemical deposition of Manganese dioxide on carbon fibers. The electrochemical synthesis of MnO_2 was performed

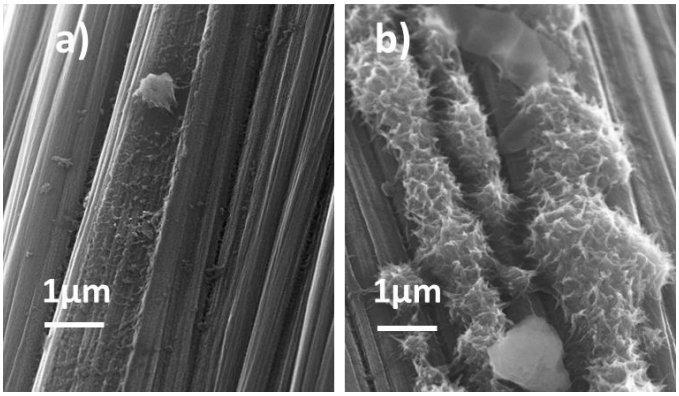

Figure 4.4 (a) Fesem images of potentiostatic, (b) galvanostatic deposition of MnO_2 [136]

initially exploiting both potentiostatic and galvanostatic techniques of deposition, the former results with very low MnO_2 coverage as shown in the figure 4.4, while the latter shows some spots of deposited MnO_2 owing to this reason, galvanostatic approach was chosen as best method and was optimized by adjusting the current density and time of deposition. The time of deposition was varied from 10 minutes up to 180 minutes to find out best time at which optimized loading of manganese oxide was obtained and consequently best electrochemical performance. The synthesized materials are firstly examined by field emission scanning electron microscopy to study the evolution of morphology with deposition time.

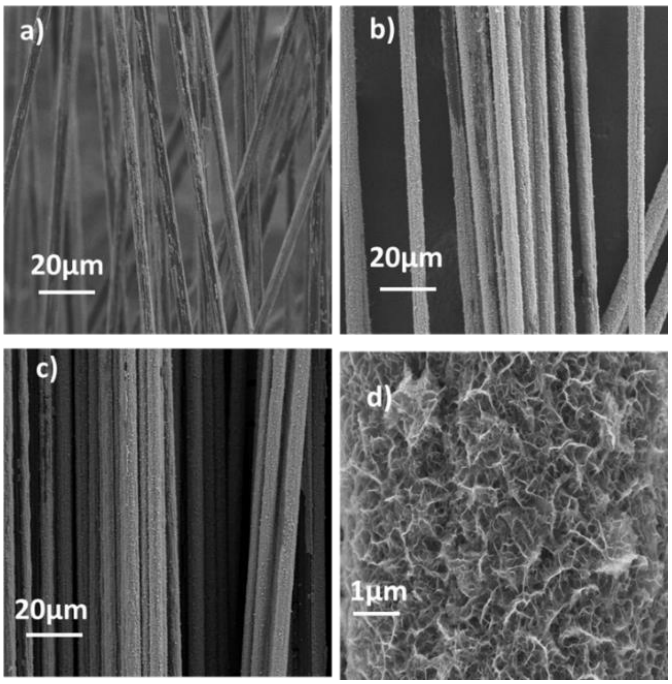

Figure 4.5 a-c) FESEM images for higher galvanostatic deposition times (30, 60, 120 min respectively) results in better coverage of the CFs with manganese dioxide layer, d) higher magnification image of 120 min deposition. (Reproduced copyright permission) [136]

As shown in Figure 4.5, the deposition time had some impact on the consistency of the manganese dioxide coverage. Precisely, full coverage of the fibers cannot be achieved at low time of deposition. For example, the 30 minutes deposited sample shows, there are regions, the external surface of the CFs is not covered by

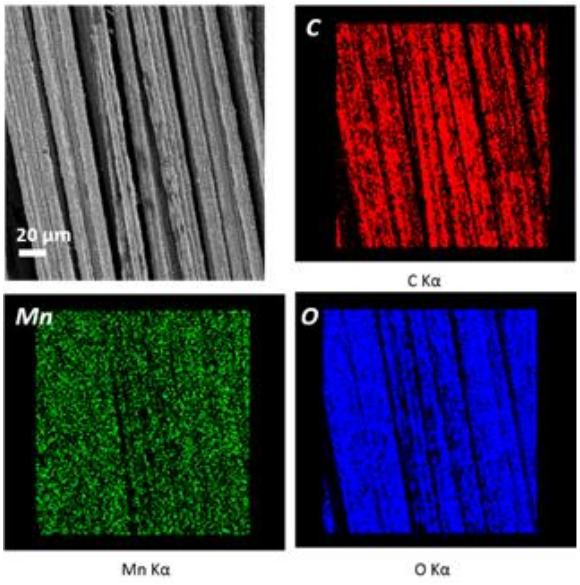

Figure 4.6 EDX mapping performed on the region shown in the FESEM image on the left. The analyzed sample was obtained with galvanostatic 120 min deposition. (Reproduced copyright permission) [136]**.**

manganese dioxide as shown in Figure 4.5a, these naked regions can be identified in low-magnification FESEM images as they have lower intensity (they are "darker") than the covered area. After 120 minutes of deposition, full coverage of the CFs is achieved, as established by FESEM imaging and by EDX mapping as shown in Figure 4.6. The variation in the coverage of the CFs at low deposition times is possibly due to the actual current density provided to the CFs, which is considerably lower than the set current density. This resulted in lower ED rates which needed longer time of deposition for the full coverage of the fibers, if compared to other flexible substrates, such as Ti foil [138]. The morphology of the nanostructured manganese dioxide layer is also examined by high-resolution imaging and it does not seem to be influenced by the time of deposition. Figure 4.5a-c are typical images of the morphology of the manganese dioxide coverage, which consists of really thin nanosheets (thickness < 10 nm, see STEM and TEM measurements in Figure 4.7a-c), as anticipated for this specific ED method, as previously stated in the literature [139], [140].

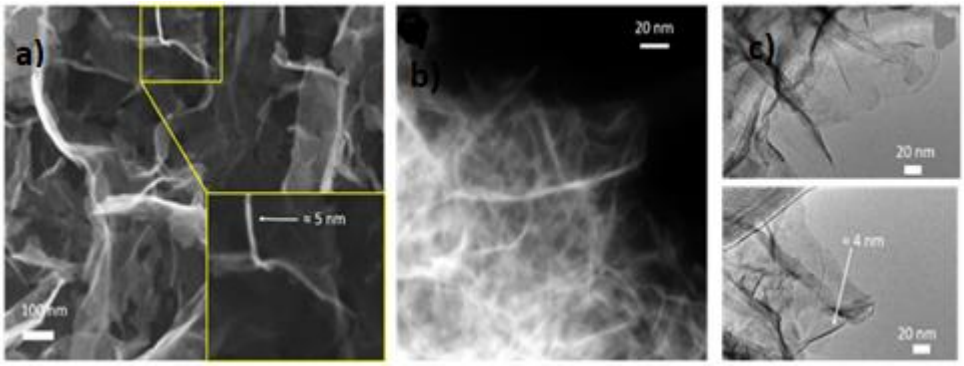

Figure 4.7 a) Show High-magnification FESEM images of the morphology of the ED MnO_2 nanoflakes, b) STEM HAADF image of the MnO_2 nanosheets, c) TEM images of various regions. (Reproduced copyright permission) [136]

4.1.4.2 physical characterization

XRD and Raman

Some insights on the crystal structure characteristics of the material are collected with X-ray diffraction and Raman spectroscopy. XRD (Figure 4.8a) exhibit the presence of an amorphous region, with only a very feeble and wide signal at $2\vartheta \sim 37°$. Raman measurements (Figure 4.8b) illustrate characteristics from both MnO_2 in the 200 - 800 cm^{-1} region and from CFs in the 1200 - 1700 cm^{-1} region. In general, it is well-known that manganese dioxide in their several crystalline phases exhibit Raman signals associated with the motion of the oxygen atoms within the MnO_6 octahedral units in manganese dioxide [140]. In particular, this material demonstrated a strong phonon band around 650 cm^{-1} (associated with A_{1g} spectroscopic species with Mn−O symmetric vibrations) and a weak phonon band in the region 200 - 500 cm^{-1} range with no explicit resonances (a fuse of Mn-O symmetric vibrations and Mn- O bending vibrations). These properties of materials are well-

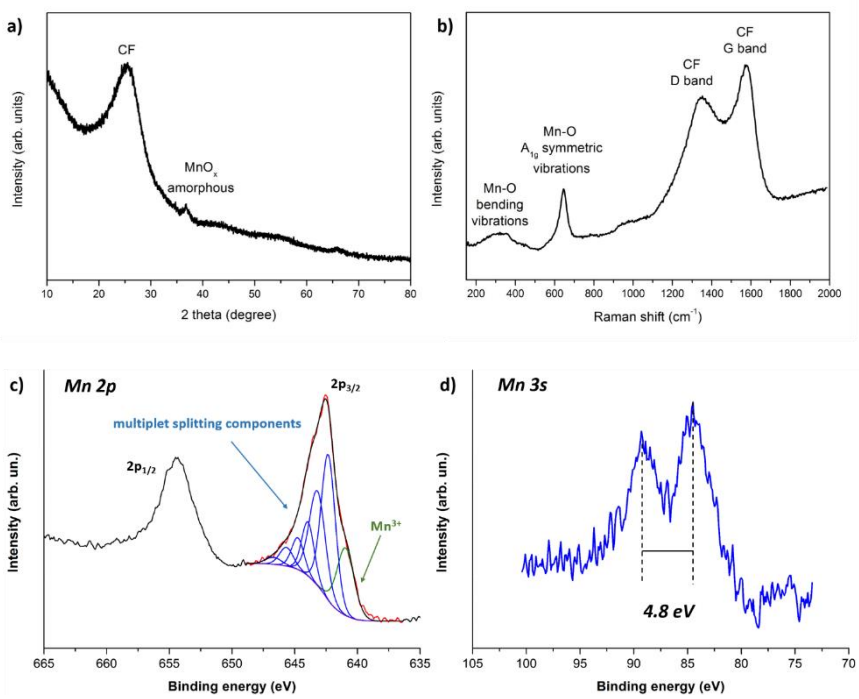

Figure 4.8 (a) XRD spectrum from MnO_2/CF sample (JCPDS references for α-MnO_2: 44-0141), (b) Raman spectrum from MnO_2/CF sample, (c) XPS high-resolution scans of Mn 2p, (d) Mn 3s regions of the photoelectron spectrum for the MnO_2/CF sample. (Reproduced copyright permission) [136]

matched with the synthesis of an amorphous material, in-line with XRD findings. At higher wavenumbers, the characteristics peaks D and G from CFs are designated at ~1350 cm^{-1} and ~1580 cm^{-1}, respectively.

X-ray photoelectron spectroscopy (XPS)

XPS measurements are performed to study the surface chemical composition of ED manganese dioxide. This characterization permits the identification of MnO_2, since there are characteristics of the XPS spectra which are sensitive to the oxidation state of manganese. Precisely, the two most vital regions of the XPS spectrum for the identification of MnO_2 phases are Mn 2p and Mn 3s. Regarding Mn 2p area, a multiplet structure is anticipated to arise for Mn^{+2}, Mn^{+3} and Mn^{+4} owing to the existence of unpaired d electrons [141]. The specific multiplet structure depends on the oxidation state and it can be employed for phase identification. Furthermore, more information can be achieved from shake-up characteristics: e.g, MnO displays a clear shake-up constituent at the higher binding energy side of the $2p_{3/2}$ peak [142]. In the case of the MnO_2 /CF electrode, the peak structure of the Mn 2p area (Figure 4.8c) is indicative of manganese dioxide: the existence of multiplet splitting constituents, the nonappearance of a shake-up satellite adjacent to the $2p_{3/2}$ peak and the overall shape of the convoluted spectra agrees with reports published in the literature [143], [144]. In agreement with the previously

mentioned reports, low binding energy peak is not considered as a multiplet splitting element but it is ascribed to Mn^{3+}, since this peak does not appear from theoretical computations of multiplet structure of core 2p levels for manganese [141]. Concerning the Mn 3s region of the photoelectron spectrum, multiplet splitting is responsible for the existence of two main peaks, whose binding energy difference can be used for phase recognition. For the evaluated sample, a binding energy difference of about 4.8 eV is well-matched with the manganese dioxide phase, rendering to previous reports [145], [146].

4.1.4.3 Electrochemical characterization

Two-parallel wire configuration wearable devices are assembled employing a gel-polymer electrolyte with dual functionality, acting as a separator and ion mediator (a 3D schematic of the fabricated device is shown in Figure 4.3). The electrochemical performance of the MnO_2/CF composite electrodes is studied by CV and constant current charge/discharge measurements, while all the energy storage parameters can be computed by the equations reported in detail in chapter 2. The assembled devices with electrodes containing 10 minutes deposition of manganese dioxide using both techniques (potentiostatic as well as galvanostatic), and electrochemical characterizations were performed in both cases. Figure 4.9a, shows the comparison of cyclic voltammograms of the galvanostatic deposition at different scan rates. It is observed that galvanostatic deposition shows better electrochemical performance as compared to potentiostatic deposition. This is because MnO_2 by potentiostatic shows very low mass loading and more compact while galvanostatic deposition, gives higher mass loading which are less compact and greatly separated from each other [147]. In galvanostatic deposition of MnO_2, it is observed that the potential of deposition gradually decreases with passage of time, owing to the higher friction effect resulting from the deposition of MnO_2 on the cathode and the interaction of ions moving in cathodic direction with the ions electro-transferred in anodic direction. This reduction of voltage reduces the diffusion rate of MnO_2 to the cathode surface and decreases deposition rate, thus I obtained MnO_2 layered structure with less compact nanosheets, as shown in FESEM images [148]. It is also observed that for galvanostatic deposition CVs exhibit larger and semi-rectangular shape at lower scan rates with ideal symmetry signifying good charge transfer within nanostructure as compared to potentiostatic deposition. The better spacing between nanosheet or nanoflakes and low compactness leads to better diffusion of electrolyte, which results in higher current and specific capacitance [148].

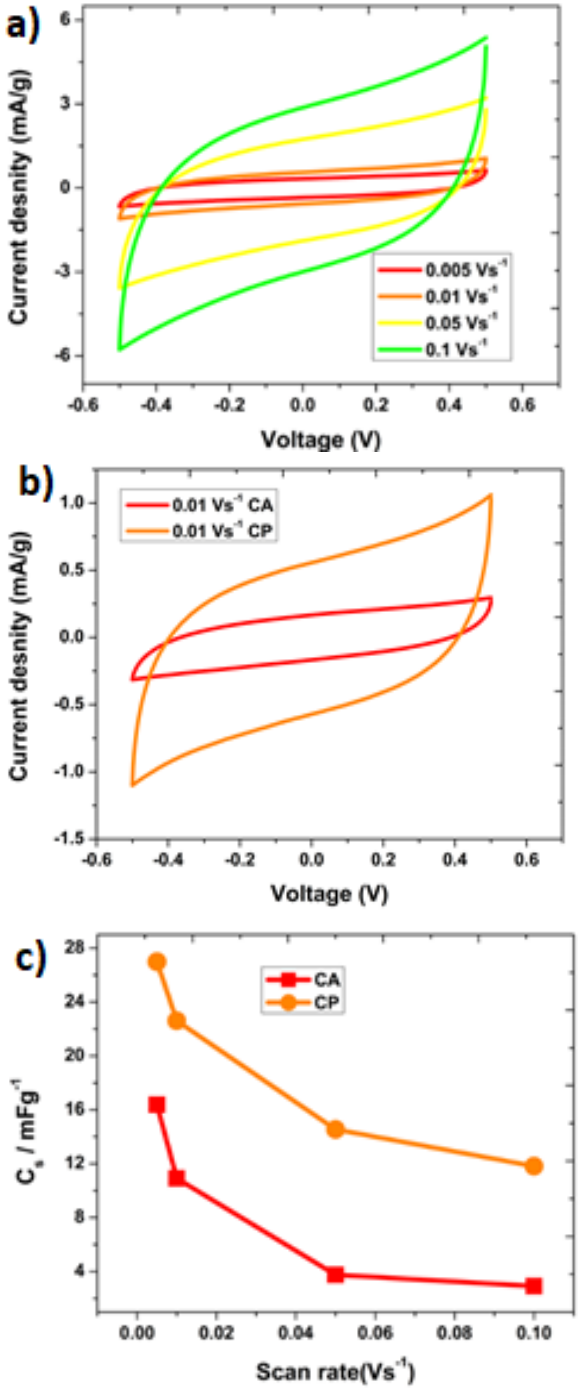

Figure 4.9 a) Comparison of CVs obtained at various sweep rates for galvanostatic deposition, b-c) comparison of CVs and specific capacitance for both galvanostatic and potentiostatic. (Reproduced copyright permission) [136]**.**

As it is clear from the Figure 4.5b, CFs are not completely covered at this current and time. So, I doubled the current and also increased time to optimize the coverage and electrochemical performance. As shown in Figure 4.10a-c, the time of deposition sturdily affects the capacitive performance of the SC device, with a noticeable increase of the current in the CVs and results in increased specific capacitance, respectively.

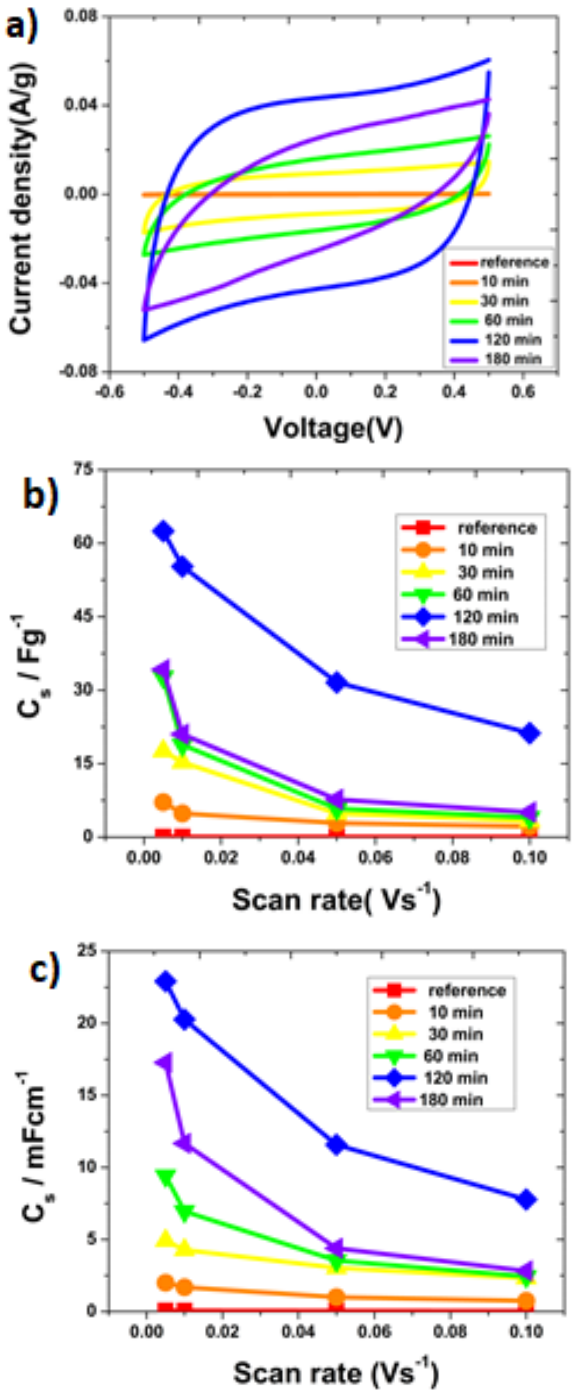

Figure 4.10 a) CVs comparison recorded at 5 mV s^{-1} on electrode synthesized at various times of deposition: 10, 30, 60, 120 and 180 minutes, b-c) show a plot of the specific capacitance as function of sweep rate the for various devices in F g^{-1} and (mF cm^{-1}) respectively. (Reproduced copyright permission) [136]**.**

Even, if the manganese function as pseudocapacitive materials, there are no oxidation/reduction peaks sited in the CVs. These results agree with many other reports, since MnO_2 PC is owed to fast and reversible faradaic interactions, which include the electrochemical interconversion between Mn (IV) and Mn (III) in the solid, and corresponding insertion of cations from the electrolyte [149]. The maximum specific capacitance obtained at 5 mV s^{-1} is computed (using equation 2. 4

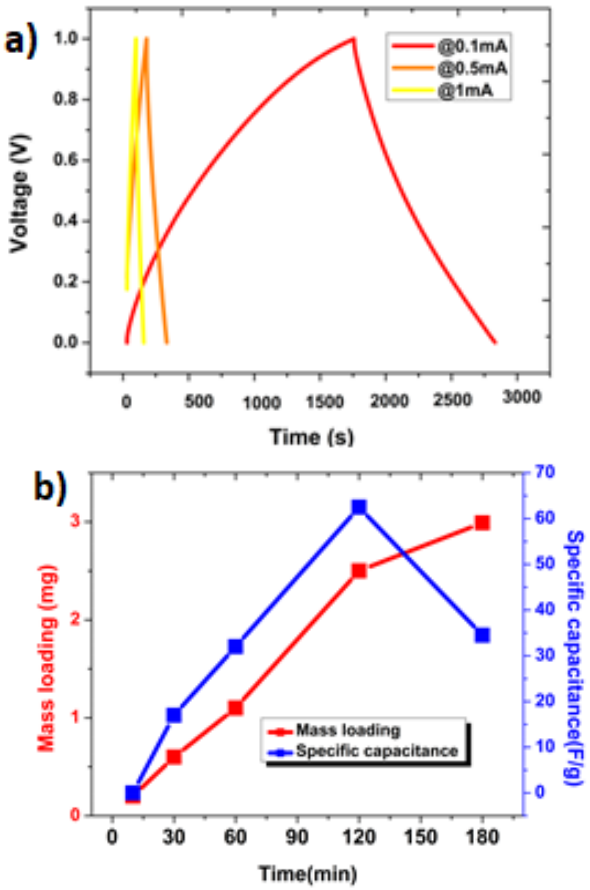

Figure 4.11 a) Comparison of constant current charge/discharge measurements at various current densities for 2 hours deposited device, b) comparison of specific capacitance and mass loading vs time of deposition. (Reproduced copyright permission) [136]**.**

and 2.5 respectively) to be 62 F g^{-1} as gravimetric capacitance, and 23 mF cm^{-1} as length capacitance for the two-hour deposited MnO_2 electrodes, which is almost 4 orders of magnitude higher than the pristine CFs (0.02 F g^{-1} and 0.06 mFc m^{-1}, respectively) as can be seen in comparison in Figure 4.10b-c. This value is also much higher than other recently published composite electrodes such as RGO-MnO_2/ RGO (22 Fg^{-1}) [134] or CNT@MnO_2 /CNT (12.5 F g^{-1}) in PVA based gel-polymer electrolytes [150]. Constant charge-discharge measurements were also performed as shown in Figure 4.11a exhibiting a good triangular profile. In order to highlight the effect of the manganese dioxide deposition, Figure 4.11b demonstrate the trend of the specific capacitance vs the MnO_2 loading on the CFs. The specific capacitance is also computed by using the equation 2.6 from the constant current charge and discharge measurements and the specific capacitance is 62.5 F g^{-1}.

It is a common thought, that the charge transfer resistance, ohmic resistance (active material and electrolyte) and mass transfer resistance can influence the capacitive performance of the electrodes [151], [152]. By employing nanostructures as active materials, some of the aforementioned factors may become insignificant because these active materials deliver both, high specific surface area and fast redox reaction for charge transfer. Thanks to their micro/nano attributes, the MnO_2

/CF composite electrodes structure not only ease a fast penetration of the cations between electrode and electrolyte, but they are also helpful to overcome the poor electrical conductivity of the MnO_2, both of which results in enhanced electrochemical performance of SCs [149]. The capacitive performance for the 180-minutes of deposition of manganese dioxide is lower than the 120-minutes of deposition time, since the increase in time of deposition has increased the corresponding mass loading which results in thick manganese dioxide layer on CFs (as shown in Table 1 in CFs and MnO_2 ratio) and possibly only a layer of manganese

Table 4.1 CFs to MnO_2 mass loading ratio

Time of deposition(min)	Mass of MnO_2 deposited(mg/cm)	Ratio (CF: MnO_x)
10	0.2	1: 0.011
30	0.6	1: 0.033
60	1.1	1: 0.061
120	2.56	1: 0.14

dioxide is charged and discharged during SC testing, resulting in a reduction in the energy storage behavior [125]. This confirms that capacitance of the active material (manganese dioxide) is strongly reliant on the loaded mass and the thickness of the film of material involved in the synthesis of the electrodes [149].

4.1.4.4. Effect of temperature on electrochemical performance

The effect of calcination temperature i.e. 500 ^oC on the electrochemical performance of the manganese dioxide was also studied. After synthesis of electrode and calcinating at 500 ^oC, electrochemical characterizations were performed. The comparison was drawn between the electrodes which are ambient dried, calcined 300 ^oC and 500 ^oC. It is observed that specific capacitance exhibits a 50% decrease, as shown in the Figure 4.12. According to Mao et al. [153] electrodeposited MnO_2 usually has inbound water content which has a appreciated effect on the specific capacitance by enhancing the transport of the active ionic species. The calcination treatment at 500 °C causes an evaporation of the inbound water content, decreasing ionic transport properties and resulting in lower specific capacitance, as supported by the experimental data.

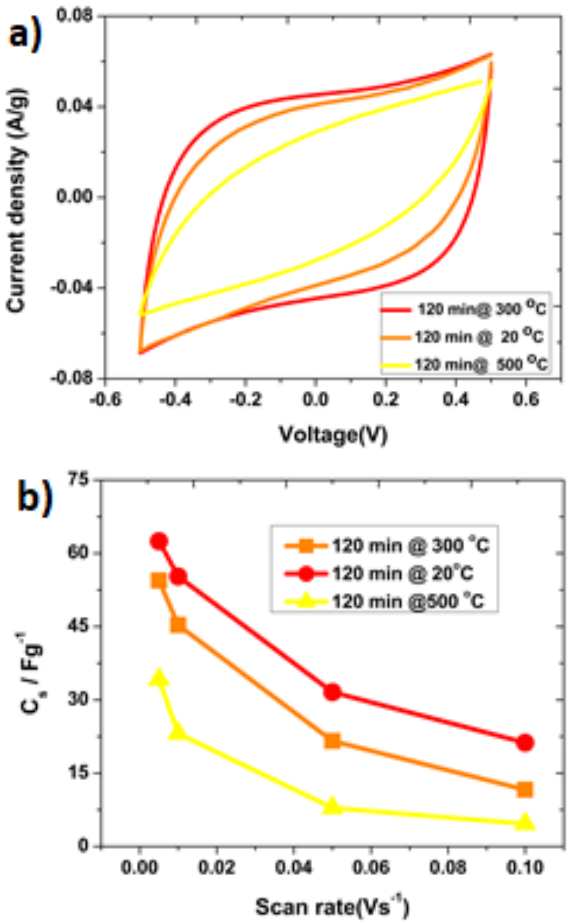

Figure 4.12 a) CVs comparison of samples calcinated at different temperatures, b) specific capacitance vs scan rate. (Reproduced copyright permission) [136]

4.1.4.5 Cyclic stability

Cyclic stability is considered one of the most important attributes of SC devices practical applications. Long-term cyclic stability of the device was tested by CV in a voltage window of 0.5 V for 10000 cycles at 50 mV s^{-1} scan rate. The SC still has 90 % specific capacitance of initial capacitance after 10000 cycles as shown in Figure 4.13a-c. CVs are also plotted to show the degradation after various cycles and found a slight change in voltammograms which demonstrated that device has excellent cyclic stability. This also exhibits that the devices with gel-polymers electrolytes PVA+NaCl evade loss of specific capacitance by averting the evaporation of the electrolyte [152].

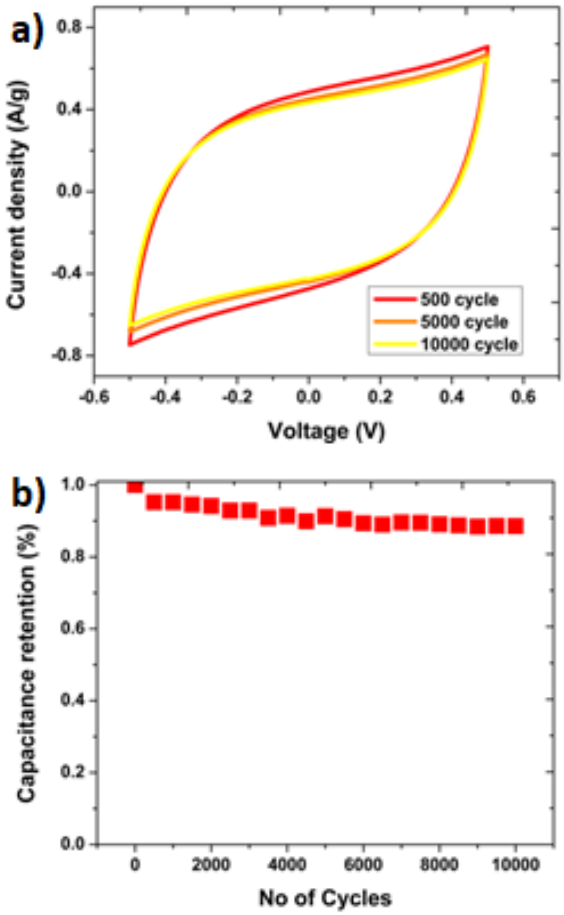

Figure 4.13 a) Comparison of CVs at various cycles, b) capacitance retention vs no of cycles after 10000 cycles. (Reproduced copyright permission) [136]

4.1.4.6 Bending stability & Ragone plot

In addition to smaller size, light weight, and higher flexibility, a supercapacitor must have mechanical stability so that they can be deformed to almost any anticipated shape, knotted or even weaved into textile [154]. Because, in their extended life cycles, these delicate fiber shaped SCs unavoidably suffer from various local stress under bending and other deformations, which is a real problem for wearable SCs in practical applications which may cause to a permanent mechanical deformation over time. This inevitable failure would seriously limit the lifecycle and reliability of the supercapacitor, resulting in a failure of the whole device [155].

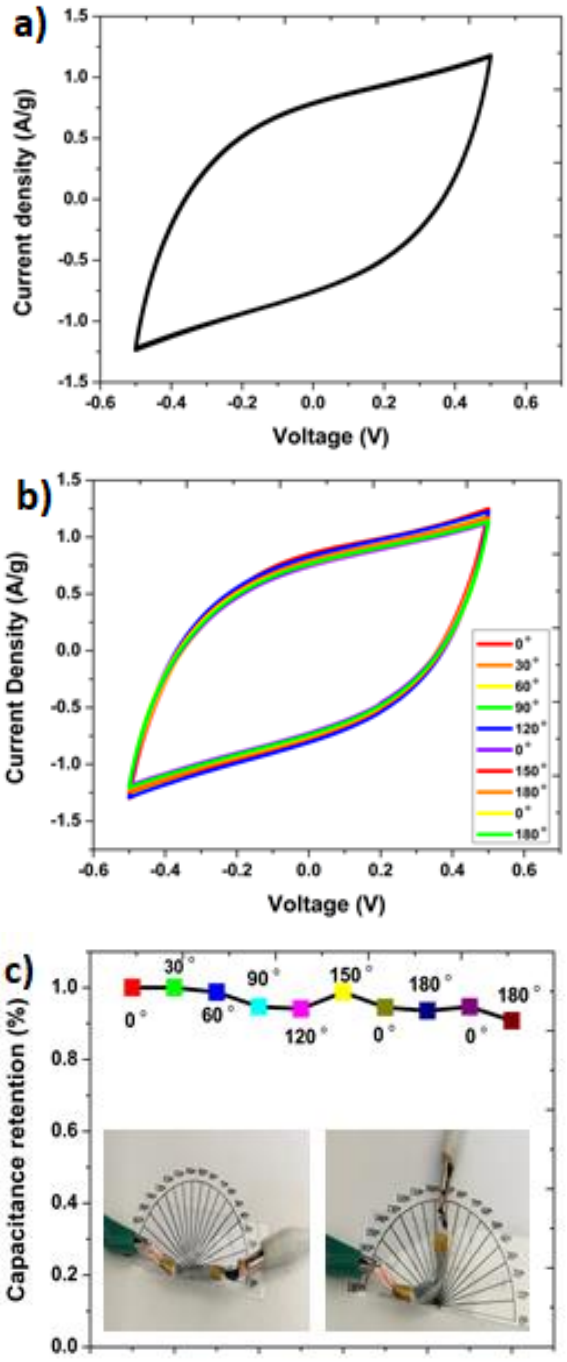

Figure 4.14 a) CVs recorded at 90° bending angle of 20 cycles, b) comparison of CVs recoded at different bending angles, c) capacitance retention vs bending angles (in set shows assembled device. (Reproduced copyright permission) [136].

After performing the electrochemical characterization of assembled devices, mechanical stability under different mechanical stresses has been examined. The cyclic voltammetries were recorded at different stresses levels in the angle ranges from 30 to 180 degrees, to evaluate the bending stability of the devices (photo attached inset of figure 4.14 c). CVs are plotted as shown in the Figure 4.14a-b to demonstrate stability at 90° and also comparison of CVs of all the angles. It is clear from the Figure 4.14c that capacitance retention is almost 100 % which is in

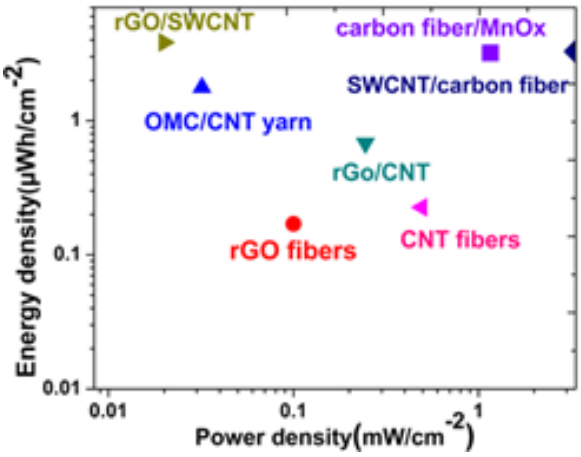

Figure 4.15 Ragone plot comparison of results with other material in PVA base electrolyte. (Reproduced copyright permission) [136]

Table 4. 2 Comparison of PVA based fiber shaped supercapacitors

Sr#	Electrodes	electrolyte	Cs (mF/cm)	E (μWh/cm)	P (μW/cm)	Reference
1	rGO	PVA/H_2SO_4	27.1	0.17	100	[156]
2	CNT fiber	PVA/H_2SO_4	.006	-	-	[157]
3	CNT fiber	PVA/H_3PO_4	.027	-	-	[158]
4	OMC/CNT yarn	PVA/H_2SO_4	1.91	0.085	1.55	[127]
5	MnO_2/rGO fibers	PVA/H_2SO_4	0.143	-	-	[159]
6	MWCT/CF	PVA/H_2SO_4	6.3	0.7	13.7	[81]
7	MnO_2/CF (Current study)	PVA/NaCl	24	1.089	129.65	This work

line with previous literature reports [125], hence exhibiting the appropriateness of the here demonstrated device to be integrated into textiles. The energy and power density values for the best performing device are computed using the equations 2.7 and 2.9 and are 530 W kg^{-1} and 1.087 Wh kg^{-1}, respectively. Ragone plot is drawn to compare the performance of composite electrode device, especially in gel-polymer electrolyte with other stated composite material as shown in Figure 4.15. It is demonstrated that MnO_2/CF composite material devices exhibit higher specific energy and power density respectively, when connected with other

carbon-based composite material devices in PVA based polymeric electrolytes as shown in Table 2.

4.1.5 Conclusion

In summary, novel synthesis of MnO_2/CF composite electrodes are obtained by galvanostatic ED of manganese dioxide nanoflakes film on CFs and fully investigated from the chemico-physical aspect. Two parallel electrodes configuration is exploited for flexible symmetric SCs with a gel-polymer acting as both electrolyte as well as separator. Constant current charge/discharge and CV measurements exhibit excellent electrochemical performance as compared to the stated literature. The dependence of the ED time on the energy storage behavior is studied and maximum values of specific capacitance and length capacitance of 62 F g^{-1} and 23 mF cm^{-1}, respectively, are achieved for two hours of manganese dioxide deposition. Finally, cycling and bending stability is investigated and the attained results demonstrate that these flexible fiber-shaped SCs possess appropriate mechanical and electrochemical performance as wearable power source for textile electronic devices.

This innovative approach permits the required large-area synthesis and offers an inimitable combination of high MnO_2 loading, binder-free attributes, open macro-/meso-porous structure, high-accessibility for the electrolyte, excellent electrical conductivity, use of cost-effective and no-critical raw materials for the EU community as well as optimum stability over the time.

4.2 2-Step electrodeposition of MnO_x

4.2.1. Introduction

The primary objective of this study is to enhance the specific capacitance by improving intrinsic kinetics, porosity and specific surface area of the material. Second objective was to use this material for asymmetric supercapacitors (ASC) to fabricate high energy devices. In this regard, single step ED MnO_2/CF electrode (detail in section 4.1) subjected to hydrogenation process to induce oxygen vacancies in the manganese dioxide film to improve intrinsic kinetics and porosity. When this material tested in three electrodes configuration, it exhibits a very resistive behavior due to cracks in the film. To counter the problem, a new approach of 2-step ED of MnO_x is used, which has not only improved the coverage of the CFs but also increases electrochemical performances of 2-step ED MnO_x. The electrodes were also synthesized by reversing the orders of steps and time of deposition to study the effect on the electrochemical performance. Herein, an effective and reliable approach is presented to intrinsically improve the conductivity and capacitance of the MnO_x by inducing oxygen vacancies (denoted H-MnO_x) on the surface of the MnO_x film by performing thermal treatment under hydrogen environment. Oxygen vacancies plays an important role in determining properties of the manganese oxides. Induced oxygen vacancies on fabricated electrodes significantly improve the conductance and the kinetics of the surface redox reactions [132], [160]–[162] because of the high porosity. In this study, I have also synthesized sodium Birnessite using in-situ electrochemical oxidation of spinel Mn_3O_4 structure, in which pre-insertion of the cations (such as Na^+ and K^+) in Mn_3O_4 strucuture can effectively improve the performance of the SCs [163].

4.2.2. Experimental section

This section contain detail information about the synthesis of the electrodes and fabrication of the devices.

4.2.2.1 Reagents

All the reagents and chemicals used for preparation and synthesis of MnO_x are of analytical grade and used as received without any further cleansing which includes manganese acetate tetrahydrate $Mn(CH3COO)_2.4H_2O$ > (98 % Sigma-Aldrich), Na_2SO_4 (98% Sigma-Aldrich), distilled water, CFs (Panex® 35, ZOLTEK), copper tape, glass microscope slides.

4.2.2.2. preparation of MnOx

MnO_x nanoflakes are first grown on CFs substrate via 2-step ED method. The ED is performed in two steps using traditional three electrode configurations with CFs as working electrode, a Pt mesh as counter, Ag/AgCl as reference electrode respectively. Prior to the ED, the CFs are cut (length 3 cm), washed in acetone, ethanol and distilled water in a 1:1:1 ratio, and blocked on microscope glass slides and are used as anode for the ED of the manganese dioxide. The end of the CFs bundle is tied up with a copper tape to enhance the electrical contact during the ED. MnO_x nanoflakes deposition on the CFs is carried out by 2-step galvanostatic ED using instrument (CHI660D electrochemical work station), applying a two different anodic current densities of (0.27 mA cm^{-2} and 0.135 mA cm^{-2} for 45 min and 75 min respectively) in a solution bath comprises 0.1M ($Mn(CH_3COO)_2$, as manganese oxide precursor and 0.1M of Na_2SO_4, as supporting electrolyte. After first deposition of the 45 minutes at 0.27 mA cm^{-2}, electrode is calcined at 150 ^{0}C for 1 hour and then second step of deposition is performed at low current density (0.135 mA cm^{-2}). The dark brown MnO_x nanoflakes film is obtained with average mass loading of 0.25 mg cm^{-1} uniformly coated on the CFs. After growth CFs are cleaned with distilled water to remove the unattached particles and calcination was done at 300 ^{0}C for 1 hour. Various samples are prepared, by varying the electro-deposition current and time of depositions at room temperature. The mass of the manganese oxide loaded on the CFs is evaluated by weighting the CFs before and after ED using a microbalance (Sartorius CP225D).

4.2.2.3. Synthesis of Mn_3O_4 by thermal reduction method

Synthesis of partially crystalline Mn_3O_4 denoted as (H-MnO_x) nanoflakes was obtained by annealing as deposited MnO_x in a furnace (Carbolite Tube Furnaces MTF 12/38/400) at 250 ^{o}C for 3.5 hours at ramp rate of 2.5 ^{o}C/min under hydrogen flux. Figure 4.16a shows the 3D schematic detail of the complete process.

4.2.2.4. Synthesis of Sodium Birnessite from Mn_3O_4 spinel structure

Birnessite is a phyllomanganate, which is a kind of manganese oxide minerals with major proportion of manganese having similar layer strucuture and dissimilar interlayer arrangement [164]. The structure of these phyllomanganate is not well-know and thought to be similar to chalcophanite which is based on sheets of edge-sharing Mn_4^+-O octahedra. The vacancies in Mn-O octahydra, create charge deficiencies which are balanced by the external cations (i.e. Li^+, Na^+, K^+) to form birnessite [164]. Sodium Birnessite is synthesized by in-situ electrochemical oxidation in which Na^+ cation was inserted into Mn_3O_4 spinel structure in the presence of saturated Na_2SO_4 solution [163], [165]. First saturated solution of Na_2SO_4 was prepared and then using same three electrodes configuration, in which H-MnO_x is used as working electrode, SCE and platinum rod is used as reference and counter

electrodes respectively. Sodium Birnessite is synthesized by cycling this H-MnO_x electrode in this electrolyte of saturated Na_2SO_4 for 500 cycles and black color $Na_{0.36}MnO_2$ is prepared.

4.2.3. Characterizations

All the physical characterization performed to confirm the morphology, crystal structure (XRD, Raman) and XPS (chemical composition) described in detail in chapter 3 and 4. Electrochemical measurements are performed in three electrode set-up using SCE and platinum rod as reference and counter electrode respectively, in a 1M Na_2SO_4 solution at pH=10.

4.2.4. Results and Discussion

4.2.4.1 Structural and morphological analysis

Free standing hierarchical structure is prepared by electrodeposition as shown in the schematic below in Figure 4.16. Mn_3O_4 nanoflakes are synthesized on CFs by three step process which involves binder and template free anodic galvanostatic ED of the MnO_x by two steps and thermal treatment in Hydrogen environment as show Figure 4.16. In our previous study [136], single step anodic ED of MnO_2 performed on CFs (detail in section 4.1), there were problems of coverage and cracks

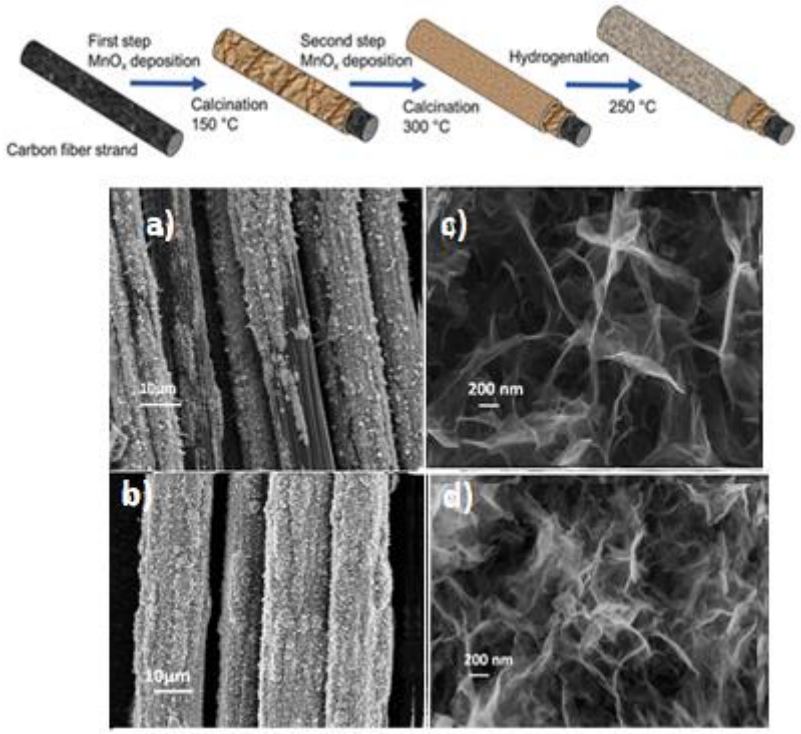

Figure 4.16 Schematic of 2-step electrodeposition of MnO_x and hydrogenation of MnO_x, a-b) FESEM images of 1-step deposition and 2-step MnO_x coverage, c) higher magnification images of 2-step deposition, d) higher magnification images of H-MnO_x with porosity in nanoflakes.

on the surface of the film after calcination as shown in Figure 4.16a which degrade the performance of the device specially in aqueous based electrolyte. To expound this problem, here I have used a new approach, 2-step anodic ED which not only exhibited better coverage of the CFs and also fills the cracks appeared on the surface of the film as shown in Figure 4.16b. The full coverage of the surface of the CFs is achieved with uniform film of MnO_x nanoflakes of nano scale dimension < 10 nm as expected for this kind of precursor and technique (anodic ED) [136], [139] and Figure 4.16c shows the higher magnification image of the 2-step ED MnO_x nanosheets. To introduce oxygen vacancies and improved kinetics of the MnO_x nanoflakes, the as prepared MnO_x nanoflakes are reduced in hydrogen (H_2 / Ar) environment at 250 ^oC for 3.5 hours (denoted as H-MnO_x). The treatment has introduced further porosity in nanoflakes as shown in the Figure 4.16d, when compared with high magnification FESEM images of simple 2-step MnO_x shown in Figure 4.16c which results in partially crystalline Mn_3O_4 nanosheets.

4.2.4.2 Raman spectroscopy

Structural features of the 2-step ED MnO_x are investigated using Raman spectroscopy. Raman measurements as shown in the Figure 4.17 demonstrate characteristics from both MnO_x in the wavenumber 200 - 800 cm^{-1} range and for CFs in the wavenumber 1200 - 1700 cm^{-1} range. In general, it is well-established that MnO_x in their different crystalline phases show Raman signals associated with the motion of the oxygen atoms within the MnO_6 octahedral units in MnO_x [140]. In particular, this material demonstrated a three Raman bands around 500, 575, 645 cm^{-1} which are in agreement of three major vibrational mode of MnO_2 [166], [167]. At higher wavenumbers, the typical D and G peaks associated with CFs substrate are designated at ~1350 cm^{-1} and ~1580 cm^{-1}, respectively.

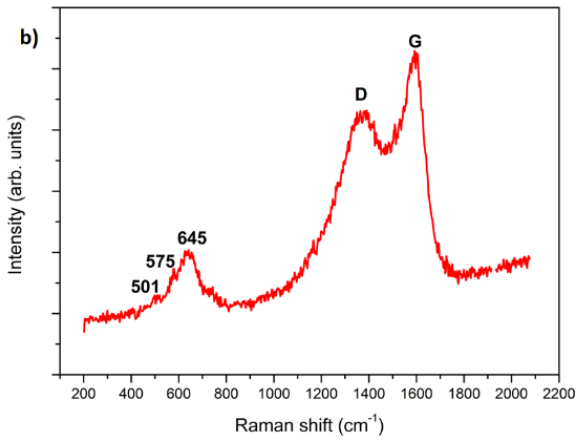

Figure 4.17 Raman spectra of 2-step MnO_x

4.2.4.3 XPS

The XPS measurements are performed to investigate the chemical composition of the MnO_x nanostructures. By the investigation of high-resolution scans of the Mn

2p and Mn 3s areas of the photoelectron spectras of (1-step MnO_2, 2-step MnO_x, H-MnO_x) as shown in Figure 4.18a-b, it is probable to gather information on the different existing MnO_x phases. The Mn 2p region is typically characterized by a complex shape as an effect of multiplet splitting and shake-up attributes [133], [161]. In this case, characteristic attributes of specific MnO_x phases [140] cannot be identified, pointing to the simultaneous existence of different oxidation states of manganese. It is possible to evaluate the average oxidation state (AOS) through the examination of the Mn 3s region: in fact, as reported in the literature, [162] peak separation in binding energy (owed to multiplet splitting) is correlated to the AOS by using the formula,

$$AOS = 8.956 - 1.126\ \Delta E$$

where ΔE is the difference in binding energy between the two main peaks of the Mn 3s region. In this case, the estimated AOS is around 3.1, which cannot be

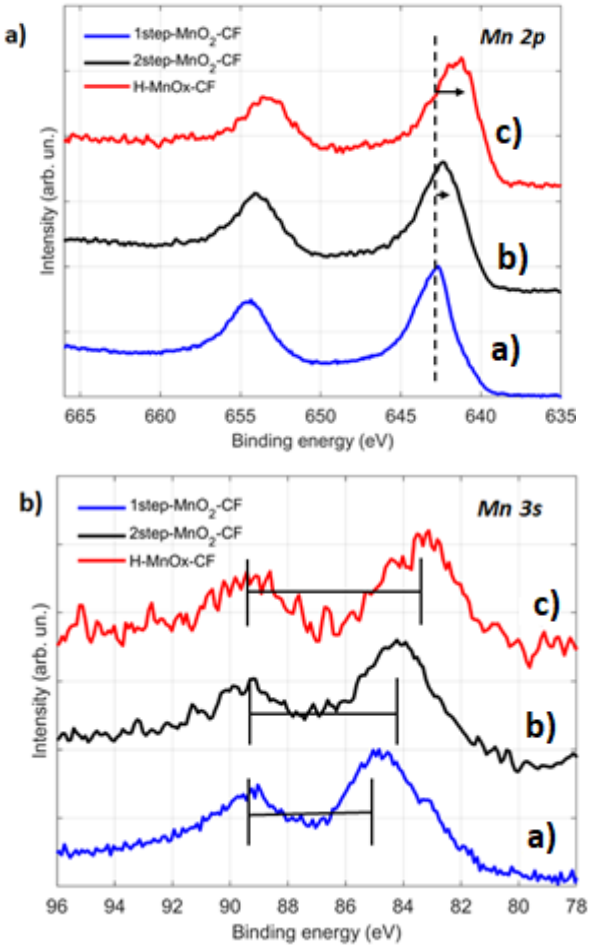

Figure 4.18 Comparison of high-resolution XPS scans of Mn 2p (a) and Mn 3s (b) regions of the photoelectron spectrum of 1-step MnO_2, 2-step MnO_x and H-MnO_x.

attributed to specific stoichiometric MnO_x phases, thus confirming results achieved from the Mn 2p region.

4.2.4.4. Electrochemical characterization

In our previous study [136], single step electrodeposited MnO_2/CF film was subjected to hydrogenation at 250 ^oC for 3.5 hours to further improve electrochemical performance of the electrode by inducing oxygen vacancies and to improved intrinsic kinetic behavior. But extended exposure of high temperature treatment of deposited film, e.g. after deposition calcination at 300 ^oC for one hours and subsequent hydrogenation process at 250^o C in hydrogen environment 2.5^o C/min ramp for 3.5 hours, the structure of the film collapsed and disrupt the continuity of the structure (nanoflakes) as shown in Figure 4.16b. It behaves like resistor during three electrodes electrochemical characterization in 1M Na_2SO_4 aqueous electrolyte at pH=10 (adjusted by adding some drops of NaOH). The electrode resistive behavior after hydrogenation was attributed to surface cracks and dry shrinkage of the electrode because of the removal of the surface adsorbed and structural water elimination [73] which degrade the electrode capacitive performance in the aqueous electrolyte [168].

To overcome this problem of the electrode, a new facile approach was used and divided the optimized two-hour deposition time [136] (at which material shows best performance) into 2-step deposition. In the first step, I performed ED at higher current density (1 mA for 45 min) and subjected this electrode to calcination at 150 ^oC for 1 hour to evaporate the surface adsorbed water. In the second step same process was repeated at lower current density (0.5 mA for 75 min). The bottom line of this strategy is, when I performed calcination after the first step to remove surface adsorbed water, film became a little dry and prone to cracks to appear on the surface of the film during calcination. By performing the second step of deposition at lower current density, I can fill those cracks and not only have full coverage of CFs with interconnected nanoflakes but can get desired morphology (nanoflakes).

CV has been a suitable electrochemical characterization technique for evaluating the capacitive properties of active materials. Two mechanisms are proposed for MnO_2 during charging and discharging, the first one indicates the intercalation of protons (H^+) or alkali metal cations (C^+) such as Li^+, Na^+, K^+ etc. in the bulk of the material upon reduction of MnO_2 to MnOOH followed by deintercalation upon oxidation. As experiments are performed in slight basic environment, so charge storage mechanism is as follows [73],

$$MnO_2 + H^+ + e^- \leftrightarrow MnOOH + OH^- \quad (4.1)$$

Or

$$MnO_2 + C^+ + e^- \leftrightarrow MnOOC^+ + OH^- \quad (4..2)$$

The second mechanism is based on the surface adsorption of electrolyte cations (C^+) on MnO_2 [169].

$$(MnO_2)_{surface} + C^+ + e^- \leftrightarrow (MnO_2{}^- C^+)_{surface} \quad (4.3)$$

Here C^+= cations of alkali metals e.g. Na^+, K^+, Li^+. This mechanism of charge storage of MnO_2 was proposed after the observation of significant difference of the CV's and the specific capacitance of MnO_2 in the presence of various alkali metal cations in the electrolyte [169]. It is noticed in above mentioned equations that both proposed mechanisms of charge storage exhibited the redox reaction between

Table 4. 3 Summary of deposition and masses of deposition

Electrode	Current -Time step1	Current -Time step 2	notation	Mass mg/ cm
1 – step MnO_2	1 mA (120 min)		1-step MnO_2	0 .34
1st step sample1	1 mA (45 min)		1st step- Dep1	0.21
Sample 1	1 mA (45 min)	0.5mA-(75min)	Dep 1	0.29
Sample 2	0.5 mA (75 min)	1mA-(45min)	Dep 2	0.56
sample 3	1 mA (75 min)	0.5mA-(45min)	Dep 3	0.68
H- MnO_x			H-MnO_x	0 .2
$Na_{0.36}MnO_2$			$Na_{0.36}MnO_2$	0.2

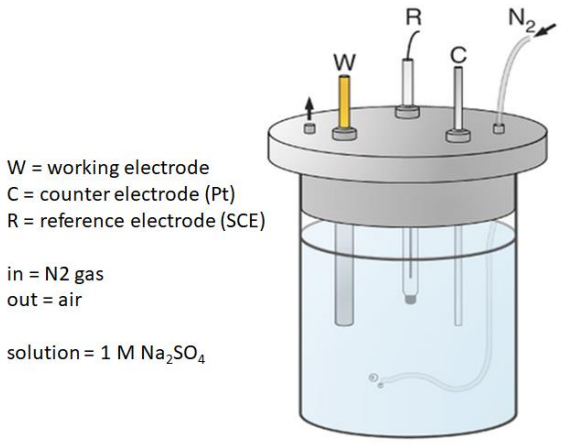

Figure 4.19 Typical three electrodes setup

Mn III and Mn IV of oxidation states of manganese. These mechanisms of charge storage in the MnO_2 electrodes are based on the solid-state diffusion of electrolyte protons in the bulk of the active material similar to RuO_2 [170] but diffusion may not be as fast as of RuO_2 because of low electrical conductivity of MnO_2 [78]. Subsequently, the charge storage might only involve the surface atoms of the MnO_2 crystallites or a very thin layer of active material. Then it might be plausible to

adopt that electrolyte ions would participate in the charge compensation process. On the other hand, the reported [66] specific capacitance for MnO_2 ranges between 150 and 200 F g^{-1} for composite electrode, and it cannot be associated on to the formation of the classical EDL but both EDLC as well as PC. The electrochemical characterizations of individual electrodes are performed to evaluate the electrochemical behavior and stability of nanostructured material, under potential window ranging -0.025 V to 0.75 V in three electrode cell configurations in 1M Na_2SO_4 electrolyte at pH=10, with saturated calomel electrode (SCE) and Platinum (Pt) rod as reference and counter electrode respectively as shown in the Figure 4.19. Figure 4.20a show the cyclic voltammetry comparison of all the individual electrodes, and Figure 4.20b show the comparison of specific capacitances of the all individual electrode materials. The summary of different individual electrode materials studied are shown in Table 4.3 along with loaded mass during depositions. The specific capacitance of the cell was calculated using the equations 2.4 and 2.5 respectively (detail description in chapter 2). From Figure 4.20a-b, it is clear that deposition 1 (notation as described in Table 4.3) is the best performing electrode and exhibited outstanding electrochemical performance with specific capacitance of 267 F g^{-1} at scan rate 5 mV s^{-1} as compared to other electrodes, 94 F g^{-1} for 1-step 2-hours ED MnO_2, and 125 F g^{-1} for 1st step of deposition 1 respectively. It is also clear, the 1st step of deposition 1 has less specific capacitance and second step of deposition has greater impact on specific capacitance value and morphology. It is also observed that electrochemical performance of the pristine CFs (which is not shown here) is very low and have negligible contribution in this electrochemical performance of the electrode and all the capacitive performance

Table 4. 4 Specific capacitance and efficiency of the electrode

Scan rate (mVs^{-1})	1 step MnO_2 (F/g)	1st step Dep (F/g)	Dep 1 (F/g)	Dep 2 (F/g)	Dep3 (F/g)
200	17	41	60	12	9
100	26	55	93	20	15
50	39	70	132	31	24
30	50	83	165	40	32
20	60	92	191	47	38
10	77	107	231	59	49
5	94	126	266	72	59

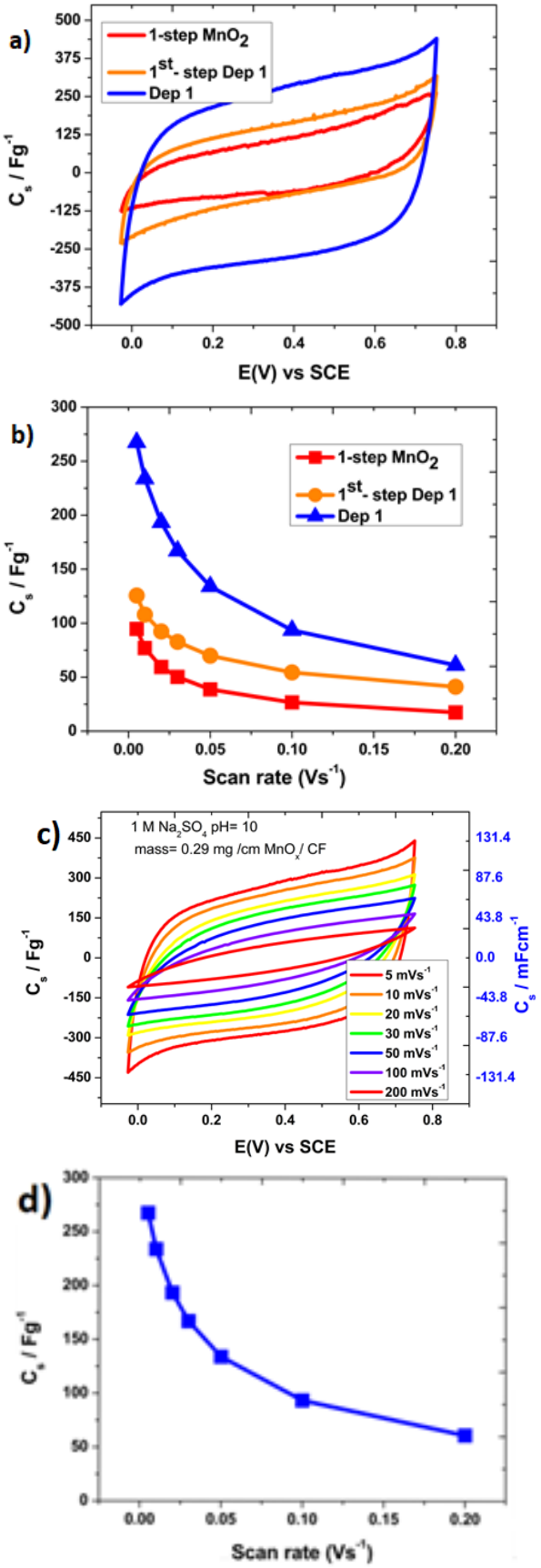

Figure 4.20 a-b) Comparison of CVs & specific capacitance vs scan rates of 2-step MnO_x against 1 step 2 hours deposition and 1st step of MnO_x deposition, c-d) CVs vs potential of 2-step MnO_x at different scan rates and specific capacitance.

strictly attributed to the MnO_x. This value of specific capacitance for 2-step MnO_x /CF is higher than anodically deposited MnO_2 rod like structure on Au sputtered Si substrate with 185 F g^{-1} at 5 mA cm^{-2} [79], 210 F g^{-1} at 5 mA cm^{-2} for ED MnO_2/PEDOT [171]. To study the effect of scan rates, CVs are recorded at different scan rates for 2-step MnO_x starting from 5 mV s^{-1} to 200 mV s^{-1}. The rate of cation diffusion into the bulk electroactive electrode material could be controlled by applying different sweep rates during the electrochemical study. The electrodes electrochemical behavior differs from the anticipated ideal pseudocapacitive behavior at the scan rate higher than 5mV s^{-1} owing to some polarization effect [172], [75]. This means complete charge or discharge of the MnO_x electrodes cannot be realized at this time scale. At high sweep rates, the electron reached only to the outer surface-active sites and half of the manganese surface atoms participate in the Faradaic process [173]. One reason can be that high scan rates limit the diffusion of Na^+ ions and/or protons throughout the bulk volume of the active materials (MnO_x electrode) and electrolyte ions probably adsorbed on the surface of the active material. On the contrary at lower scan rate, ions have large length of time to diffuse in the bulk of the material's active sites and authorizing better intercalation of the ions with active sites exhibiting larger capacity to store charge and hence results in higher specific capacitance properties as a supercapacitor electrode material. The Specific capacitances as function of scan rate for manganese oxide deposits synthesized under different deposition conditions are tabulated in Table 4.4.

Figure 4.21a shows the comparison of the columbic efficiency of electrodes at different sweep rates. It is clear from the plot that efficiency constantly deteriorate for the 1-step electrodeposited MnO_2 and 1st step of the deposition1 but for 2-step electrodeposited electrode shows excellent coulombic efficiency at both lower and higher scan rates. The longer-standing stability of both ED composite electrodes is also investigated using same three electrodes setup in 1M Na_2SO_4 solution at pH=10 for 4000 cycles as depicted in the Figure 4.21b and the variation of specific capacitance is evaluated. The 1-step ED electrode shows good cyclic stability up to 500 cycles but after that continuous deterioration was observed in specific capacitance and total 30 % loss of capacitance is reported after 4000 cycles. But if we compare this cyclic stability performance with 2-step MnO_x, it exhibits excellent cyclic stability and only 3% capacitance loss is depicted. The specific capacitance decreases a small fraction for first 1500 cycles then it increases to original initial value and remain stable for 4000 cycles. I have also synthesized electrodes by varying the time of deposition and order of steps to investigate the impact on the performance of the electrode. It is observed that specific capacitance decreases in both case, in time variation as well as changed order of steps as summarized in Table 4.3

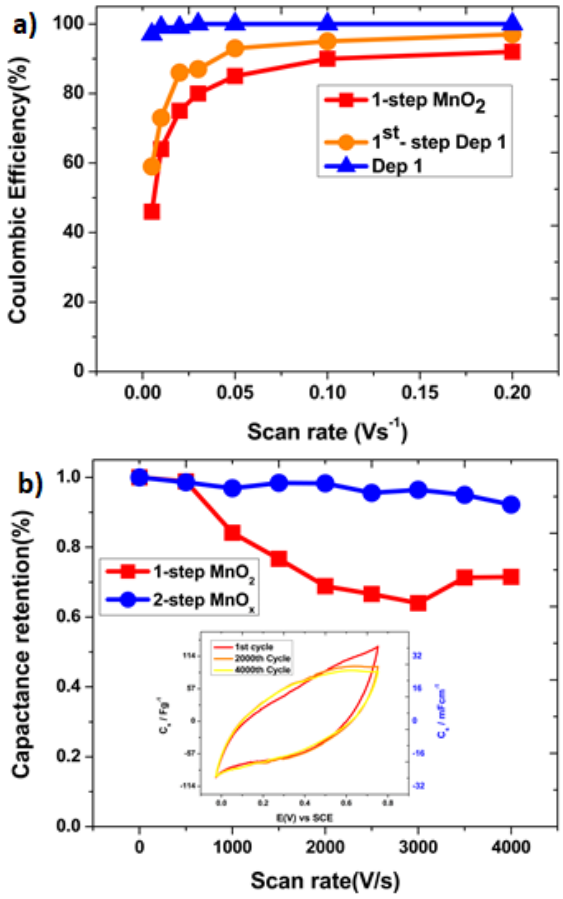

Figure 4.21 a) Comparison of the coulombic efficiencies of electrodes, b) cyclic stability of the 2-step MnO_x electrode.

The improved performance in deposition 1 (2-step ED of MnO_x) as compared to other electrodes (1-step deposition, deposition 2, deposition 3) can be attributed to many reasons, i) more surface coverage as compared to the 1-step MnO_2 and 1^{st} step of deposition 1, so it has more surface area and more active sites are available for charge storage, ii) more uniform and interconnected deposition of MnO_x is obtained in the second step deposition performed at lower current density. In this case first layer of deposited MnO_x particles serve as seed for the growth of thin sheet of MnO_x in the second step [79],[174]. These sheets of MnO_x under galvanostatic control may grow preferentially on energetically favorable sites results in very porous structure exhibiting relatively large specific surface area which encourage effective contact at active material/electrolyte interface offering more active site for electrochemical reactions. It is observed that material with porous structure and interconnected nanoparticles (nanosheets) offer additional accessible active sites for electrolyte ions while maintaining adequate conductivity for electron transfer. This will help to store more charges and results in improved capacitance and high cycling rate. Moreover, nanosheets can provide miniscule diffusion path lengths to both electrolyte ions and electrons and also enough porosity for electrolyte diffusion giving rise to high charge/discharge rates [79]. iii) As the second deposition was performed in the same solution bath, so lower

concentration of precursor in the bath along with low current density promote discrete oxide clusters favors growth of porous structures [172], [174]. iv) Electrodeposition at higher current density (as in 2nd-step in deposition 2) leads to formation of the aggregate of rod-like structure around nanosheets which results in reduced porosity and hence lower specific capacitance and same is the case with deposition 3. v) It is evident that the thickness of the electrodes also plays a major role in electrochemical performance e.g. 2-step MnO_x have less mass as compares to other electrodes. Hence, it is reported [80], [136], that a longer diffusion length of ionic motion in the 1-Step, deposition 2 and deposition 3 electrodes is necessary from electrolyte to the inner MnO_x. In the range of the applied scan rates, alkali cations have enough time to reach the surface of MnO_x for the absorption/desorption reaction to occur favorably and results in improved electrochemical performance.

4.3 Synthesis of Mn_3O_4

Free standing H-MnO_x nanoflakes were also prepared on CFs by performing hydrogenation treatment as shown in scheme Figure 4.16. MnO_x nanoflakes were first grown on CFs by 2- step ED (detail in experimental section) and then they were subjected to thermal treatment under hydrogen (H_2) environment at 250 ^oC for 3.5 hours. This hydrogenation induced oxygen vacancies on the surface of the film and increased the porosity of the electrode as seen in Figure 4.16 (c-d), which results in partially crystalline Mn_3O_4 phase of manganese which is confirmed by XRD and Raman measurement as shown in Figure 4.22a-b.

The hydrogenation process induces a partial crystallization of the material in the Hausmannite form (weak signal), as clearly evidenced in the XRD pattern reported in Figure 4.22a. As reported previously [136], the manganese oxide film is amorphous after the electrodeposition process, while after the hydrogenation step it is possible to identify peaks from the (101), (112), (103) and (201) planes of the Mn_3O_4 crystallographic structure, superimposed to the typical diffraction pattern of CFs. Raman spectroscopy is less sensitive in the precise identification of the crystallographic behavior of this material, since it is well-established that MnO_2 in their different crystalline forms exhibit Raman signals associated to the motion of the oxygen atoms within the MnO_6 octahedral units in MnO_2 .The spectrum reported in Figure 4.22b exhibits an intense and sharp peak at 657 cm^{-1} that can be ascribed to A_{1g} mode which corresponds to the Mn–O breathing vibration of Mn^{2+} ions in tetrahedral coordination, and two weak features at 371 and 318 cm^{-1}, related with Mn−O bending vibrations. At higher wavenumbers, the typical D and G peaks from CFs are revealed at ∼1350 cm^{-1} and ∼1580 cm^{-1}, respectively.

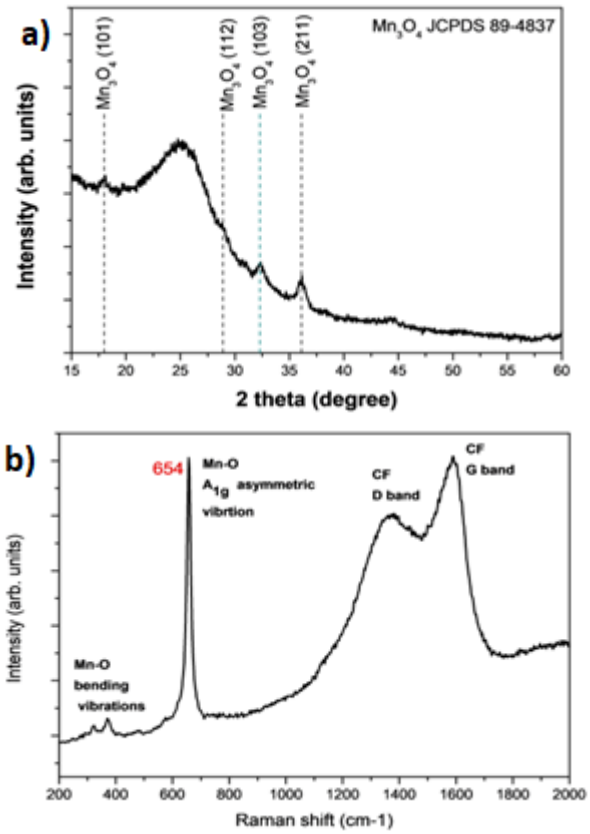

Figure 4.22 XRD and Raman spectra of Mn_3O_4

XPS is also performed to study the surface composition change induced by the thermal treatment. From the Mn 3s spectra of the untreated MnO_x and the H-MnO_x (Fig. 4.18 spectra b and c) substantial change in the multiplet splitting energy induced by a change in the oxidation state. The larger the splitting energy, the lower the Mn valence number. The H-MnO_x shows a larger splitting energy 6 eV as compare to 5.2 eV for MnO_x [143], [162].The thermal treatment under hydrogen flow introduced oxygen vacancies in the MnO_x due to the reduction of Mn (IV) to Mn(III) or Mn(II). The hydrogenated manganese oxide therefore, becomes sub-stochiometric in oxygen (MnO_{2-x}) and it shows a lower average oxidation state 2.3 eV when, compared to the 2-step MnO_x (untreated) 3.1 eV and 1-step of deposited MnO_2 4 eV. These results confirm that hydrogenation treatment has induced oxygen vacancies into MnO_x indicating H-MnO_x film comprises mixed oxide phase.

Electrochemical performance evaluation of the H-MnO_x (Mn_3O_4) was also carried in same three electrodes setup and shown in Figure 4.19. Figure 4.23a shows the CV curve of H-MnO_x at different scan rate and shapes exhibit quasi-rectangular behavior, even as the scan rate increased from 5mV s^{-1} to 200 mV s^{-1} indicating its good capacitive behavior and good rate capability. Figure 4.23b shows the calculated capacitance as a function of scan rates. It is clear from the Figure 4.23b that H-MnO_x show very high specific capacitance of 342 F g^{-1} at 5 mV s^{-1}. In comparison to MnO_x/CF, H-MnO_x exhibits an obvious pseudocapacitive behavior which can be ascribed to the presence of polyvalent Mn ions (Mn^{+3}/Mn^{+2} couple) on H-MnO_x in

line with the literature [162]. This value is higher than H-MnO_x nanorods on conductive carbon fabric (306 F g^{-1}) [162], 261 F g^{-1} Mn_3O_4 [175] and 232 F g^{-1} Mn_3O_4/MnOOH [176]. If we compare the electrochemical performance of the H-MnO_x with 2-step MnO_x, there is a significant improvement in the specific capacitance. The enhanced electrochemical performance is attributed to the oxygen vacancies in H-MnO_x which exhibits excellent electrical conductivity and good capacitive behavior. Moreover, as it is confirmed from the XRD, Raman and XPS that oxygen vacancies-induced phase transformation led to the mixed valent MnO_x [136]. Due to presence of this mix valent manganese oxides, redox reaction on surface of electrodes, surface charge storage as well as intrinsic kinetic properties of the material are viable to be enhanced[177], [178].

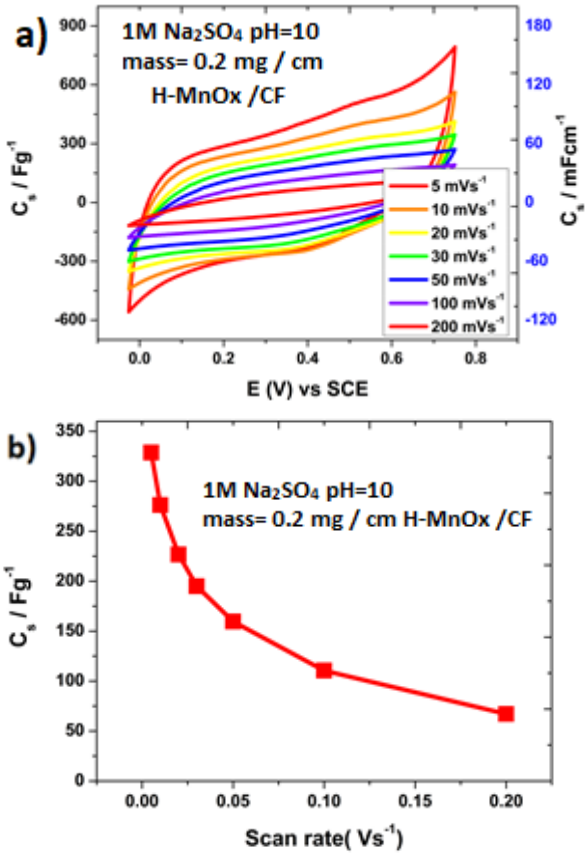

Figure 4.23 a-b) CV comparison at different scan rates and specific capacitance H-MnO_x.

4.3.1 Electrochemical activation of Mn_3O_4

The full capacitive performance of the MnOx cannot be exploited, when electrochemical characterizations are performed in 1M solution of neutral electrolyte, due to low content of cations ratio between Na^+/Mn, which results in limited electrochemical performance of the MnO_x and low specific capacitance [163]. Many groups reported that pre-insertion of high content of cations [such as Na^+ and K^+] in MnO_x nanostructures can effectively improve the electrochemical performance of the MnO_x based electrodes [179]. Pseudocapacitive behavior of the MnO_x is

highly dependent on the number of cations (Na^{+}) inserted which can help in Mn^{+3}/ Mn^{+4} redox couple induction and cause significant increase in the specific capacitance [163], [15].

To counter this problem of low content of cations, here in-situ electrochemical oxidation of Mn_3O_4 spinel structure (detail in experiment section) was performed in the same three electrodes setup in saturated Na_2SO_4 solution, and synthesized

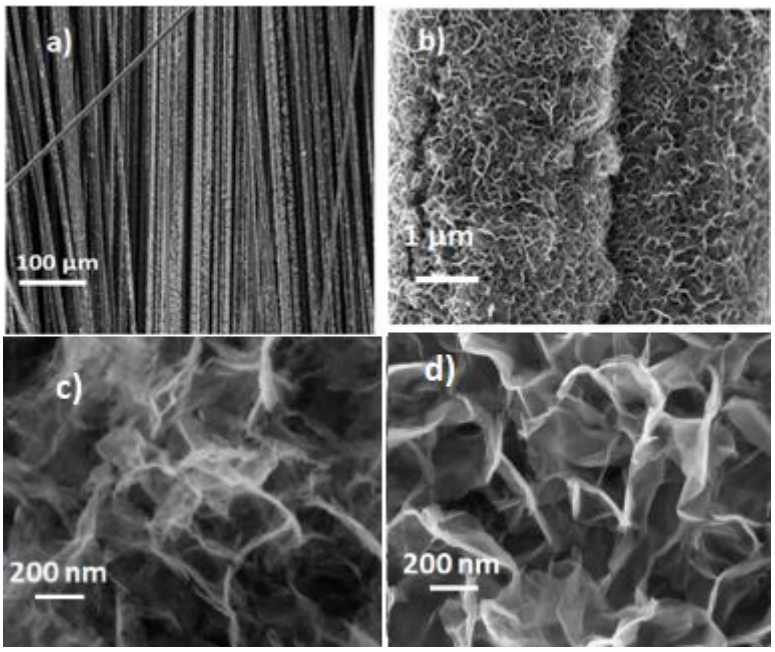

Figure 4.24 a) Show the coverage of the carbon fiber, b) show the interconnected hierarchical structure, c-d) show the comparison of the change in the morphology from Mn_3O_4 to sodium Birnessite

Na-Birnessite hierarchical structure (lamellar nanosheet/nanoflakes) on the CFs substrate as shown in the Figure 4.24a-d. It is clear from the Figure 2.24a that CFs are well covered by the active material. This hierarchical structure offers large specific surface area to electrode material and on other side high content of Na^{+} cations enables the material to exhibit high specific capacitance [163], [179]. The surface morphology undergoes a significant transition before and after in-situ electrochemical oxidation process. As it is clear from the images (Figure 4.24c-d) that after electrochemical oxidation, the final product is not only transformed into novel hierarchical structure composed of lamellar nanosheet /nanoflakes but also induced high porosity. This is also confirmed from the apparent color changes of the H-MnO_x electrode which has changed from brownish to dark black in line with the literature [163].

Raman spectra was obtained to confirm the synthesis of sodium Birnessite type structure as shown in the Figure 4.25. The general distinctiveness of the vibrational features of Birnessite-type MnO_x is their low Raman activity. Three

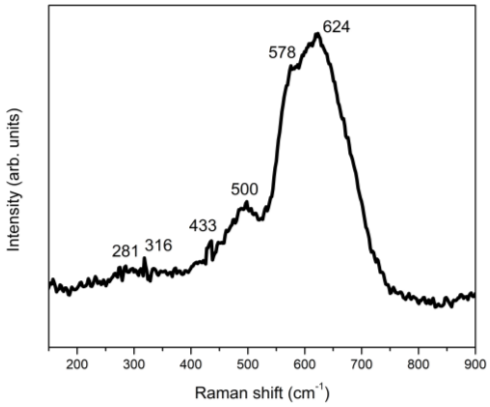

Figure 4.25 Raman spectra of sodium Birnessite

major features can be identified at different wavenumbers range: i.e. 500–510, 575–585 and 625–650 cm^{-1} respectively [163], [180].

The surface electronic state and chemical composition of the material was investigated by XPS as shown in the Figure 4.26. A typical XPS full survey of sodium Birnessite was shown in the Figure 4.26a. It consists of strong representative peaks of Na 1s, Cu 2p3 (impurity from copper tape used during electrodeposition), Mn 2p3, O 1s and C 1s at 1071.3, 934, 641.9, 531.10 and 284.5 eV respectively. From Mn 2p core level spectra, oxidation states of Mn near surface changes from divalvent to tri-valent or tetravalent during electrochemical oxidation [163], [181], [182]. The detailed structure fruition of the Mn_3O_4 spinel structure to layered Birnessite $Na_{0.36}MnO_2$ as shown in Figure 4.27 is like the procedures reported by Kim et al. and Jabeen et al. [163], [181], [183]. During the cyclic voltammetry scans (from -0.2 to 1.15 V), Mn^{+2} in the crystal structure of the Mn_3O_4 dissolved out resulting oxidation of Mn^{+3} in higher oxidation state (Mn^{+4}) [163], [181] with transition from tetrahedral sites to octahedral sites. Meanwhile, crystal water molecules intercalate into space between crystal layers forming layered Birnessite ($Na_{0.36}MnO_2$) type structure while in discharging Na^+ cation will intercalate in the structure and act as a pillar to stabilize structure. Na^+ interaction was confirmed by the XPS results as shown in Figure 4.26c Na 1s core level spectra, the characteristic peak around 1071.3 eV, is attributed to Na^+ cation appear on the surface of the electrode material after 500 cycles. Because of the morphology changes and phase transition, deposition of high surface area Birnessite would occurs during electrochemical oxidation [163], [181]. From the high-resolution analysis, Na/Mn atomic ratio determined to be 0.36 which is in line with the literature [163], [181].

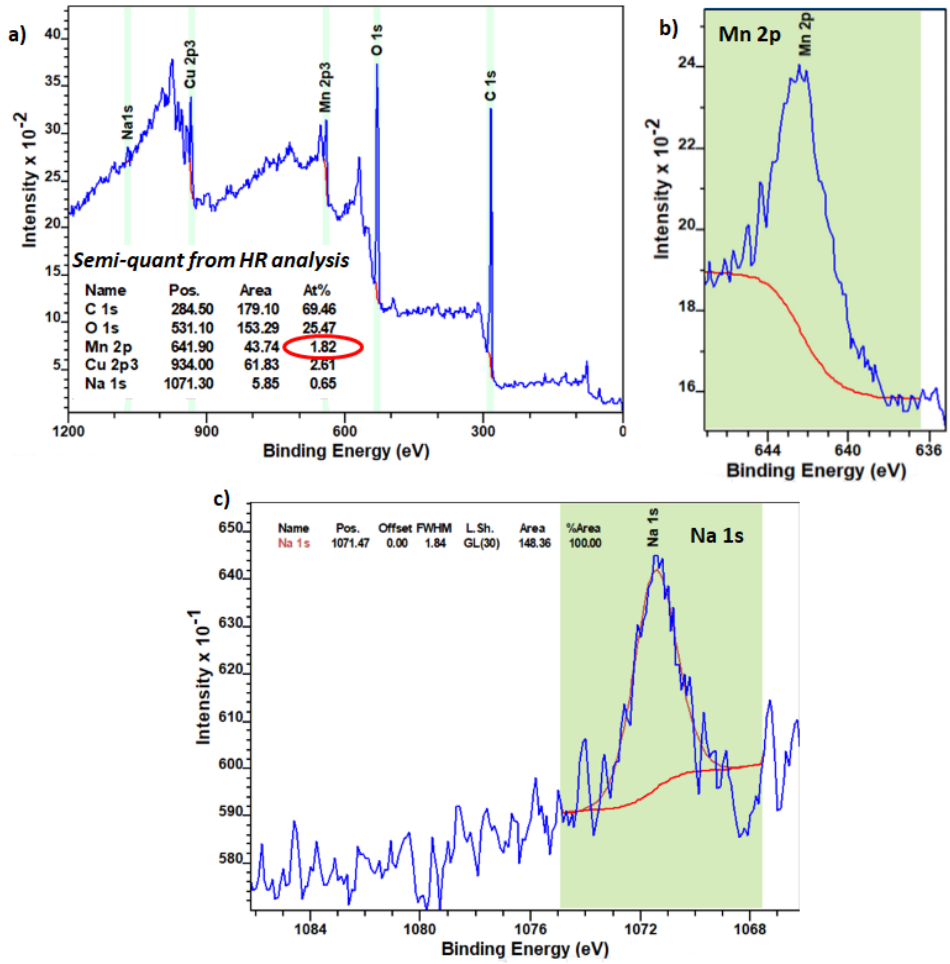

Figure 4.26 a) High Resolution XPS survey spectrum, b) Mn 2p spectra, c) Na 1s spectra

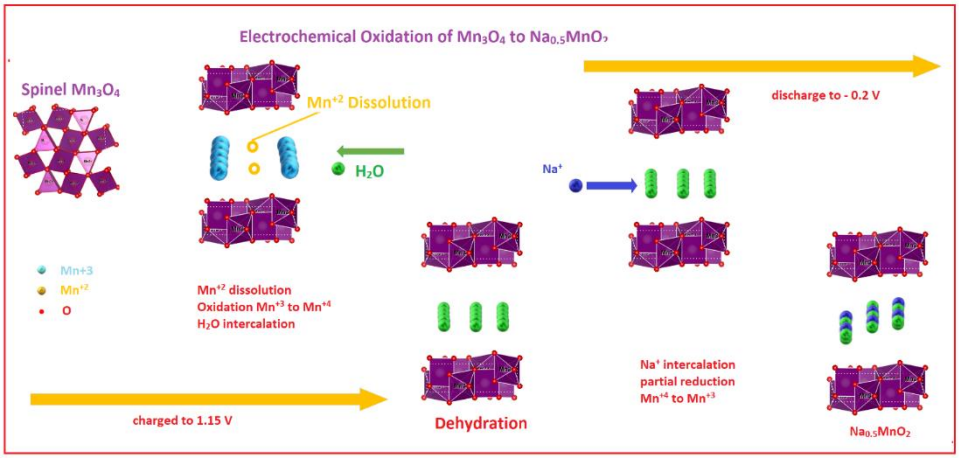

Figure 4.27 Schematic of electrochemical activation of the spinel Mn_3O_4 to Birnessite $Na_{0.36}MnO_2$

It is noteworthy, that preinsertion of the high content of the Na^+ cations in $Na_{0.36}MnO_2$ allowed us to work in extended potential windows -0.2-1.15 V vs SCE by using flexible current collector. CVs were performed at a sweep rate 10 mV s^{-1} between -0.2 and 1.15 V (vs SCE) in saturated solution of the Na_2SO_4 for controlled cycles. For initial cycles anodic peaks around 1 V depicting oxidation of the Mn_3O_4

into higher oxidation state and it is observed during activation process that these anodic peaks and cathodic peaks at 0.7 V on negative cycles are inclined to decreasing trend with increasing number of cycles of activations. These peaks are related to oxidation and reduction of the Mn_3O_4 between Manganese III to IV according to Pourbaix diagram. After performing electrochemical activation for 500 cycles, electrochemical measurements of electrode were performed in 1M solution of Na_2SO_4 at pH=10 vs SCE and Pt rod as reference and counter electrode respectively.

To evaluate the electrochemical performance of sodium Birnessite ($Na_{0.36}MnO_2$), typical cyclic voltammograms were recorded in different potential windows: i.e. -0.2- 0.8 V, -0.2-1 V and -0.2-1.15 V namely (1, 1.2 and 1.35 V respectively) and comparison was plotted for CV's recorded at 5 mV s^{-1} as shown in the Figure 4.28a. It is noted that CV curves show distinct electrochemical performance and current densities in different potential windows. The CV curve of 1 V potential window shows a pair of redox peaks namely anodic peak at 0.51 V and cathodic peak 0.48 V, corresponding to the reversible redox reaction of Mn^{+3}/Mn^{+4} via intercalation and de-intercalation of the Na^+ cations [184]. But as the upper cutoff potential was increase from 0.8 V to 1.0 V, an obvious jump of current emerges for the charging process at 1.0 V, which was in many study assumed as electrolysis with oxygen evolution reaction. But when the upper cutoff potential further increases to 1.15 V, new two pairs of redox peaks at 0.52 V and 0.89 V anodic peaks and 0.48 V and 0.70 V cathodic peaks were observed in the CV curves. These double pair of anodic and cathodic peaks are more prominent, when potential window in raised up to 1.35 V with increased current density associated with Na^+ intercalation and deintercalation. The newly emerged redox couple and increased current density in large potential windows 1.35 V demonstrates that the Mn^{+3}/Mn^{+4} redox is not complete and Na^+ cannot be fully extracted from $Na_{0.36}MnO_2$ when, potential window is below 1 V. The restricted potential windows e.g. 0-0.8 V or 0-1 V adopted for electrochemical measurements (CV and charge and discharge) for MnO_2 based electrodes as reported in literature [187], [188], which results in low specific capacitance and energy density because of small voltage windows for symmetric and asymmetric configurations of SCs. It is noted that voltage window cannot be extended beyond 1.23 V, when working with some metallic substrate such as stainless steel, Ti, and Ni because they cause electrolysis of the electrolyte when potential window is raised beyond 0.8 V [163]. In this study, working potential window can be extended to 1.35 V for sodium Birnessite ($Na_{0.36}MnO_2$) by using carbon fibers and can be a potential cathode material for asymmetric SCs.

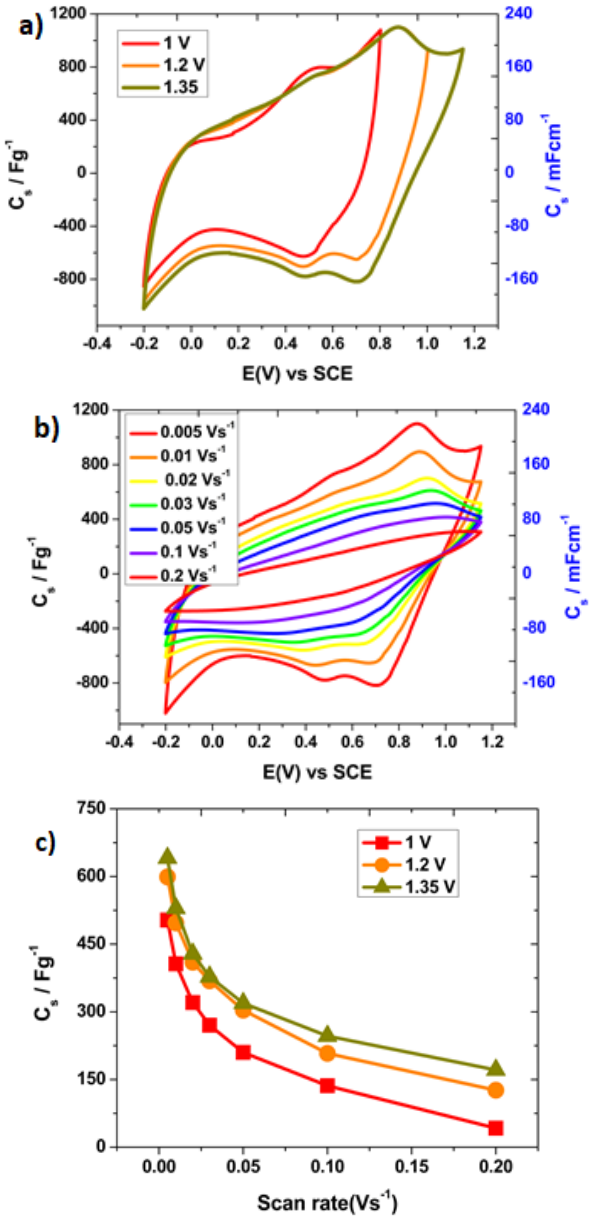

Figure 4.28 a) Comparison of CVs at three different potential windows, b-c) comparison of cyclic voltammetry at different scan rates for 1.35 V potential window.

To understand the charge storage mechanism of the $Na_{0.36}MnO_2$ hierarchical structure and specific capacitance, CVs were recorded at different scan rates. Figure 4.28a show the comparison of cyclic voltammograms of all three potential windows. Figure 4.28b shows the CV curve of hierarchical structure for 1.35 V potential window recorded at different scan rates starting from the 5mV s^{-1} to 200 mV s^{-1}. It is clear from the graph that as the potential windows increases, specific capacitance also increases from 500, 600 and 642 F g^{-1} for 1, 1.2, 1.35 V respectively and maximum capacitance is 642 F g^{-1} at 5 mV s^{-1} against 1.35 V potential window as shown in Figure 4.28c as function of the scan rate. Specific capacitance without pre-insertion is calculated to be 328 at 5mV s^{-1} in the -0.025-0.75 V potential window. If the working potential window extended beyond this range, it gives oxygen /hydrogen evolution reactions as reported in

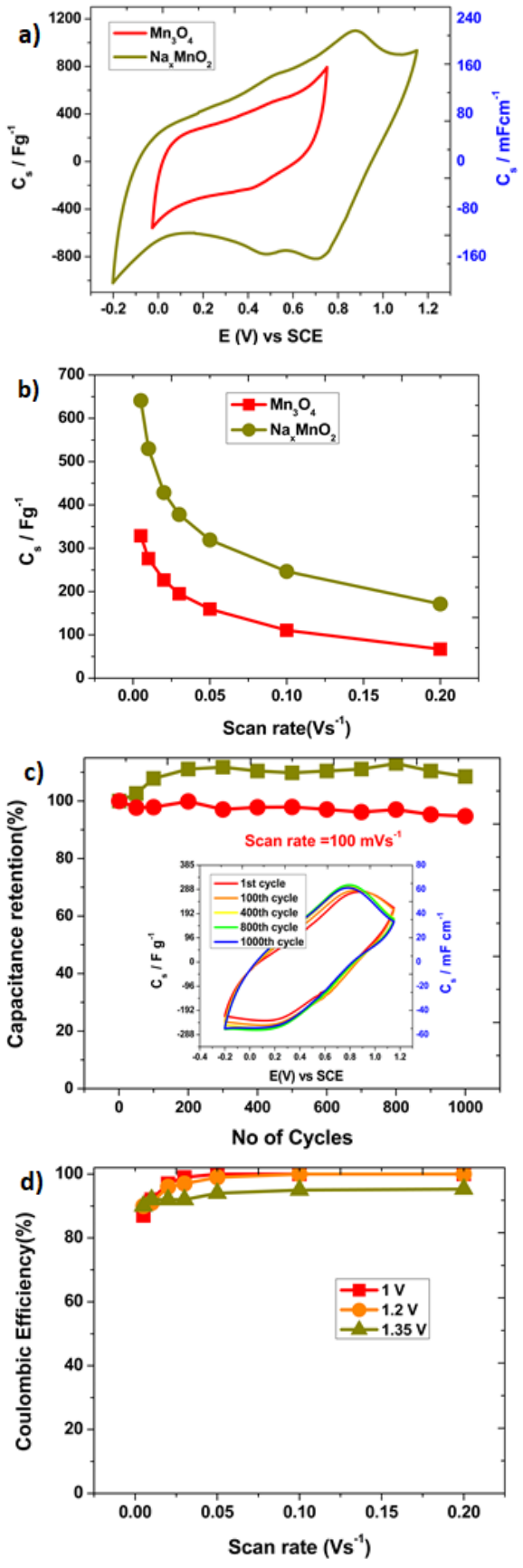

Figure 4.29 a-b) Comparison of CVs and specific capacitance between electroactive $Na_{0.36}MnO_2$ and Mn_3O_4, c) comparison of cyclic stability for 1 V and 1.35 V potential windows (inset CVs at different cycles), d) columbic efficiency at different potential windows.

literature [9,31-32]. It is clear from the Figure 4.23b that although, H-MnO_x show high specific capacitance value of 328 F g^{-1} at 5 mV s^{-1} as compare to the simple 2-step-MnO_x in potential window of -0.025-0.775 V but we cannot go beyond this restricted potential window, due to oxygen/hydrogen evolution reactions and hence results in low specific capacitance. But after pre-insertion, the capacitance of the device increases almost double to pristine Mn_3O_4 spinel structure as shown in Figure 4.29a-b. This specific capacitance of 642 F g^{-1} for 1.35 V potential window is much higher than reported values $Na_{0.5}MnO_2$ 366 F g^{-1} [163], K_xMnO_2 260 F g^{-1} [189]. This indicates that crystalline phase change from Mn_3O_4 to Birnessite proceeds by electrochemical oxidation accompanied by morphological changes and increased specific capacitance. It is reported [163] that Birnessite $Na_{0.36}MnO_2$ are more electroactive because redox couple Mn(III)/Mn(IV) in solids accompanied with reversible alkali ions and proton insertion. Therefore, high capacitance value of the Mn_3O_4 electrode after electrochemical oxidation is due to the formation of Birnessite structure with high surface area. To investigate the cyclic stability of the device over the extended voltage window cyclic performance was evaluated in different potential windows 1 V and maximum 1.35 V as shown in Figure 4.29c. It is clear from the graph, device demonstrate a cyclic stability with retention of over 98% of capacitance for both 1 V and 1.35 V potential windows and above 95% coulombic efficiency at such high scan rate as shown in Figure 4.29d. This shows that increase in the potential window does not deteriorate specific capacitance and coulombic efficiency in extended potential windows and can be potential electrode for large voltage windows SCs. After hydrogenation of as prepared MnO_x characterized as Mn_3O_4, converted to Birnessite $Na_{0.36}MnO_2$ via electrochemically activation. They are termed as composite material comprise of Birnessite structure $Na_{0.36}MnO_2$ and marginal portion of Mn_3O_4. The improved performance of the material is attributed to the synergistic effect of poorly crystallized MnO_2 and Mn_3O_4 in the composite material and this non-stochiometric Birnessite $Na_{0.36}MnO_2$ generating composite material possess excellent electrochemical performance.

4.4. Conclusion

The main conclusions of the work are the following

1. This facile method of 2-step anodic ED allows the desirable large-area synthesis and offer a unique combination of high MnO_x mass loading, binder-free properties, excellent electrical conductivity.
2. The oxygen vacancies induced in 2-step ED MnO_x by hydrogen environment at 250 ^oC have intrinsically improved conductivity and electrochemical performance of the material. H-MnO_x nanoflakes obtained from hydrogenation exhibit remarkable enhanced electrochemical performance and excellent rate capability compare to bare MnO_x in 1M Na_2SO_4 at pH=10. H-MnO_x with vacant oxygen sites and

highly porous nanoflakes enables remarkably increased conductivity, reversible and fast charge transfer kinetics and excellent cyclic stability in aqueous electrolyte.

3. In-situ electrochemical activation of the Mn_3O_4 spinel structure help us to obtain high specific surface area and improved conductivity which results in higher specific capacitance with excellent cyclic stability.

4. The ability to intrinsic electrochemical performance, open macro-/meso-porous nanostructure, high-availability of active sites for the electrolyte, use of low-cost raw materials open new opportunities for other semiconductor material for different application.

Chapter 5 Design and development of high energy asymmetric fiber-shaped SCs

"Experimenter are the shock troops of Science".
— Max Planck.

5.1. Introduction

To bridge the gap between batteries and conventional capacitors, SCs have been employed in a variety of applications ranging from portable electronic devices, hybrid electrical vehicles and large industrial scale power and energy management. Therefore, the challenge of the current SCs is to increase the energy density without sacrificing its power density and cyclic life. The specific energy density (E) and specific power density (P) of the SCs is computed according to equations 2.7 (detail in chapter 2),

$$E = \frac{1}{2} C_s V^2$$

This means based on above equations, a 2- fold increase in voltage window could result in a 4-fold increase in specific energy of the SC device for the same value of specific capacitance. Therefore, the specific energy of the device can be enhanced either by increasing the voltage window or by increasing the specific capacitance of the SCs. There are two possibilities to enhance the cell voltage: i) using polymer electrolyte because they provide a wider voltage window with better electrochemical stability than aqueous electrolytes. ii) asymmetric supercapacitors (ASCs) configuration because each electrode material has its own working voltage[190]. One effective way to improve the energy density is to adopt the asymmetric configuration because during the charge/discharge processes, ASCs can exploit different voltage windows of the two electrodes to maximize the operating

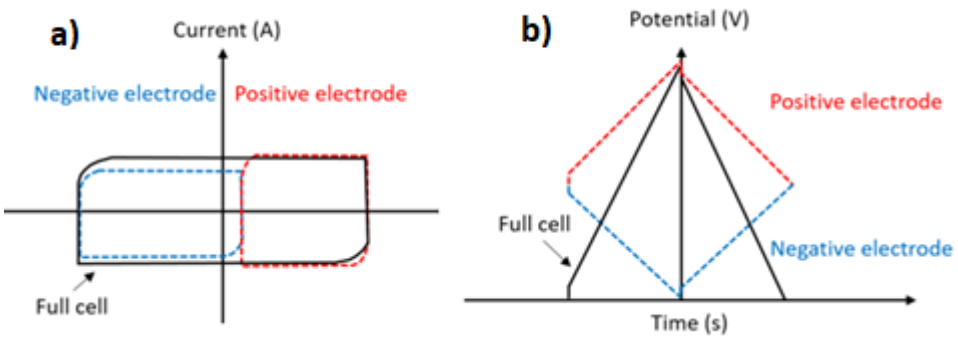

Figure 5. 1 Capacitive asymmetric supercapacitor

potential of the device as shown in the Figure 5.1a-b. For example, while the potential of a liquid-based symmetric device is restricted to ∼1.23 V, the operating potential of an ASCs can be extended beyond 2.0 V. ASCs is an alternative approach for improved energy density because they can work in wider voltage windows as compared to symmetric SCs [191]. There has been increasing interest in incorporating carbon-based material with TMOs to design nanomaterials for SCs (called PCs) because their fast- redox reactions occurring at the surface and bulk of the electrode materials results in higher energy density. Therefore, a suitably designed ASCs offers the prospect of increasing the energy density for applications where high energy needs to be stored and delivered with high power.

5.1 rGO aerogel /Fe_2O_3 // 2-step MnO_x based asymmetric SCs

5.1.1 Introduction

In this study, a composite of Fe_2O_3 dispersed on rGO aerogel was synthesized by a hydrothermal technique with polyols as green surfactant for negative electrode of an ASC. Graphene based materials have been widely studied in electrochemistry as extremely conducting mediator to fabricate composites. The aerogel configuration offers a 3D porous structure with high specific surface area, where stack of few-atomic layers of graphene constitute the highly conductive path and promise the fast diffusion of the ions of electrolyte and a rapid electron transport. Moreover, conductive CFs have been chosen as apposite current collector in view of the production of wearable devices. Undoubtedly, the resultant composite rGO/Fe_2O_3 aerogel displays outstanding pseudocapacitive performance in terms of high specific capacitance. 2-step electrodeposited MnO_x nanostructured onto CFs was opted as suitable positive electrode for the fabrication of fiber-shaped SC. The assembled flexible device demonstrated high rate capability, remarkable bending and cyclic stability in a hydrogel electrolyte.

5.1.2. Experimental

In this section, detail about synthesis of active materials and fabrication of the electrode is presented. This section also provides information about reagents used.

5.1.2.1. Reagent

Iron Nitrate $Fe(NO_3)_3.6H_2O$ (Sigma Aldrich), Olive leaf Algerian region, Distilled water, Graphene oxide (GO) powder (Single Layer GO, 0.7-1.2 nm, Cheap Tubes Inc.), L-Ascorbic Acid (L-AA, Sigma Aldrich), carbon fibers (Panex® 35, ZOLTEK), Manganese acetate ($Mn(CH_3COO)_2$), Na_2SO_4

5.1.2.2. Synthesis of Fe_2O_3 and rGO/Fe_2O_3

In a typical synthesis of hematite, solutions of Fe_2O_3 are obtained by a green technique using: iron nitrate $Fe(NO_3)_3.6H_2O$ as a precursor, an olive leaves extract as a dual functioning surfactant as well as reducer with distilled water as a solvent. Primarily, fresh olive leaves obtained from Algerian region, are washed and then dried completely. Afterward, an infusion of these olive leaves is prepared by mixing 10 g to 1 L of Milli-Q water. The infusion is thermally treated at 100 °C and then filtered to eliminate the leaf particles. Thereafter, 0.6M of $Fe(NO_3)_3$, was mixed

with 30 ml of this infusion while vigorously stirring which results in an orange color solution. Then orange color solution is shifted into a beaker and put in a reflux system at 70 °C for 3 h. The obtained solution is dehydrated under 100 °C and the final powder obtained is washed with Milli-Q water and ethanol for numerous times and dried at room temperature. Finally, the powder is shifted into an oven for calcinations at 400°C for 1 hour.

Graphene oxide (GO) powder is dispersed in 16 mL of distilled water and L-Ascorbic Acid (L-AA), L-AA is added to the slurry as reducing agent of GO according to a 2 mg/mL final concentration (w/v). After 5 hours, the dispersed solution is sonicated for 30 minutes and 1 mL of the Fe_2O_3 solution is added to the pristine dispersion. The final slurry is then shifted into a Teflon reactor and sealed into a stainless-steel autoclave and placed in a muffle oven for the rGO/Fe_2O_3 hydrogel synthesis happened under hydrothermal conditions, for 12 hours at 180 °C After ambient cooling to room temperature, the rGO/Fe_2O_3 hydrogel is frozen at -196 °C in liquid nitrogen and then dried, overnight, under vacuum pressure (3 x 10^{-3} mbar) at -55 °C in a LIO – 5P DIGITAL lyophilized (5Pascal-Italy).

5.1.2.3 MnO_x electrodeposition

The synthesis of MnO_x nanoflakes onto CFs current collector is obtained by a 2-step galvanostatic anodic ED. The deposition bath comprises 0.1 M $Mn(CH_3COO)_2$ and 0.1 M Na_2SO_4 as supporting electrolyte. The deposition was performed under a current density of 0.27 mA cm^{-2} for 45 minutes and 0.135 mA cm^{-2} for 75 minutes. In between the deposition steps, the electrode is washed and dried at 150°C for 1 hour and after the second step, the electrode is washed with distilled water so that free metal ions can be detached and annealed at 300°C for 1 hour. The mass of the deposited MnO_x on the CFs is assessed by weighting the CFs before and after deposition using a microbalance (Sartorius CP225D). Electrochemical deposition is performed using three electrode cells in which Ag/AgCl and platinum mesh are used as reference and counter electrodes respectively.

5.1.3. Characterization

The physical characterization performed (FESEM, EDX, XRD, Raman and XPS) are described in detail in chapter 3 and chapter 4 experimental sections. The electrochemical characterization of as-synthetized hematite nanoparticles, rGO/Fe_2O_3 composite and ED of MnO_x electrodes is performed in a three electrodes cell in deaerated 2M KOH with Ag/AgCl and platinum bar as reference and counter electrode respectively. The slurry of Fe_2O_3 nanoparticles is prepared by mixing Nafion 5% and water (1 mg: 3 ul: 140 ul) to obtain a well dispersed ink which is drop casted onto mirror-like glassy carbon (GC) electrodes (5 ul). The weight proportion of electrode material with respect to binder and solvent is revised for rGO/Fe_2O_3 to

sustain same loading of Fe_2O_3 onto the GC electrodes. All the GC electrodes are then loaded with 0.5 mg cm^{-2} of the prepared ink.

5.1.3.2. Device fabrication and characterization

The asymmetric hybrid device is assembled by depositing rGO/Fe_2O_3 onto CFs used as negative and ED MnO_x on CFs used as positive electrode. The mass per length proportion of negative and positive electrodes active materials is modified so that the charge stored on the two electrodes should be equal which are 2 and 1.6 mgcm^{-2} respectively. The electrochemical measuremenst of asymmetric device is first performed in 2M KOH and then a device fabricated by using a hydrogel (PVA in 2M KOH) used as electrolyte as well as separator to evade short-circuits. All the measurements were performed on M101 Metrohm potentiostat/Galvanostate with Nova 2.1 software, a part of the cyclic life stability of the asymmetric hydrogel device that is performed at 1 A g^{-1} on Arbin instrument.

5.1.4. Results and discussion

FESEM measurements of the synthesized rGO/Fe_2O_3 samples, after freeze drying is reported in Figure 5.2a. The existence of hematite solution does not affect the development of the rGO aerogel, which exhibit the characteristic 3D porous structure consists of interconnected wrinkled rGO flakes [192]. The hematite nanostructures decorate the rGO aerogel evenly, as depicted in Figure 5.2b, where

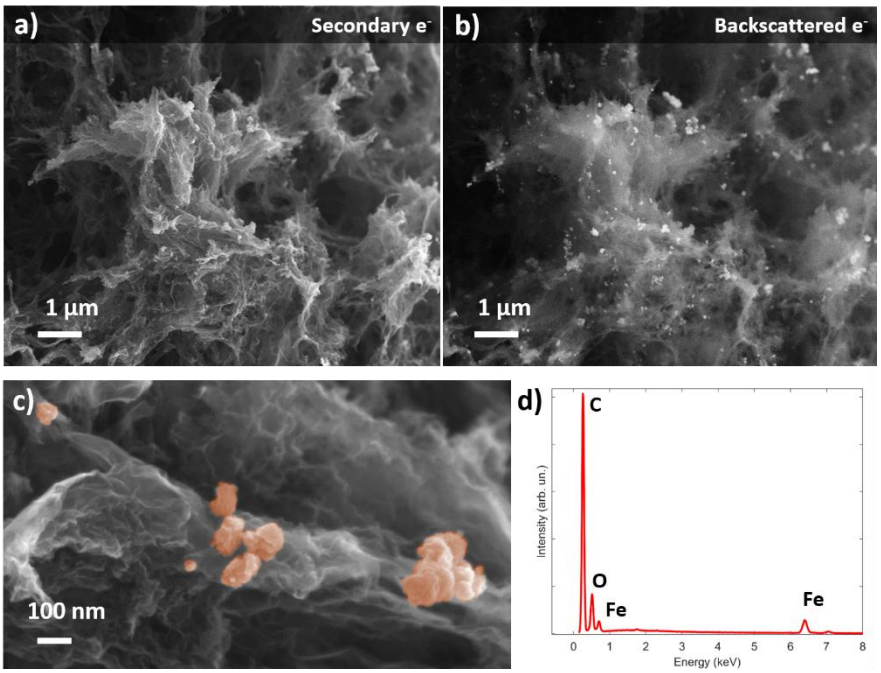

Figure 5.2 Low-magnification FESEM secondary electron image (a) and pseudo-back scattered electron image (b) of the rGO/Fe_2O_3 sample, accompanied by a high-magnification view (c). Representative EDX spectrum (d) acquired on a large area is presented.

the iron-containing nanoparticles are identified as higher intensity features in the image, owing to pseudo-back scattered electron imaging, with contributions to contrast arising from average atomic number differences. Depending on high-resolution images such as Figure 5.2c, the hematite nanoparticles having mutable diameters roughly in the range of 100–200 nm, with nanostructured exterior surface and asymmetrical shape. EDX analysis is also performed as shown in figure 5.2d to confirm the chemical composition of the hematite sample: the EDX spectra show C, O and Fe contributions.

Crystallographic classification of the synthesized material is done by means of X-ray diffraction as depicted in Figure 5.3a. The rGO aerogel structure exhibits a disturbed behavior and the characteristic peak at ~23° (2ϑ) is difficult to distinguished from the background. On these attribute, representative peaks from Fe_2O_3 in the hematite phase are superimposed. Fe_2O_3 phase has a hexagonal symmetry (R3c space group), and the resulting resonances from (012), (104), (110), (113), (024), (116), (214) and (300) planes are visibly evidenced. Raman spectra was also achieved as shown in Figure 5.3b which confirms the structural results, display the contribution from both the supporting rGO and the hematite nanostructures. The rGO support exhibit the characteristic attributes of disordered carbon, with the presence of the D band at ~1350 cm^{-1}, related with the creation of defects, vacancies and bent sp^2 bonds and G band at ~1580 cm^{-1}, instigated from a first- order inelastic scattering method including the degenerate iTO and iLO phonons at the G point (E_{2g} mode). In the Raman modes, hematite are clearly visible at lower wavenumbers, since the material has two A_{1g} and five E_{1g} modes (247 cm^{-1}, 293 cm^{-1} and 299 cm^{-1}, overlapping in the room temperature spectrum, 412 cm^{-1} and 613 cm^{-1}) [192] modes (225 cm^{-1} and 498 cm^{-1}).

The XPS analysis is performed to study the chemical composition of the surface, in order to (i) check that the rGO reduction during the hydrothermal treatment is not affected by the hematite dispersion and (ii) for the identification of the iron-containing phases and validation against the results achieved from the structural classification. Figure 5.3c shows the deconvolution of the C 1s region of the photoelectron spectrum into components with different chemical environments, exhibiting characteristic attributes of reduced GO. Precisely, contributions associated to oxygen-containing groups are significantly reduced after the hydrothermal treatment as shown in the Figure 5.4c which display the comparison between the starting GO powder and the reduced GO which is achieved after the synthesis of the hybrid rGO/Fe_2O_3 electrode material. After the hydrothermal process, contributions at binding energies higher than 285 eV significantly decreased, authorizing the successful reduction of the initial GO flakes.

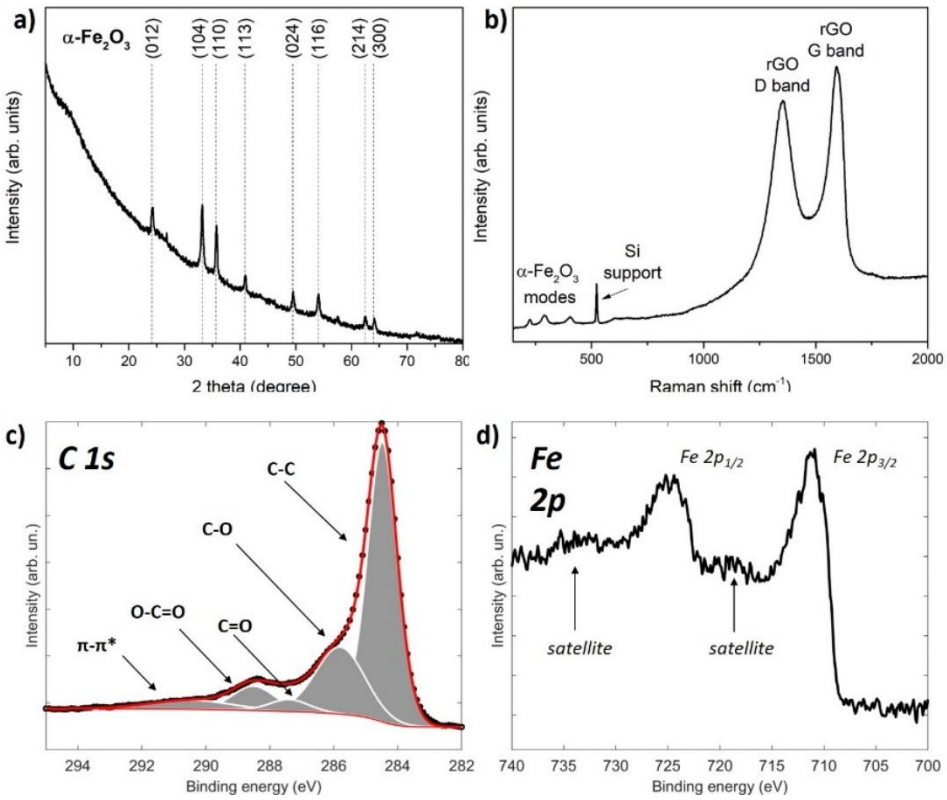

Figure 5. 3 (a) X-ray diffraction pattern of rGO/Fe_2O_3 hybrid material (reference card for α-Fe_2O_3: JCPDS 89-2810); (b) Raman characterization of rGO/Fe_2O_3 hybrid material. High-resolution XPS scans of the C 1s (c) and Fe 2p (d) regions of the photoelectron spectrum for sample rGO/Fe_2O_3.

Moreover, the π-π* satellite at the higher binding energy side is characteristic of graphitic materials, since this contribution is owed to interbond shifts in sp^2-hybridized structures [193], [194]. Concerning the recognition of iron-containing phases, the Fe 2p region (Figure 5.3d) gives a lot of information but the investigation is not trivial. In fact, the Fe 2p region shows multiplet splitting, leading to complex shape of the main peaks (Fe $2p_{3/2}$, Fe $2p_{1/2}$). Moreover, satellite peaks owed to transformation processes are present [195]. In practice, it is possible to classify the iron-containing phases by the investigation of the following attributes: generally, shape of the Fe 2p region, binding energies of the main peaks, presence and binding energies of the satellites. In this case, the binding energies (BE) of the main doublet (BE (Fe 2p3/2) ≈ 711.3 eV, BE (Fe 2p1/2) ≈724.8 eV) and the presence of two satellite peaks positioned at nearly 719 eV and 733 eV, are well-matched with the Fe_2O_3 phase, in agreement with XRD and Raman results and with the literature [191].

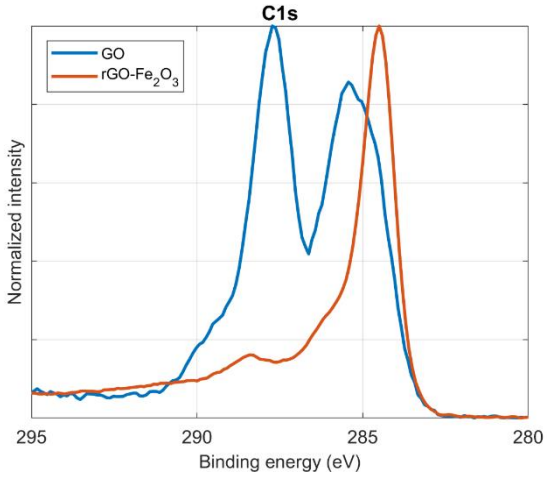

Figure 5.4 High-resolution scans of the C 1s region of GO and rGO-Fe_2O_3 samples.

5.1.4.1. Electrochemical characterization

The electrochemical measurements of the as-synthesized materials are performed by cyclic voltammetry and galvanostatic charge-discharge in a three electrodes cell as shown in the Figure 5.5a. The as-prepared Fe_2O_3 and rGO/Fe_2O_3 composite were drop-casted onto GC electrodes to have a comparison of the same quantity of Fe_2O_3 nanoparticles configured in different structures. Figure 5.5b shows the cyclic voltammogram of Fe_2O_3 and rGO/Fe_2O_3 at 2 mVs^{-1} together to appreciate the larger currents obtained by the composite material, hence higher specific capacitance. The linearity of CV curve of Fe_2O_3 nanoparticles demonstrate a highly resistive electrode material that cannot be used straight as active electrode material for electrochemical storage purposes. On the contrary, CV curve of nanocomposite shows no resistive behavior and demonstrated well-defined cathodic and anodic redox peaks at -1.072 V during cathodic scan and at -0.762 V in the anodic scan respectively, this also true for Fe_2O_3 sample for redox peaks at the same potentials. These results show that the charge attributes are governed by Faradaic redox reactions which correspond to the conversion of Fe^{+2} to Fe^{+3} [1], [196]–[198].

According to the above electrochemical measurements and the alkalinity of the electrolyte involved, the possible mechanisms of charge storage and the resulting reactions are as follows:

1) Activation reaction:

$$Fe_2O_3 + H_2O \rightarrow 2\,FeOOH \qquad 5.1$$

2) Discharging reaction:

$$FeOOH + H_2O + e^- \rightarrow Fe(OH)_2 + OH^- \qquad 5.2$$

3) Charging reaction:

$$Fe(OH)_2 + OH^- \rightarrow FeOOH + H_2O + e^- \quad 5.3$$

$$3\,Fe(OH)_2 + 2\,OH^- \rightarrow Fe_3O_4 + 4\,H_2O + 2\,e^- \quad 5.4$$

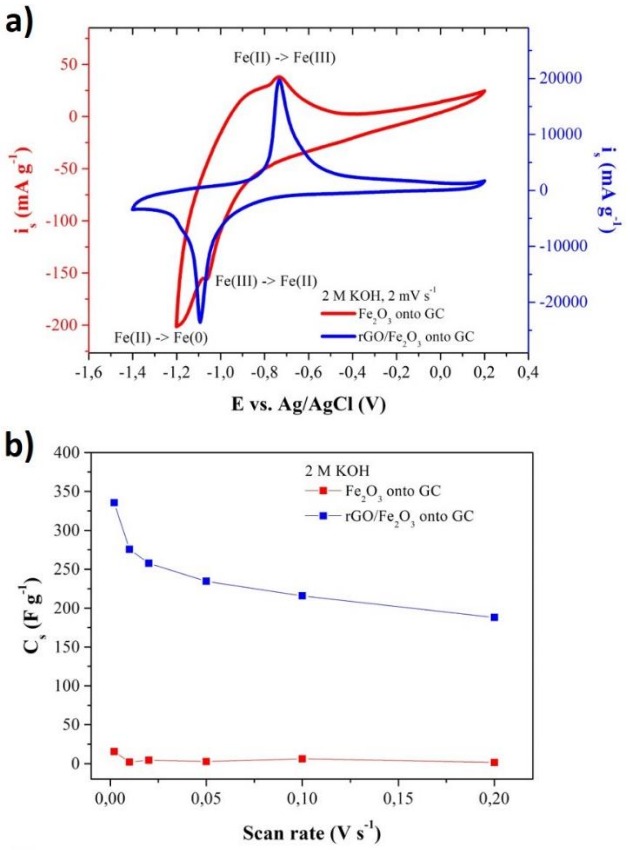

Figure 5.5 a) Comparison of CV and specific capacitance, b) between Fe_2O_3 and rGO/Fe_2O_3-30 OLE.

In the charging process, two possible reactions can take place or compete. On the anodic sweep, at potentials lower than -1.072 V, both the voltammograms exhibit asymmetry of the reduction peak. This current behavior can be subjected to many reasons: (i) a second current peak, (ii) a change in the resistance behavior of the active material due to the possible intercalation of cations (K^+) in the crystal structure, (iii) varying rate of redox reactions, after the maximum current potential or combination of thereof. At low scan rate such as 2 mV s^{-1}, the first sweep demonstrated an extra peak around potential of -1.2 V that gradually disappears after five sweeps. The proposed reaction is a complete reduction with two electrons from Fe^{+2} to Fe [196]–[199] but as I move to more negative potentials, HER happens. Instead, the decoration of the rGO with Fe_2O_3 nanoparticles immensely changes the performance of pristine rGO (renowned to be a EDLC material) and

the metal oxide nanoparticles make a major contribution to the total capacitance of the electrode. It is clear from Figure 5.5b, the specific capacitance of the rGO/Fe_2O_3 composite is more than one order of magnitude higher (330 F g^{-1}) than pristine Fe_2O_3 (15 F g^{-1}) at 2 mVs^{-1}. But, as the scan rate increases, the specific capacitance decreases representing an electrochemical system in whichthe intercalation of electrolyte ions plays a significant role. From the CV, the hematite nanoparticles activated in alkaline electrolyte demonstrated wide peaks signifying a primarily pseudocapacitive behavior. It is interesting to separate the total charge stored from the segment owed to capacitive controlled and diffusion-controlled phenomena.

5.1.4.2 Charge storage mechanism

The voltammograms recorded at different sweep rates have been examined to abstract the current which is linear dependent on scan rate ν and in the second process current is proportional to the square root of the scan rate, $\nu^{1/2}$) according to [198]–[200]:

$$i(V) = k_a \nu + k_b \nu^{1/2} \qquad 6.5$$

Figures 5.6a-b demonstrate the ratio of capacitive and diffusion-controlled charges at different scan rates. This graph shows that, the maximum current at high sweep rates is capacitive controlled and as we move to lower sweep rates current gradually becomes predominantly diffusion-controlled**.** By equating the charge stored on the Fe_2O_3 and rGO/Fe_2O_3 composite electrodes materials, at higher scan rate like 200 mV s^{-1} almost 69 % and 13 % of the total currents are due to diffusion-controlled phenomena and these proportion increase to 94 % and 60% when the scan is lowered to 2 mV s^{-1}, as reported in Table 5.1. In Figure 5.6c-d, instead, the reconstructed CV voltammograms of the capacitive controlled current at 10 mV s^{-1} are stated together with the percentage of the capacitive-controlled to total stored charge. These projected CV voltammograms are equated with the ones experimentally achieved on Fe_2O_3 (c) and rGO/Fe_2O_3 (d) at the same sweep rate. In the rGO/Fe_2O_3 composite case, a higher capacitive controlled charge value is ascribed to the peaks agreeing to the Fe^{+2} to Fe^{+3} reaction. I am confident that the rGO framework enhances the utilization of the active material offering a higher electrode/electrolyte interface, reducing the diffusion path length of adsorption/desorption of ions and improves the kinetic of electron transfer. The improved capacitive performance of the rGO/Fe_2O_3 nanocomposites is owed to the synergetic effect of the higher conductivity of rGO and the mesoporous structure of hematite nanoparticles. The high specific surface area of rGO nanosheets helps the anchoring of hematite nanoparticles and at the same time the rGO nanosheets are analogous to a conductive additive by significantly improving the electrical conductivity of the rGO/Fe_2O_3 nanocomposites.

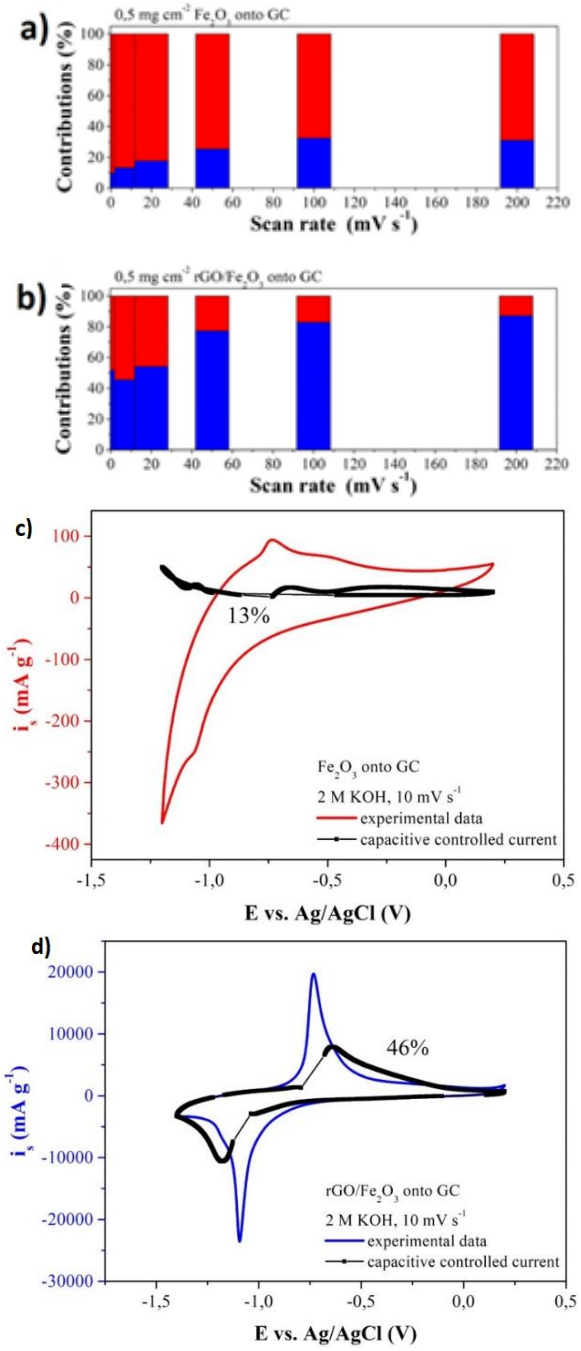

Figure 5.6 Estimation of the charge stored by diffusion-controlled phenomena (red) and capacitive controlled phenomena (blue) at different scan rates on Fe_2O_3 (e) and rGO/Fe_2O_3 (f). Reconstructed voltammograms of the capacitive controlled current (black line+dots) contribution to the total current in the voltammetry of Fe_2O_3 (c) and rGO/Fe_2O_3 (d).

The well-dispersed Fe_2O_3 nanoparticles avert the agglomeration and the reloading of rGO nanosheets creating larger specific surface areas which is available for the high energy storage. The capacitance results confirm that rGO/Fe_2O_3 can be a promising nanocomposite active electrode material that can be used as negative electrode material in alkaline SCs. Regarding the synthesis of the positive

electrode material, here I proposed a small adjustment of the ED method developed in our preceding work (section 4.1) [136].

Table 5. 1 Capacitive controlled and diffusion-controlled charges estimated at different scan rates in Fe_2O_3 and rGO/Fe_2O_3

Scan rate	Fe_2O_3		rGO/Fe_2O_3	
mV s^{-1}	Capacitive controlled %	Diffusion controlled %	Capacitive controlled %	Diffusion controlled %
200	31	69	87	13
100	32	67	82	18
50	25	75	77	23
20	18	82	54	46
10	13	87	46	54
5	10	90	52	48
2	6	94	40	60

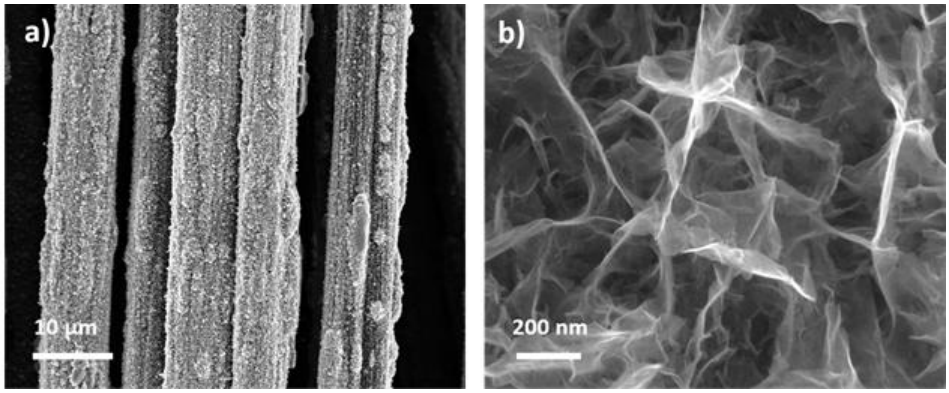

Figure 5.7 Characterization of MnO_x /CF material. FESEM images at low (a) and high magnification (b)

The deposition of MnO_x nanostructures were obtained in 2-step process to promise a proper coverage of the CFs, as displayed in low-magnification images such as Figure 5.7a. Furthermore, the typical nanosheet morphology of the MnO_x nanostructures (Figure 5.7b) is reserved through the 2-step deposition, leading to a uniform, high specific surface area active electrode material for SCs application (detail in sction 4.2 regarding FESEM and physical characterizations). Considering the electrochemical performance of MnO_x, the charge-storage mechanism in manganese oxide is analogous to that of untreated MnO_2 with Faradic reactions taking place both on the surface and in the bulk of the electrode. The surface Faradaic interactions include the adsorption/desorption of alkali metal cations (denoted as cat^+ like H^+, Li^+, Na^+, K^+) on the MnO_x in alkaline electrolyte:

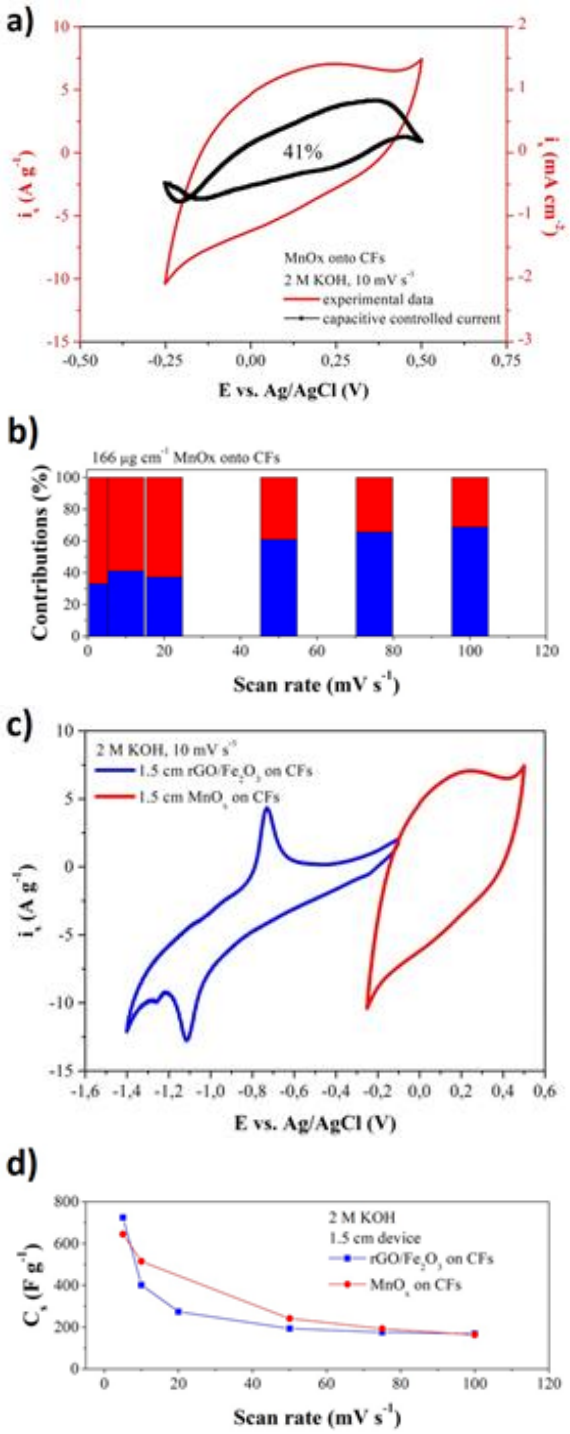

Figure 5. 8 Electrochemical experiments on flexible electrodes: reconstructed voltammograms of the capacitive controlled current contribution to the total current in the voltammetry (a) and estimation of the charge stored by diffusion-controlled phenomena (red) and capacitive controlled phenomena at different scan rates (b) of MnO_x/CF. (c) cyclic voltammetry of rGO/Fe_2O_3/CF (negative electrode, blue) and MnO_x/CF (positive, red) at 10 mV s^{-1} vs Ag/AgCl as reference electrode; (d) specific capacitance of the negative and the positive measured at multiple scan rates.

$$MnO_{2_{surface}} + cat^+ + e^- \underset{\leftarrow}{\overset{\rightarrow}{}} MnO_2^- cat^+_{surface} \qquad 5.7$$

This mechanism was proposed to be dominant in amorphous manganese dioxide or when the sample offer large surface area and it was accompanied with optimum particle size and pore distribution. The second proposed mechanism happens to be dominant for crystalline manganese dioxide in which the crystallographic lattice offers tunnels in which restricted Faradaic reactions with intercalation and deintercalation of electrolyte cations occurs:

$$MnO_2 + cat^+ + e^- \underset{\leftarrow}{\overset{\rightarrow}{}} MnOOcat \qquad 5.8$$

In both charge storage mechanism [143], [201], the oxidation and reduction reactions take place between Mn^{+3} and Mn^{+4}. According to the time-dependent data examination previously reported, the capacitive-controlled capacitance is remarkably high in the sample of MnO_x and it dominates at high rates (above 50 mV s^{-1}) as reported in Table 5.1 and in Figure 5.8a. In Figure 5.8b, the recreated voltammogram of the capacitive-controlled current for the manganese oxide nanostructured electrodeposited on carbon fibers (MnO_x/ CF) at sweep rate (10 mV s^{-1}) is reported along with the one experimentally achieved: the large contribution (41 %) of the capacitive-controlled charge on the overall phenomena is clear. The semi-rectangular profile of the voltammograms at all the sweep rates indicates a fast charging/discharging process that occurs at almost constant rate even for solid state diffusions. The renowned pseudocapacitive behavior of manganese oxide and its potential window in alkaline conditions make this material a potential candidate to be composited with the graphene-based iron oxide nanocomposite. In fact, Figure 5.8c demonstrate the comparison of CV profiles of rGO/Fe_2O_3/CF as negative electrode and MnO_x/CF as positive electrode in three electrodes set up (2M KOH). Figure 5.8d shows the comparison of the specific capacitance in mass of the carbon fiber-based electrodes having similar electrochemical behavior and values.

5.1.4.3 Two- electrode electrochemical characterization

After doing mass balancing with three electrodes set up in aqueous electrolyte, two electrode experiments were performed in usual 2M KOH aqueous electrolyte, but to study the potentialities of the flexible electrodes, a hydrogel electrolyte comprises PVA in 2M KOH was tested and compared with the aqueous electrolyte soaked in a glass-fiber membrane. In the latter arrangement, in fact, the flexibility of the device is immensely restricted by the presence of the rough membrane, which, upon bending, can strip away the active electrode material from the substrate. In comparison to the 2M KOH aqueous electrolyte, hydrogel electrolyte

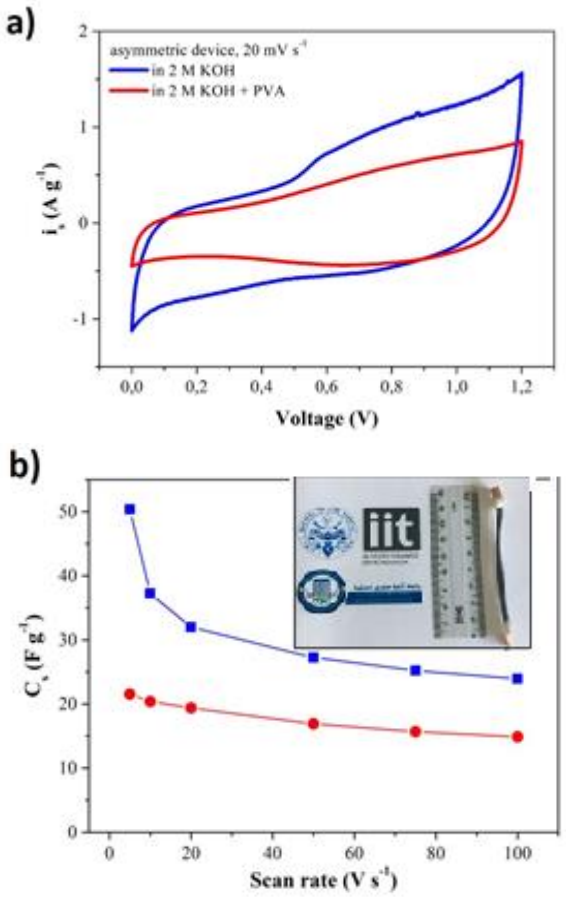

Figure 5.9 Experiments on flexible devices: (a) comparison of CV at 20 mV s^{-1}, (b) specific capacitance, inset of (b) shows the digital photograph of the assembled flexible asymmetric supercapacitor.

owing to its high viscosity offers a larger resistance (larger ESR in the Nyquist plot in the EIS), thus it reduced the total capacitance of the device. Figure 5.9a

Table 5. 2 Capacitive and diffusion-controlled charges at different scan rates in MnO_x/CFs

Scan rate mV s^{-1}	Capacitive controlled %	Diffusion controlled %
100	69	31
75	66	34
50	61	39
20	37	63
10	41	59
5	33	67

demonstrated that the device exhibits higher current in the aqueous electrolyte as compared with that achieved in gel-electrolyte. As it can be seen in Figure 5.9b, the specific capacitance reduced almost half, what achieved with aqueous

electrolyte 2M KOH for all the scan rates. However indeed, the bending stability of the hydrogel device at multiple angles and the cyclic stability are improved: during cycling the specific capacitance of the device initially increases until 250 cycles and then it gradually drops back to its initial value at 2500 cycles as shown in Figure 5.10a. In the inset of the Figure 5.10a, bending of the device elicits a progressive decrease in the specific capacitance from flat position (0° no bending on right hand side) up to a bending at 180° in which the 75 % retention of its initial capacitance sustained.

Ragone plot is used to compare the performance of various energy-storing devices. On such a graph, the values of specific energy density (in W·h kg^{-1}) are plotted vs specific power density (W kg^{-1}). Both axes are logarithmic, which allows comparing performance of very different devices. Specifc energy and specific power density of the SCs devices were also evaluated for both aqueous as well as hydrogel electrolyte and Ragone plot is reported in Figure 5.10b in order to permit a comparison of the proposed device, with similar PVA based SCs devices previously reported in the literature. The energy and power density obtained in this study are comparable with other materials.

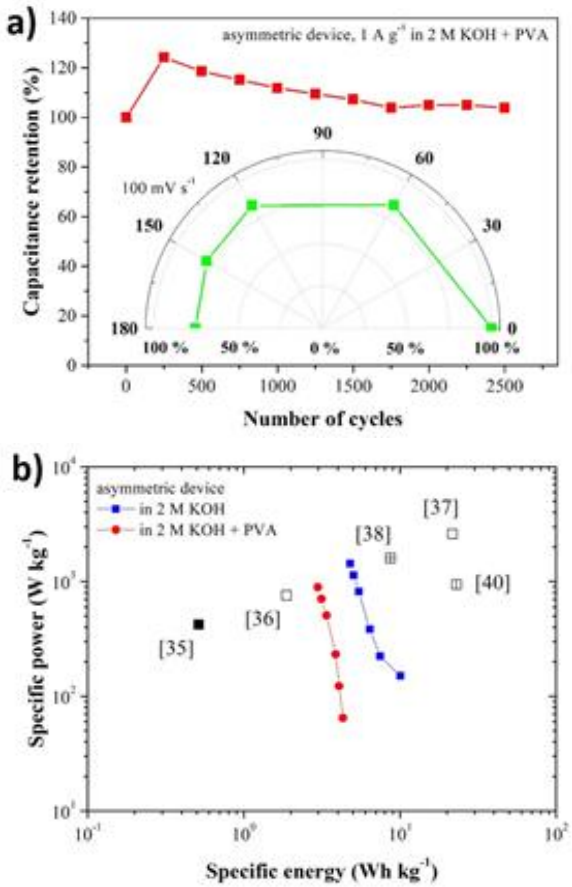

Figure 5.10 (a) Capacitance retention over 2500 cycles and bending stability at different angles on the flexible device with hydrogel. (b) Ragone plots of the devices recorded when 2M KOH (blue) and hydrogel (red) are employed, compared with literature results.

5.1.5. Conclusion

The synthesis of a rGO/Fe_2O_3 nano-composite was achieved by hydrothermal route exploiting olive leaves extract as green surfactant. After profound physico-chemical characterization the attained material was used as negative electrode material into an asymmetric fiber-shaped SC in combination with manganese oxide as positive electrode material. The outstanding capacitive performance of the rGO/Fe_2O_3 nanocomposites (established by a specific capacitance value higher than 700 F g^{-1} in three electrode arrangement measurements) is attained, thanks to the synergetic higher conductivity of rGO and the mesoporous structure of hematite nanoparticles. rGO framework permits to: (i) anchor Fe_2O_3 nanoparticles maximizing the coverage, thanks to the large surface area of rGO sheets, (ii) optimize the utilization of the active material offering a large electrode/electrolyte interface, (iii) reduced diffusion path length to adsorption/desorption of ions and (iii) offer improve kinetics of electron transfer. Furthermore, the well-dispersed iron oxide nanoparticles avert the agglomeration and the restacking of rGO nanosheets producing a large surface area accessible for the energy storage.
The fabricated ASC device permits to attain capacitance values higher than 50 F g^{-1} in aqueous environment and more than 20 F g^{-1} in hydrogel electrolyte, demonstrating promising cycling stability and excellent capacitance retention under bending conditions. The attained results confirm the high potentialities of rGO/Fe_2O_3 nanocomposite material as negative electrode in fiber-shaped alkaline SCs.

5.2 MoS_2//H-MnO_x based flexible high energy asymmetric SCs

5.2.1 Introduction

In this part of the chapter, MoS_2 is used as negative and hydrogenated manganese oxide denoted (H-MnO_x) as positive electrode material (details are given in chapter 5) for the fabrication of the ASCs. MoS_2 has a layered structure and exist in two different phases [202]: i) 2H-MoS_2 phase, which is a semiconductor with a monolayer direct bandgap ~ 1.67 eV and ii) 1T phase which is metallic and possess conductivity 10^7-times higher than 2H phase. 1T phase has favorable electrochemical characteristics along with excellent hydrophilicity, electrical conductivity and ability to intercalate electrolyte ions. It has structure comparable to graphite and its large specific surface area, fast ionic conductivity and the 2D-like morphology make it a potential candidate for using as negative electrodes material in SCs [202]–[204]. MnO_2 can be easily electrodeposited onto current collectors by anodic or cathodic electrodeposition [205]–[207] and this soft-chemical method was chosen to nicely coat CFs current collectors. In this study, the pseudocapacitve performances of manganese oxide with oxygen vacancies (MnO_2-x) have been exploited showing better performance than MnO_x without any reduction [162]. Employing CFs as a support, the effective utilization of active materials and the mechanical strength of the electrodes increases due to their high flexibility that won't be achieved with metallic wires. Moreover, their reduced weight and costs make flexible modified carbon-based devices with high performances extremely appealing to meet the great demand of practical applications. Here, cyclic and bending stability of the flexible device was also demonstrated in a wide voltage window (1.8 V).

5.2.2 Experimental

In this section, the detail about the synthesis of the electrode material and fabrication of the fiber shaped SCs is presented.

5.2.2.1 Reagents

All the reagents and chemicals used for preparation and synthesis of MnO_x were of analytical grade and used as received without any further cleansing. The reagents and chemical used for synthesis are: Manganese acetate Tetrahydrate Mn $(CH3COO)_2.4H_2O$ > (98 % Sigma-Aldrich), Na_2SO_4 (98% Sigma-Aldrich), distilled water. PVA (Mw 89,000-98,000, 99 % hydrolyzed Sigma-Aldrich) and KOH (Potassium

Hydroxide, ≥90%, Flakes Sigma-Aldrich), Phosphomolybdic acid hydrate, ≥99.99% trace metals basis, Sigma Aldrich, L-Cysteine 97%-Sigma-Aldrich, Sodium hydroxide ACS reagent, ≥97.0%, pellets.

5.2.2.2 Electrodeposition of MnO_x and hydrogenation to H-MnO_x

The fabrication of H-MnO_x electrodes onto CFs was carried out by annealing the as deposited MnO_x on CFs under a constant hydrogen flow at 250 °C for 3.5 h (2.5 °C per min ramp). Those samples are labelled as H-MnO_x/CFs. (detailed procedure of synthesis was described in section 4.2)

5.2.2.3 Synthesis of MoS_2 flakes and electrodes fabrication

The synthesis of MoS_2 flakes was carried out with a simple hydrothermal method: 106 mg of phosphomolybdic acid hydrated and 170 mg of L-cysteine were added to 17 mL of dH_2O. Before the amino acid was added, the pH of the solution was adjusted to 6.5 by adding 1M NaOH dropwise in the solution that was further sonicated for 30 min and it was transferred into the autoclave reactor. The hydrothermal reduction was carried out at 180 °C for 12 hours in the muffle oven and, after cooling down to room temperature, the solution was centrifuged at least 3 times at 4000 rpm for 1 hourr with distilled water to remove the excess of reactants and soluble products. The flakes were then garnered in 10 mL distilled water and this dispersion was directly drop-casted onto the CFs until the desired mass per length was obtained. No addition of binder was employed.

5.2.3 Characterization

Physical characterizations are described in detail in chapter 3 and chapter 4 experimental sections. The capacitive behavior of the H-MnO_x and MoS_2 coated fibers was carried out in a three electrodes cell in 1M Na_2SO_4 purged with nitrogen for 20 minutes prior to perform any experiment. Platinum bar and Ag/AgCl sat KCl were employed as counter and reference electrodes respectively. Cyclic voltammetry at multiple scan rates was carried out between [-0.6-0.15] V vs. Ag/Ag^+ and [0.1- 0.85] V vs. Ag/Ag^+ for MoS_2 and H-MnO_x CFs electrodes, respectively. In the asymmetric devices the mass or length of the MoS_2/CFs electrode was tuned to counterbalance the charges stored on the H-MnO_x/CFs electrode. Devices with liquid electrolyte and hydrogel (PVA in 1M NaCl) were characterized by means of cyclic voltammetry, chronopotentiometry in 1.8 V of voltage window and AC Impedance spectroscopy at 5 mV amplitude between 100 kHz and 10 mHz. Moreover, to appreciate the potential candidacy of these devices, the capacitance retention was investigated at different bending angles. The devices were sealed in between two of Kapton® tapes. All of these experiments were performed with a Metrohm Autolab M101 potentiostat/galvanostat and Nova 2.1.

5.2.4. Results and Discussion

This section contained detailed information about the results obtained after physical characterization such as FESEM, XRD, Raman, XPS and detailed electrochemical analysis of the negative electrode (MoS_2/CF), and positive electrode (H-MnO_x /CF).

5.2.4.1 Physical characterization of cathode

Free-standing highly porous H-MnO_x nanoflakes were synthesized via 2-step process. In the first process template free manganese dioxide nanoflakes were synthesized by 2-step ED process (details in the experimental section 4.2). In the anodic ED of MnO_x onto CFs, an electrode proceeds with the diffusion of charged electroactive species through the electrolyte, when an electric field is applied and consequently oxidation of the charged species occurs in form of the deposition on the surface of the substrate. The electro-oxidation of Mn(II) [48], [206]–[208] species on the CFs electrode follows this reaction:

$$Mn^{2+} + 2\,H_2O \;\rightarrow\; MnO_2 + 4\,H^+ + 2\,e^-$$

A careful study on the behavior of the as synthetized MnO_2 films produced by tuning the electrodeposition parameters is such as time and current density of the deposition details in section 4.2.

Field emission scanning electron microscopy (FESEM) characterization was performed on the 2-step ED MnO_x to study the surface morphology of the obtained electrode as described in detail in chapter 5. Figure 5.11a shows the 2-step ED of the MnO_x and it is clear from the image that fibers are uniformly covered and there were no cracks or gap in the film and nanoflakes with thickness < 10 nm, are continuous and interconnected. To introduce oxygen vacancies into these MnO_x nanoflakes, they were further subjected to thermal treatment under hydrogen environment at 250 ^oC for 3.5 hours as described in experimental section. Figure 5.11b-c shows the higher magnification images of the 2-step MnO_x and H-MnO_x. It can be seen that the structure of manganese oxide film before and after the hydrogenation process is almost unchanged, but this hydrogenation treatment introduced more porosity in the nanoflakes. The XRD and XPS measurements details are given in section 4.2.

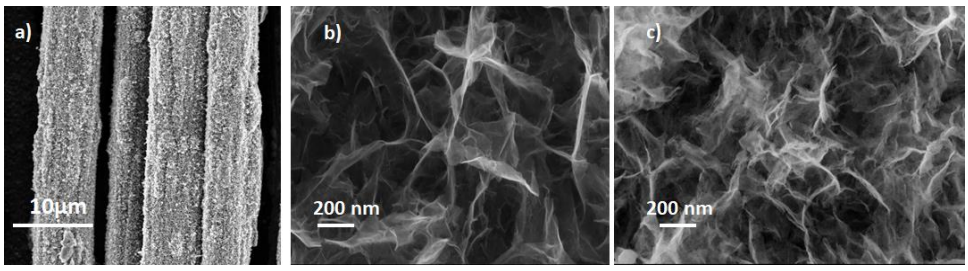

Figure 5.11 Figure: a) 2-step electrodeposition of the MnO_x, b-c) higher magnification images of the of 2-step MnO_x and H-MnO_x

5.2.4.2 Physical characterization of negative electrode

Figure 5.12a shows schematic representation of the fabrication of the CFs based electrode in which MoS_2 nanoflakes were dip-coated on CFs. Earlier, MoS_2 nanoflakes were hydrothermally synthesized using phosphomolybdic acid and L-Cystine as precursor in an autoclave at 180 ^oC for 12 hours (detail in experiment section). For electrochemical SCs applications, the surface structure of the electrode material has significant influence on electrochemical properties as electrochemical redox reactions occur at or near the surface of electrode.

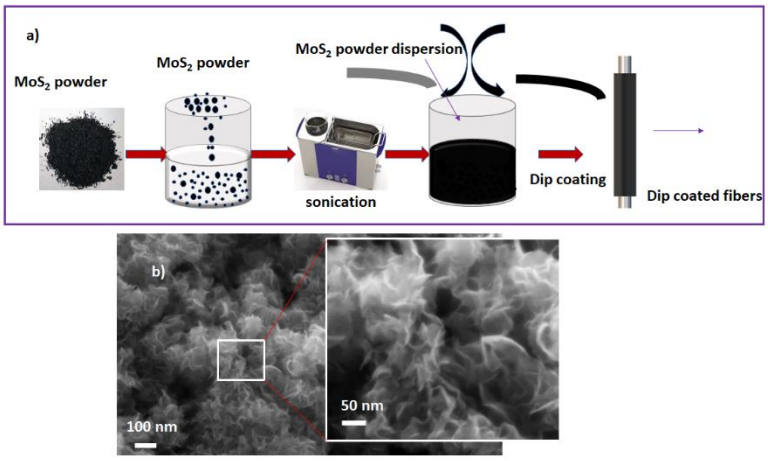

Figure 5.12 a) Schematic representation of fabrication of the electrode, b) image of MoS_2 nanoflakes (inset higher magnification image of layer MoS_2 nanoflakes).

FESEM measurement was performed to study the morphology of the synthesized material at nanoscale level. As the MoS_2 nanoflakes (1T/2H phase) are conductive so no metallic coating was performed. Figure 5.12b shows the surface morphology of MoS_2 thin film at two different magnifications. The surface of deposited MoS_2 thin film reveals the formation of nanoflakes. The nanoflakes morphology is advantageous for efficient ion/electron transport and for better accommodating the volume variation [209]. From the inset high magnification image, it is evident that MoS_2 nanoflakes are composed of few layers structure with thickness < 5 nm and literal length < 100 nm. TEM measurements were performed to further clarify the

morphological structure of the MoS_2 nanoflakes as shown in Figure 5.13. TEM images as shown Figure 5.13a and corresponding selected area diffraction is reported in Figure 5.13b. It is clear from the diffraction pattern that diffraction pattern is diffused, so there is no clear indication about single crystal structure but a stack of few layers which is in good agreement with the results obtained from SEM. Such nanoflakes structure with such a small dimension offers a very small path length for electrolyte ions which is good for SCs application.

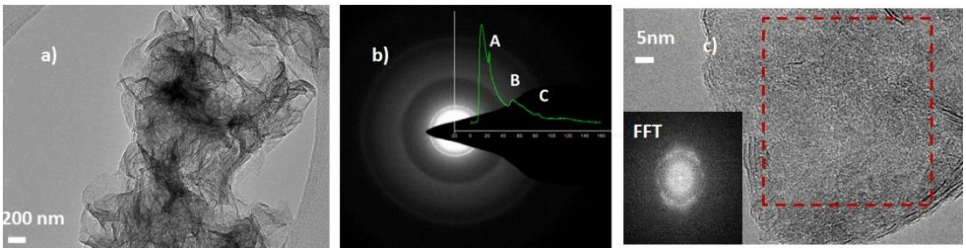

Figure 5.13 a) TEM image of MoS_2 nanoflakes, SEAD pattern for images and layered pattern

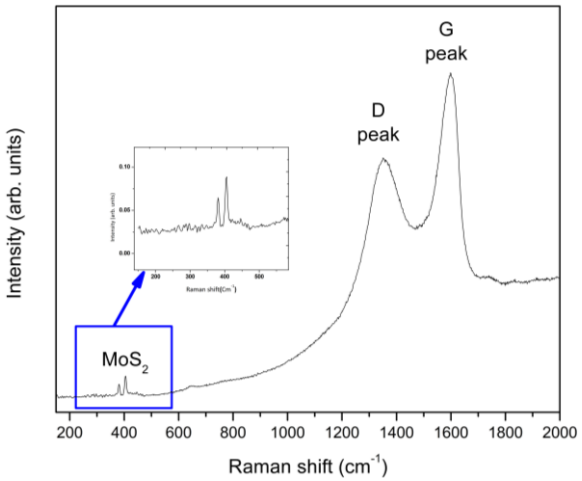

Figure 5. 14 Raman spectra of MoS_2

The Raman spectra of the MoS_2 nanoflakes decorated CFs was obtained as shown in Figure 5.14. The two main peaks related with carbon (originated from carbon fibers substrate) are clearly visible: D peak at wavenumber 1350 cm^{-1}, corresponding the decrease in the size of the in-plan sp^2 domains induced by the creation of the defects, vacant species or bent sp^2 bonds. The G peak at 1594 cm^{-1} originating from first order inelastic scattering procedure including degenerate iTO and iLO phonons at the G point corresponding E_{2g}(mode) [202]. It can be seen two vibrational band appeared at lower wavenumbers 383 cm^{-1} (A_{1g}) and 408 cm^{-1} (E_{2g}) as shown in the inset of Figure 5.14. They are the characteristic vibrations of the MoS_2 compatible with former owed to the presence of few layers of 2H MoS_2, (opposing vibration of two S atoms with respect to the Mo atom) and latter

symmetric stretching vibrations of the Mo-S of the MoS_2 [202][210]. It is clear from the spectra that intensity of the signal is low because of the very low loading of the material on the substrate structure.

XPS, while permitting for structural composition identification, has a sampling depth <10 nm [202]. Therefore, it is beneficial to investigate the chemical composition of active materials exploited for SCs applications, since electrochemical performance SCs is disparagingly affected by surface or near-surface phenomena within the active material. Figure 5.15a-b are the high-resolution scans of the Mo 3d and S 2p regions and contain lot of information about S through S 2s core peak level. Figure 5.15a show Mo 3d spectrum contains two strong doublet peaks positioned at 229.3 eV and 232.4 eV and S 2s peak 226.5 eV are compatible with MoS_2 chemical structure which confirms the formation of MoS_2 [211]. It is also clear from the Mo 3d spectra that the existence of two Mo 3d doublets first at 228.7, 231.8 eV, second at 229.6 ,232.7 eV respectively with the energy gap of ~ 0.9 eV can be ascribed to the co-existence of 1T and 2H MoS_2 polymorphs [203]. Similarly, in Fig 4.15b, the presence of two doublet in S 2p spectrum at 161 and 163 eV and 163.5 and 164.6 eV respectively, which correspond to the $S2p_{3/2}$ and $S2p_{1/2}$ orbitals of the divalent sulfide ions (S^{-2}) respectively [212].

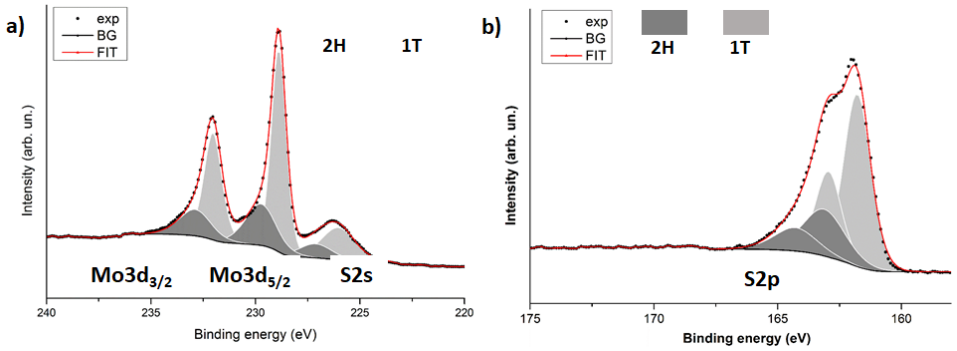

Figure 5.15 XPS spectra of MoS_2

5.2.4.4 Electrochemical characterization

The behavior of MoS_2/CFs and H-MnO_x/CFs as electrodes for supercapacitors was first investigated in 1M Na_2SO_4 by a three electrodes configuration in which the modified fibers were used as the working electrodes and a platinum bar and a saturated Ag/AgCl were employed as counter and reference electrode, respectively. In Figure 5.16a-b, the cyclic voltammograms recorded at at 5 mV s^{-1} scan rates for both the electrodes H-MnO_x and in order to appreciate the perfect match of their voltage windows. In this experiment, the length of the MoS_2/CFs was increased to 2.5 cm with respect to the length of the H-MnO_x/CFs electrode in order to match the charges stored by the two electrodes. The good capacitive performance of the H-MnO_x electrodes were studied and compared with the behavior of the same sample prior to the hydrogenation [detail in section 4.2] showing

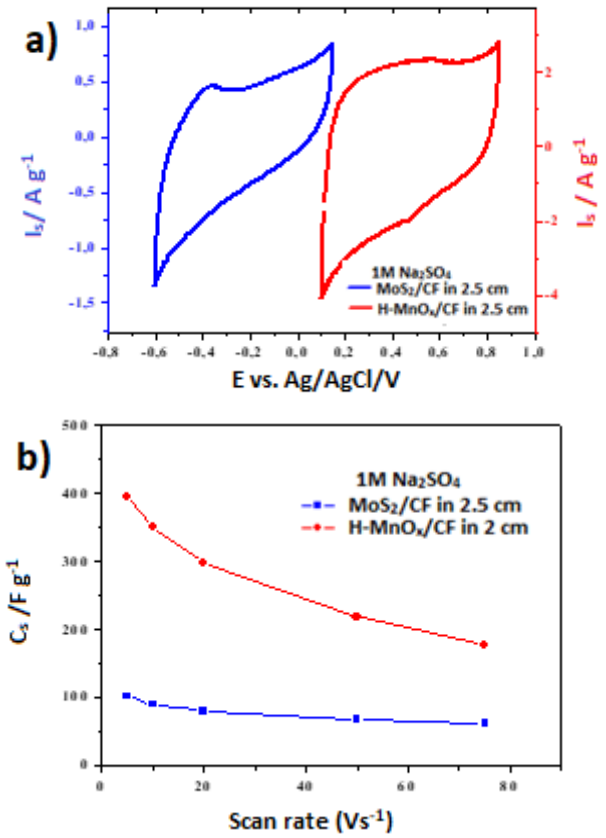

Figure 5.15 a) CVs of negative and positive electrodes in respective voltage windows, d) comparison of the specific capacitance vs scan rates

superior characteristic as storage material of the former. H-MnOx/CFs electrodes were tested in the potential window between [0.1-0.85] V vs. Ag/AgCl and CV shows quasi-rectangular shapes at all the scan rates employed. The capacitive performances of the MoS_2 electrode relies in the mixed 1T-2H phases obtained by simple hydrothermal synthesis [201] of the flakes that are nicely attached onto the CFs without any binder. Cyclic voltammograms recorded at different scan rates show that the potential window of [-0.6-0.15] V vs. Ag/AgCl is smaller with respect to acidic electrolytes (1M H_2SO_4) [202] and it reaches 0.75 V.

Charge storage diffusive or capacitive

Figure 5.15b, shows the comparison of the specific capacitances of the two electrodes. According to this plot, for MoS_2 electrodes, the capacitance remains almost constant up to 20 mV s^{-1} and for lower scan rates it increases. On contrary for the H-MnO_x electrode, the specific capacitance rises with the decrease of the scan rate, therefore the total amount of stored charges is strongly time dependent. This indicates that charges have enough time to penetrate in bulk of the material at lower scan rates. In order to understand the charge storage mechanisms

of the two different electrodes, the total charge has to be separated in three components: the faradaic currents obtained from ion insertion, the faradaic currents

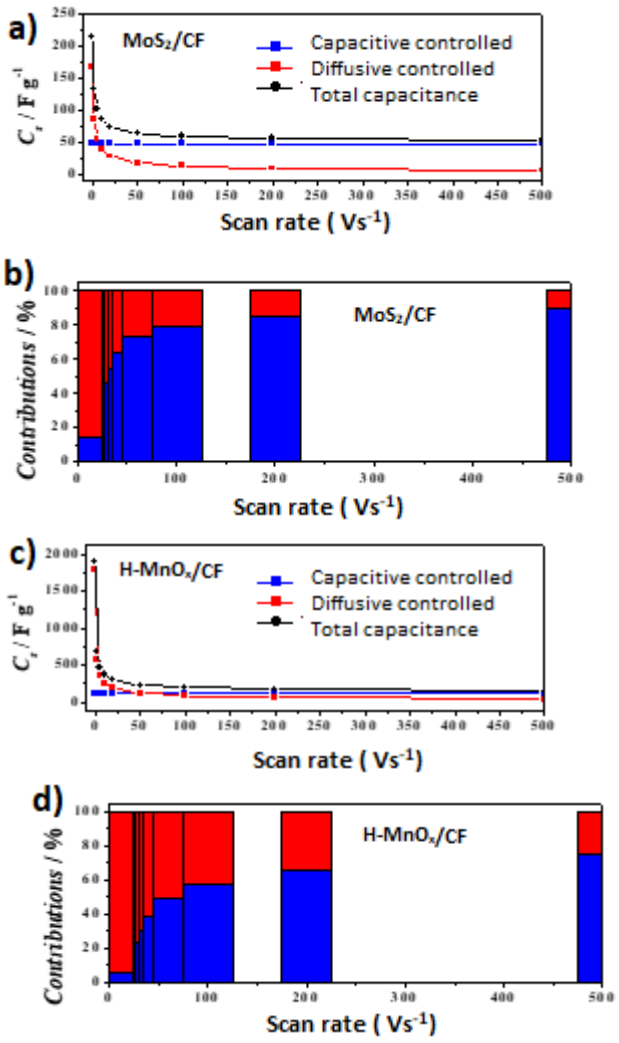

Figure 5.16 (a-d) Estimation of the charge stored by diffusion-controlled phenomena (red) and capacitive controlled phenomena (blue) at different scan rates on MoS_2/CFs (upper graphs graph) and H-MnO_x/CFs (lower graphs graph).

from charge-transfer processes with surface and interlayer atoms giving rise to the pseudocapacitance, and the non-faradaic currents due to the double-layer capacitance [48], [213],[214]. The first process is diffusion-controlled, so the current is proportional to the square root of the scan rate ($\nu^{1/2}$), while the two latter phenomena are capacitive-controlled with the current proportional to the scan rate (ν) as described in section 5.1. In the MoS_2 electrodes the capacitive controlled mechanism predominates for scan rates higher than 10 mV s^{-1} (55 %) and in the H-MnO_x electrodes for scan rates higher than 100 mV s^{-1} (58%). For lower scan rates, the diffusion-controlled current becomes predominant as clearly seen in the red plots in Figure 5.16a and Figure 5.16c. In Figure 5.16a-c in fact, shows the specific capacitance, was recalculated according to the constants k_a and k_b previously

estimated up to 0.2 mV s^{-1} and exhibit the partition of the charges due to the two phenomena are visualized as percentage on the total capacitance. In Table 5.3, the diffusion-controlled capacitance is compared at different scan rates, suggesting that the charge storage mechanism in MoS_2 is mainly capacitive controlled and in H-MnO_x, it is mainly diffusion-controlled in the timescale of the experiments performed.

Table 5. 3 Diffusion controlled capacitance estimated at different scan rates in MoS_2/CFs and H-MnO_x/CFs

Scan rate	MoS_2/CFs		H-MnO_x/CFs	
V s^{-1}	%	F g^{-1}	%	F g^{-1}
0.2	15	9	34	57
0.02	37	27	62	179
0.002	65	86	84	567
0.0002	86	167	94	1793

Figure 5.17a-b show the experimental voltammetry (black line) with the simulated capacitive-controlled current (blue line and dots), diffusion-controlled current (red line and dots) and the sum of them (black line and dots) for MoS_2/CFs and H-MnO_x/CFs, respectively. According to the data analysis, the charge-storage mechanism in sub-stochiometric MnO_x (called H-MnO_x) is similar to that of untreated-MnO_x with Faradic reactions occurring both on the surface and in the bulk of the electrode. The surface Faradaic reaction involves the adsorption/desorption of alkali metal cations (called cat+ such as H^+, Li^+, Na^+, K^+) on the manganese oxide in neutral electrolyte:

$$MnO_{2_{surface}} + cat^+ + e^- \underset{\leftarrow}{\overset{\rightarrow}{}} MnO_2^- cat^+{}_{surface}$$

This mechanism was suggested to be predominant in amorphous MnO_2 or when the sample presents large specific surface area [169] and it was associated with optimal particle size and pore distribution. The second mechanism was suggested [73], [215] to be predominant for crystalline MnO_2 in which the crystallographic cell provide tunnels in which limited Faradaic reactions with intercalation/deintercalation of electrolyte cations takes place:

$$MnO_2 + cat^+ + e^- \underset{\leftarrow}{\overset{\rightarrow}{}} MnOOcat$$

In both charge storage mechanisms, the redox reaction occurs between Mn(III) and Mn(IV). According to the time-dependent data analysis previously described, the diffusion-controlled capacitance is significantly high in the sample H-MnO_x not

only at lower scan rates but also at dominates higher scan rates (100 mV s^{-1}). The main mechanism is therefore the intercalation/deintercalation of cations or protons into/out the MnO_x nanostructures. The distorted conventional rectangular shape of the voltammograms (parallelogram like) at all the scan rates indicates a fast charge/discharge process that happens at almost constant rate even for solid state diffusions. This may be due to the thermal treatment in hydrogen atmosphere that enhances the surface porosity and generates high surface area with more active Mn(II) and Mn(III) sites for a rapid intercalation and extraction of cations. In MoS_2/CFs, the semi-rectangular nature of the CV curves indicates the capacitive behavior of such electrodes. The deviation from a perfect rectangular behavior can be attributed to the electro sorption of protons on the surface of the nanosheets [216]. The adsorption of H^+ leads, in fact, to the formation of molecular hydrogen and evolution of the gas not only in acidic media [217]–[219], but also in neutral electrolytes [209]. As

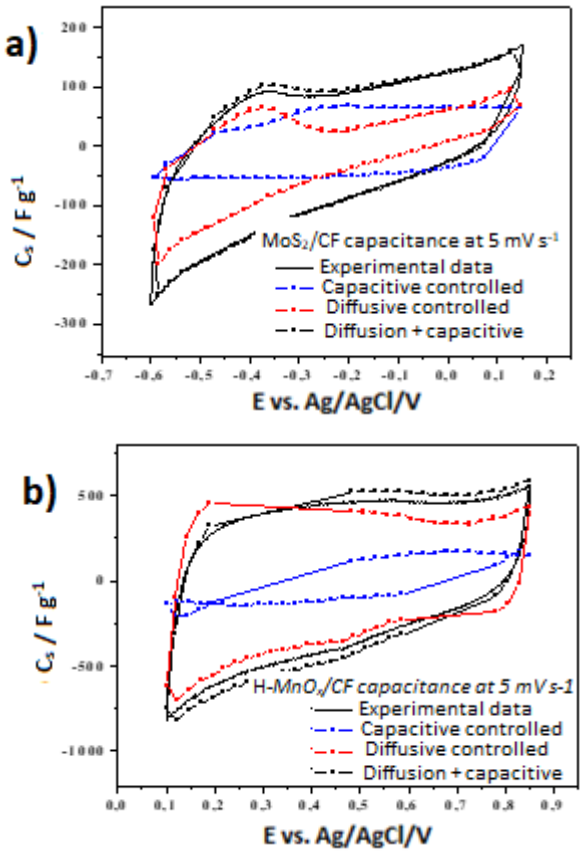

Figure 5.17 a-b) Comparison experimental voltammetry (black line) with the simulated capacitive-controlled current (doted blue line), diffusion-controlled current (doted red line) and the sum of them (doted black line) for MoS_2 /CFS and H-MnO_x/ CFs

discussed above in the XPS and TEM paragraphs, the hydrothermal synthesis employed in this study allows to obtain a mixed 1T-2H phase of MoS_2 and the electrodes were fabricated simply by drop-casting the suspension on the CFs without any binder. This makes very challenging to identify a univocal onset potential of

the HER from sample to sample and therefore decide the lower potential of the voltammetry to study the double layer formation and pseudocapacitive behavior only. In 2D-MoS_2 flakes, the nature of the storage mechanisms [220], [221] are the formation of the electrical double layer with the adsorption/desorption of ions:

$$MoS_{2_{surface}} + cat^+ + e^- \underset{\leftarrow}{\overset{\rightarrow}{}} MoS_2^- cat^+{}_{surface}$$

and the pseudo capacitance [203], [221] with the insertion/extraction of protons and alkali cations between the interlayer spaces:

$$MoS_2 + cat^+ + e^- \underset{\leftarrow}{\overset{\rightarrow}{}} MoS - Scat$$

Both these two phenomena are capacitive-controlled in nature, that is in fact the main contribution of the total current of MoS_2/CFs samples (Figure 5.16 a) unless very slow rates of charge and discharge are applied. When very slow voltammetry is performed, the diffusion-controlled phenomena start to take place and get over. This current can be due to diffusion phenomena that take place not only on the MoS_2 active material, but mainly, and it may be the case, on the CFs substrate that is partially exposed to the solution due to the absence of a binder or a compact/blocking layer (like in the case of MnO_{2-x} electrodes) as it has been observed for different carbonaceous materials [222].
AC impedance spectroscopy measurements were carried out at the open circuit

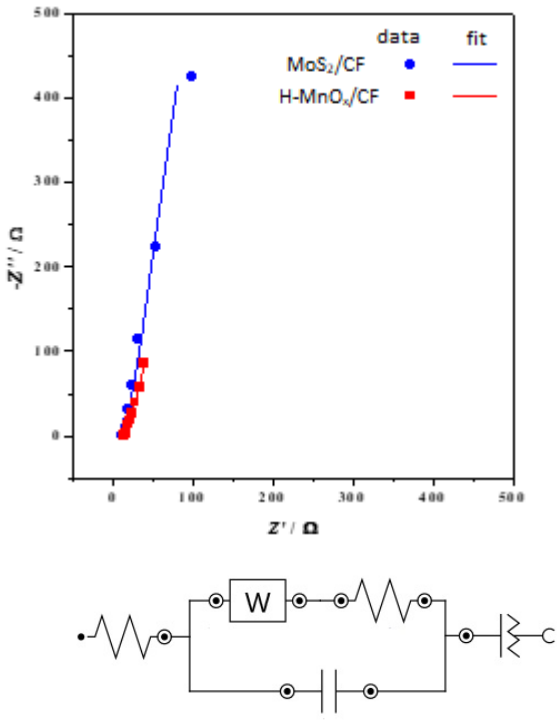

Figure 5.18 Comparison of AC impedance spectra (a) Nyquist plot up to 10 mHz of the MoS_2/CFs electrode (blue) and H-MnO_x/CFs electrode (red).

potentials of each electrode. From the data fitting, it is possible to appreciate the uncompensated resistance (highest frequencies) characteristic of each material, the constant phase element (lower frequencies) that mimic imperfect capacitor (EDLC and pseudocapacitance) and the Randles circuit in which the Warburg impedance (medium frequencies) describe the diffusion-controlled phenomena previously analyzed and commented in the text. The uncompensated resistance is 14.6 Ω and 11.9 Ω while the charge transfer resistance is 0.9 Ω and 2.5 Ω for H-MnO_x/CFs and MoS_2/CFs electrodes respectively.

5.2.4.5 Electrochemical characterization of two electrode device

After the 3-electrode electrochemical study of the single electrodes and making current balances, the MoS_2/CFs and the H-MnO_x/CFs electrodes were employed as neagtive electrode and as positive electrode in ASCs. With this intent, two

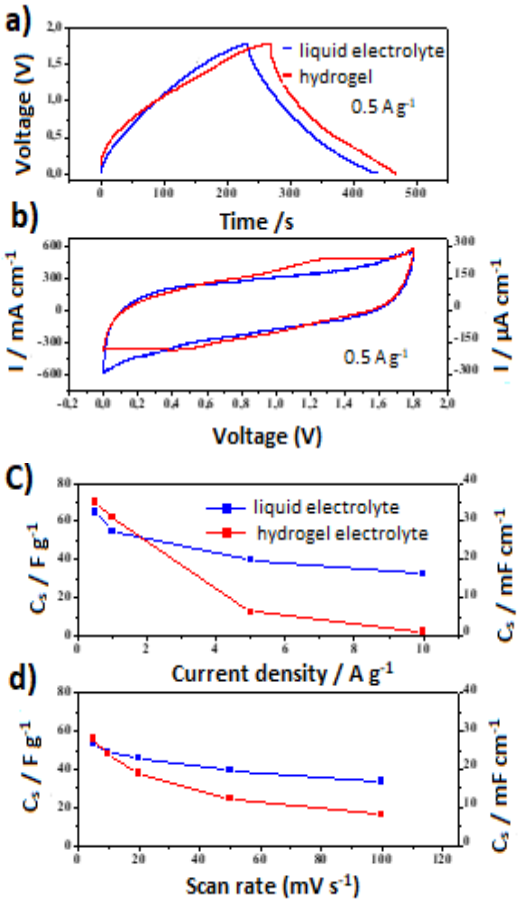

Figure 5.19 Electrochemical experiments on flexible devices employing liquid electrolytes (blue) and hydrogel (red): (a) Charge and discharge at 0.5 A g^{-1} (upper), b) cyclic voltammetry at 5 mV s^{-1} (lower); (c-d) specific capacitance estimated on charge and discharge experiments (upper) and cyclic voltammetry (lower)

configurations of ASCs were chosen: (i) standard asymmetric device by using 1M Na_2SO_4 electrolyte (called liquid electrolyte) and (ii) asymmetric device by using PVA based gel (called hydrogel) to make the cell appealing for commercial flexible devices with excellent bending stability over multiple angles. Figure 5.19a-b shows

the comparison of charge-discharge profiles (upper graph) and CV (lower graph) of the devices in liquid electrolyte and in hydrogel electrolyte. The two methods show consistent behaviors at multiple current densities and scan rates: as shown in Figure 5.19c-d, the specific capacitance computed from the galvanostatic experiments and from

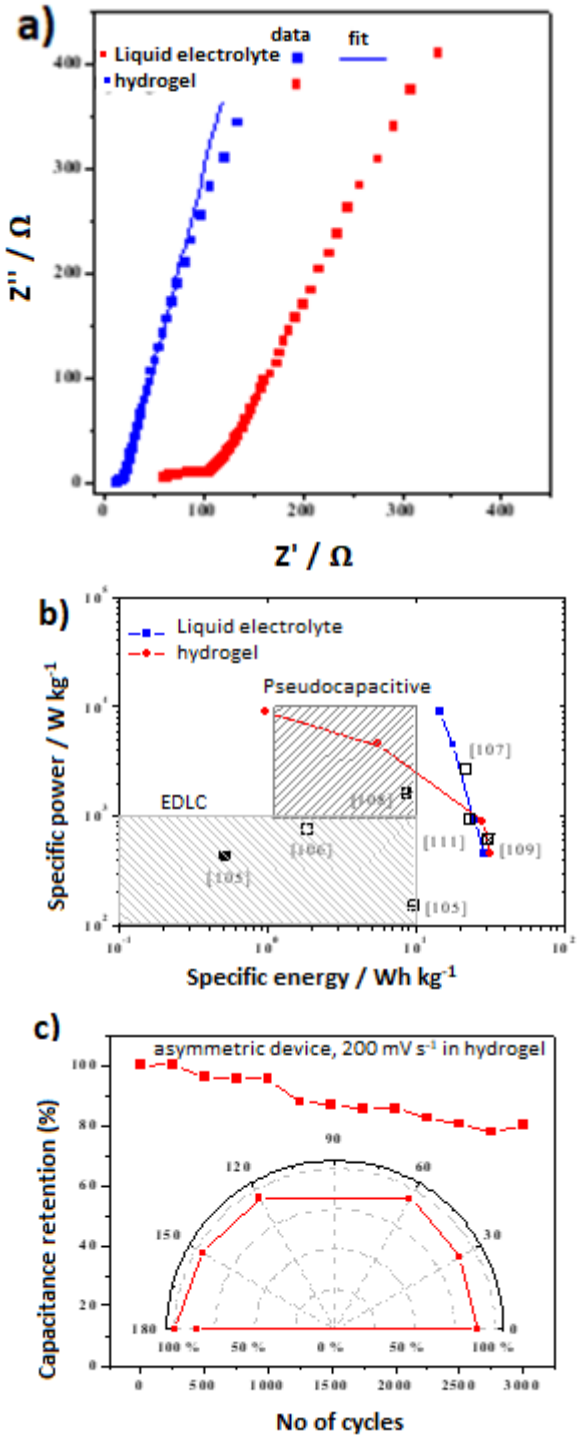

Figure 5.20 Electrochemical impedance experiments on flexible devices employing liquid electrolytes (blue) and hydrogel (red): a) Nyquist plot, (b) Ragone plot and (c) cyclability and bending stability.

cyclic voltammograms show that the devices made with hydrogel have larger capacitance at low rates, while the liquid electrolyte devices provide larger capacitance at higher rates. This unusual behavior may be produced by the larger uncompensated resistance of the hydrogel devices as shown in the Nyquist plot in Figure 5.20a in which Z' is null at 60 ohms (15 ohms in liquid electrolyte devices). Decreasing the rates of the experiments, the capacitance values of the two batches merge to quite the same value (i.e. the specific capacitances at 0.5 A g^{-1} current density are 65 F g^{-1} and 70 F g^{-1} respectively). Wearable and flexible devices are those in which the performances of the devices remain almost invariant, when the electrodes are bended, folded and wrapped. The presence of liquid electrolyte-soaked membrane, is a major limitation on the flexibility because by bending the device (i) the electrolyte moves, and this creates inhomogeneity at the electrode-electrolyte interface and (ii) the roughness of the membrane scratches the active material away from the fibers. With this aim, bending and ageing experiments were performed at multiple (shown in Figure 5.20c). From bending experiments, it was observed that the capacitance decreases 12 % with respect to the its initial value, when the device was completely folded (180°). The devices with hydrogel were cycled at 200 mV s^{-1} up to 3000 scans showing a capacitance retention of 80% that could be increased indeed by improving the packaging and sealing. The performances of the two devices are compared with the literature on flexible supercapacitors and plotted in the Ragone diagram in Figure 5.20b. It is possible to observe that the devices under study provide comparable power with respect to devices in literature, but their energy density improve mainly due to the working voltage i.e. 1.8 V which is a quite large voltage window for water-based supercapacitors.

5.2.5 Conclusions

Porous manganese oxide with oxygen vacancies (MnO_{2-x}) on CFs has been made by anodic electrodeposition and annealing in reducing atmosphere as flexible cathode. Two-dimension flakes of mixed phase 1T-2H of MoS_2 were synthetized by hydrothermal method and they were employed as binder-free active material on carbon fibers as flexible negative material. Asymmetric supercapacitors assembled with neutral electrolyte deliver at 0.5 A g^{-1} a device capacitance of 65 F g^{-1} (32 mF cm^{-1}) and when the gel electrolyte is employed, it increases up to 70 F g^{-1} (35 mF cm^{-1}). The latter layout allows not only to achieve higher level of capacitance, but also to use such device under bending conditions with very limited capacitance fading also after 3000 cycles. The present results demonstrate that these flexible hybrid devices which involve all the electrochemical storage mechanisms can increase the typical energy range and maintain the same speed (power) of PCs.

Chapter 6 Conclusion and Future prospect

"There are two possible outcomes;
if the results confirm the hypothesis,
then you've made a correct measurement
if results contrary to the hypothesis,
you've made a discovery".
—— Enrico Fermi.

In this chapter, a broad recap of the results discussed in this thesis is presented. As declared in Chapter 1, the first motivation, objective of this thesis activity is devoted to the efficient fabrication of solid-state SCs exploiting different flexible substrates used as current collector.
The second objective was to synthesize the other cost-effective free-standing nanostructures materials for SCs to overcome the limitation imposed by size, weight and binder (used for adhesion of active material with substrate) of the aqueous-electrolyte based SCs.

6.1 Conclusion of the dissertation

6.1.1. Wire- shaped SCs

ZnO/graphite-based nanocomposite slurries were prepared by varying the amount of ZnO nanoparticles (1, 5, 10, 20 % respectively) with respect to the weight of the graphite and dip-coated on copper wire for fabrication of wire-shaped electrode in view of the optimization of configuration of the solid state flexible SCs. ZnO/graphite based composite active material with 10% of ZnO showed the highest electrochemical performance as compared to other composite slurries due to the rational fabrication of the electrodes and the inherent advantage of the structures. In addition to electrochemical performance of the wire-shaped SCs, its bending and cyclic stability was also evaluated. Device has shown 4-time higher specific capacitance than pure graphite-based electrodes and shown an excellent energy and power density as compare to other materials in gel-polymer electrolyte.

6.1.2. Fiber-shaped SCs

In this activity, a systematic study was performed to fabricate free-standing MnO_2/CF based composite electrode exploiting potentiostatic and galvanostatic electrodeposition techniques. After selecting galvanostatic technique as best performing deposition, it was optimized by tuning deposition parameters such as current density and time. The growth mechanism of the MnO_2 nanostructures was investigated by FESEM, TEM and crystallographic study was conducted using XRD, Raman and XPS (to study chemical composition) techniques. It is observed that 2 hours deposition exhibits excellent electrochemical performance in terms of length specific capacitance (F cm^{-1}) and gravimetric capacitance (F g^{-1}) in gel-polymer electrolyte. The bending and cyclic stability measurements were also performed and device has exhibited excellent cyclic and bending stability. I have also calculated specific energy and specific power density and MnO_2/CF composite based solid state device exhibit higher energy and power density as compare to other PVA based solid state devices.
The deposition process is further optimized by:

- using 2-step electrodeposition method. This helps us to improve the coverage of the fiber as cracks appear on the surface of the film (in 1-step deposition process); the improvement in the coverage results in high specific capacitance.
- hydrogenation of the MnO_x to induce oxygen vacancies and to improve the intrinsic kinetics of material which results in Mn_3O_4. Morphology and crystalline structure is investigated through FESEM, XRD, Raman and XPS (to study chemical composition) which confirms that structure is mixed oxide phases.
- synthesized $Na_{0.36}MnO_2$ through in-situ electrochemical oxidation which is confirmed by Raman and XPS. As $Na_{0.36}MnO_2$ is more conductive than MnO_x and results in higher specific capacitance. This has also allowed us to work in extended potential windows without deterioration of the material and show excellent cyclic stability.

6.1.3 Flexible fiber-shaped asymmetric supercapacitors

I have also assembled ASCs which has helped to fabricate device using electrodes material working in different voltage windows. PVA based gel-polymer electrolyte which allowed us to work in large window. As voltage windows are wide, both devices exhibited high specific capacitance and high energy density. The cyclic and bending stabilities of both the devices were also investigated and they have shown excellent performance of aging and bending stability. Our SCs exhibited very promising electrochemical performance with much enhanced energy and power densities as summarized in the Ragone plot in Figure 6.1 for full weight devices.

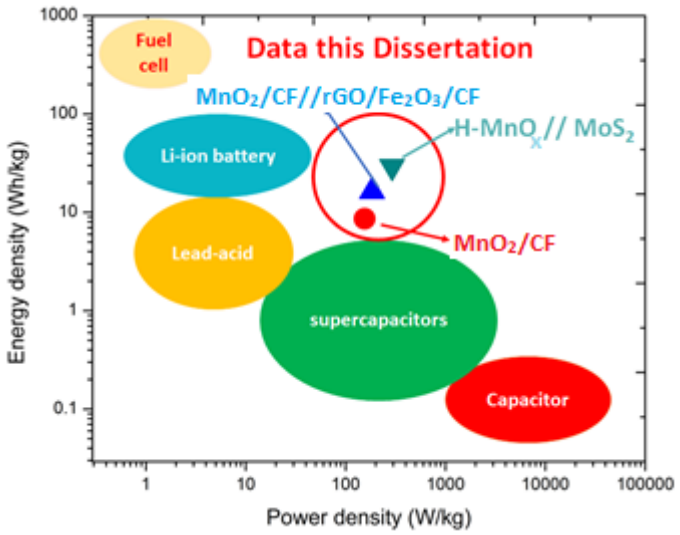

Figure 6. 1 Ragone plot shows the achieved energy and power densities of our devices including the SCs of MnO_2/CF and ASCs comprises H-MnO_x/CF//MoS_2/CF, MnO_x/CF//rGO/Fe_2O_3/CF electrodes respectively in gel-polymer electrolytes. All data are obtained from two electrodes SCs.

6.2 Future perspective

In order to further enhance the energy storage capacity of the SCs and fully exploit the potential of nanostructured materials such as MnO_2 based SCs and flexible substrate, the following guideline need to be considered.

1. To enhance the specific capacitance (F g^{-1}, F cm^{-1}) energy density and power density, need to explore other material such as manganese sulfide instead of MnO_x. Other potential candidates (materials) for high performance supercapacitor are, binary metal oxide or ternary metal oxide and sulfides such $CoMnO_x$ or $CoMnS_x$, $NiMnO_x$ or $NiMnS_x$, $MnVO_x$ or $MnVS_x$, $ZnMnO_x$ or ZnMnSx, $FeMnO_x$ or $FeMnS_x$ etc. These electrodes allow to work with extended potential windows which results in high specific capacitance and high energy and power densities. Furthermore, the Mn based layered intercalation structures such as: Li_xMnO_2, K_xMnO_2, etc. will significantly improve the energy storage capacity of the SCs due to their faster ionic diffusion with enhanced kinetics redox reactions than the conventional MnO_2 electrode materials and could be a potential candidate for flexible hybrid supercapacitors as cathode [223].

2. Encapsulation or packaging of these flexible fiber shaped supercapacitors is a big challenge in realization of the complete wearable supercapacitor an its integration in textiles. There is no study available on packaging for wearable supercapacitors. So, there is a need to design such packaging for flexible supercapacitors that when integrated in E-textiles, can sustain multiple uses, i.e., washability and durability. To the best of our knowledge,

there is no study in literature on multiple washable textiles integrated with electronic components. In general, multiple washing for the long-term usage of these wearable E-textiles is again a matter of concern which can be ensured by designing a suitable packaging for fiber shaped SCs [224].

3. Wearability is a critical aspect while designing wearable supercapacitor. Wearability prerequisites for textile energy storage devices are so far not well defined and standardized. Toxicity (material and electrolyte), flame resistance, mechanical flexibility, elasticity, abrasion resistance, moisture permeability, fatigue resistance, active material loading, thermal conductivity, and wettability are some basics requirements which need to be considered. Textile industry is well standardized to test different features of textile products, but textile energy storage devices have to setup new standards in order to be accepted by textile industry and clients. Wearability properties place critical obligation on the design of practical textile energy storage devices. Many 2D textile devices (non-woven) created by coating methods reported in literature are impermeable to moisture and cause uncomfortability while in direct contact with skin. It is also worth noting that little research has been conducted on the fatigue lifetime of textile energy storage devices under daily wearing conditions [225]. Significant research efforts will be required to create truly wearable textile energy storage devices.

4. The fundamental understanding of the surface redox reactions dominated energy storage mechanism of the MnO_2 supercapacitors is extremely important for the better synthesis and fabrication of MnO_2 materials in the future. The in-situ techniques such as TEM, XRD and Raman spectroscopy to directly observe the charge and discharge process and the associated evolution of the MnO_2 electrodes will discover new aspects towards the fundamental studies of SCs [226].

Reference

[1] M. Yu, Z. Wang, Y. Han, Y. Tong, X. Lu, and S. Yang, “Recent progress in the development of anodes for asymmetric supercapacitors,” *J. Mater. Chem. A*, vol. 4, no. 13, pp. 4634–4658, 2016.

[2] T. Cheng, Y. Zhang, W. Y. Lai, and W. Huang, “Stretchable thin-film electrodes for flexible electronics with high deformability and stretchability,” *Advanced Materials*. 2015.

[3] Y. Yang and W. Gao, “Wearable and flexible electronics for continuous molecular monitoring,” *Chem. Soc. Rev.*, 2018.

[4] M. Yu *et al.*, “Dual-Doped Molybdenum Trioxide Nanowires: A Bifunctional Anode for Fiber-Shaped Asymmetric Supercapacitors and Microbial Fuel Cells,” *Angew. Chemie - Int. Ed.*, vol. 55, no. 23, pp. 6762–6766, 2016.

[5] X. Xiao *et al.*, “Fiber-based all-solid-state flexible supercapacitors for self-powered systems,” *ACS Nano*, 2012.

[6] Y. Zhu *et al.*, “Carbon-based supercapacitors produced by activation of graphene.,” *Science*, 2011.

[7] J. Bae, M. K. Song, Y. J. Park, J. M. Kim, M. Liu, and Z. L. Wang, “Fiber supercapacitors made of nanowire-fiber hybrid structures for wearable/flexible energy storage,” *Angew. Chemie - Int. Ed.*, 2011.

[8] J. Collins, G. Gourdin, M. Foster, and D. Qu, “Carbon surface functionalities and SEI formation during Li intercalation,” *Carbon N. Y.*, vol. 92, pp. 193–244, 2015.

[9] S. Jung, C. Lauterbach, M. Strasser, and W. Weber, “ISSCC 2003 / SESSION 22 / TD : EMBEDDED TECHNOLOGIES / PAPER 22 . 1 Enabling Technologies for Disappearing Electronics in Smart Textiles • 2003 IEEE International Solid-State Circuits Conference,” *Wire*, vol. 1, no. June 2001, pp. 2–5, 2003.

[10] R. Kötz and M. Carlen, “Principles and applications of electrochemical capacitors,” *Electrochim. Acta*, vol. 45, no. 15–16, pp. 2483–2498, 2000.

[11] A. Burke and A. Burke, “Permalink,” *J. Power Sources*, vol. 91, pp. 37–50, 2000.

[12] J. Zhao, Y. Gao, J. Guo, L. Chu, and A. F. Burke, “Cycle life testing of lithium batteries: The effect of load-leveling,” *Int. J. Electrochem. Sci.*, vol. 13, no. 2, pp. 1773–1786, 2018.

[13] M. Jayalakshmi and K. Balasubramanian, “Simple capacitors to supercapacitors-an overview,” *Int. J. Electrochem. Sci*, vol. 3, no. November 2008, pp. 1196–1217, 2008.

[14] X. Peng, L. Peng, C. Wu, and Y. Xie, “Two dimensional nanomaterials for flexible supercapacitors,” *Chem. Soc. Rev.*, vol. 43, no. 10, pp. 3303–3323, 2014.

[15] Y. Wang, Y. Song, and Y. Xia, “Electrochemical capacitors: Mechanism, materials, systems, characterization and applications,” *Chem. Soc. Rev.*, vol. 45, no. 21, pp. 5925–5950, 2016.

[16] A. G. Pandolfo and A. F. Hollenkamp, “Carbon properties and their role in supercapacitors,” *J. Power Sources*, vol. 157, no. 1, pp. 11–27, 2006.

[17] B. Linnert, E. G., Md, “United States Patent Office,” pp. 2–4, 1952.
[18] R. A. Rightmire, “2. % 2.,” 1966.
[19] D. L. Boos, “Electrolytic capacitor having carbon paste electrodes,” 1970.
[20] M. F. Rose, “No Title.”
[21] J. Niu, W. G. Pell, and B. E. Conway, “Requirements for performance characterization of C double-layer supercapacitors: Applications to a high specific-area C-cloth material,” *J. Power Sources*, vol. 156, no. 2, pp. 725–740, 2006.
[22] B. E. Conway, “Transition from ‘Supercapacitor’ to ‘Battery’ Behavior in Electrochemical Energy Storage,” *J. Electrochem. Soc.*, vol. 138, no. 6, p. 1539, 1991.
[23] J. Libich, J. Máca, J. Vondrák, O. Čech, and M. Sedlaříková, “Supercapacitors: Properties and applications,” *Journal of Energy Storage*, vol. 17. pp. 224–227, 2018.
[24] M. Halper and J. Ellenbogen, “Supercapacitors: A brief overview,” *Rep. No. MP 05W0000272, …*, 2006.
[25] D. Yu *et al.*, “Emergence of fiber supercapacitors,” *Chem. Soc. Rev.*, vol. 44, no. 3, pp. 647–662, 2015.
[26] A. Chu and P. Braatz, “Comparison of commercial supercapacitors and high-power lithium-ion batteries for power-assist applications in hybrid electric vehicles: I. Initial characterization,” *J. Power Sources*, vol. 112, no. 1, pp. 236–246, 2002.
[27] E. Frackowiak, Q. Abbas, and F. Béguin, “Carbon/carbon supercapacitors,” *J. Energy Chem.*, vol. 22, no. 2, pp. 226–240, 2013.
[28] L. L. Zhang, R. Zhou, and X. S. Zhao, “Graphene-based materials as supercapacitor electrodes,” *J. Mater. Chem.*, 2010.
[29] D. L. Chapman, “LI. *A contribution to the theory of electrocapillarity*,” *Philos. Mag. Ser. 6*, 1913.
[30] O. Stern, “Zur theorie der elektrolytischen doppelschicht,” *Zeitschrift für Elektrochemie Angew. Phys. Chemie*, 1924.
[31] J. H. Lin, Y. Liu, and Q. M. Zhang, “Influence of the electrolyte film thickness on charge dynamics of ionic liquids in ionic electroactive devices,” *Macromolecules*, 2012.
[32] V. V. N. Obreja, “On the performance of supercapacitors with electrodes based on carbon nanotubes and carbon activated material-A review,” *Phys. E Low-Dimensional Syst. Nanostructures*, vol. 40, no. 7, pp. 2596–2605, 2008.
[33] G. Yu, X. Xie, L. Pan, Z. Bao, and Y. Cui, “Hybrid nanostructured materials for high-performance electrochemical capacitors,” *Nano Energy*, vol. 2, no. 2, pp. 213–234, 2013.
[34] S. Mohapatra, A. Acharya, and G. S. Roy, “The role of nanomaterial for the design of supercapacitor,” *Lat. Am. J. Phys. Educ.*, vol. 6, no. 3, pp. 380–384, 2012.
[35] Q.-Z. Zhang, D. Zhang, Z.-C. Miao, X.-L. Zhang, and S.-L. Chou, “Research Progress in MnO_2 -Carbon Based Supercapacitor Electrode Materials,” *Small*, vol. 14, no. 24, p. 1702883, 2018.
[36] J. W. Kim, V. Augustyn, and B. Dunn, “The effect of crystallinity on the rapid pseudocapacitive response of Nb2O5,” *Adv. Energy Mater.*, vol. 2, no. 1, pp.

141–148, 2012.
[37] A. Burke, “R&D considerations for the performance and application of electrochemical capacitors,” *Electrochim. Acta*, vol. 53, no. 3 SPEC. ISS., pp. 1083–1091, 2007.
[38] Y. Zhang, L. Li, H. Su, W. Huang, and X. Dong, “Binary metal oxide: Advanced energy storage materials in supercapacitors,” *J. Mater. Chem. A*, vol. 3, no. 1, pp. 43–59, 2015.
[39] K. Jurewicz, S. Delpeux, V. Bertagna, F. Béguin, and E. Frackowiak, “Supercapacitors from nanotubes/polypyrrole composites,” *Chem. Phys. Lett.*, vol. 347, no. 1–3, pp. 36–40, 2001.
[40] C. Peng, S. Zhang, D. Jewell, and G. Z. Chen, “Carbon nanotube and conducting polymer composites for supercapacitors,” *Prog. Nat. Sci.*, vol. 18, no. 7, pp. 777–788, 2008.
[41] A. Laforgue *et al.*, “Activated Carbon/Conducting Polymer Hybrid Supercapacitors,” *J. Electrochem. Soc.*, vol. 150, no. 5, p. A645, 2003.
[42] H. Li, L. Cheng, and Y. Xia, “A Hybrid Electrochemical Supercapacitor Based on a 5 V Li-Ion Battery Cathode and Active Carbon,” *Electrochem. Solid-State Lett.*, vol. 8, no. 9, p. A433, 2005.
[43] W. G. Pell, B. E. Conway, W. A. Adams, and J. De Oliveira, “Electrochemical efficiency in multiple discharge/recharge cycling of supercapacitors in hybrid EV applications,” *J. Power Sources*, vol. 80, no. 1, pp. 134–141, 1999.
[44] G. G. Amatucci, F. Badway, A. Du Pasquier, and T. Zheng, “An Asymmetric Hybrid Nonaqueous Energy Storage Cell,” *J. Electrochem. Soc.*, vol. 148, no. 8, p. A930, 2001.
[45] B. Zhao *et al.*, “A high-energy, long cycle-life hybrid supercapacitor based on graphene composite electrodes,” *Energy Storage Mater.*, vol. 7, pp. 32–39, 2017.
[46] A. J. Bard and L. R. Faulkner, *Fundamentals and Fundamentals and Applications*, vol. 8, no. c. 2015.
[47] S. Zhang and N. Pan, “Supercapacitors performance evaluation,” *Advanced Energy Materials*. 2015.
[48] T.-C. Liu, “Behavior of Molybdenum Nitrides as Materials for Electrochemical Capacitors,” *J. Electrochem. Soc.*, vol. 145, no. 6, p. 1882, 1998.
[49] K. Naoi and P. Simon, “New Materials and New Configurations for Advanced Electrochemical Capacitors,” *J. Electrochem. Soc.*, vol. 17, no. 1, pp. 34–37, 2008.
[50] C. Du and N. Pan, “Supercapacitors using carbon nanotubes films by electrophoretic deposition,” *J. Power Sources*, vol. 160, no. 2 SPEC. ISS., pp. 1487–1494, 2006.
[51] P. Simon and Y. Gogotsi, “Materials for electrochemical capacitors,” *Nat. Mater.*, vol. 7, no. 11, pp. 845–854, 2008.
[52] Y.-T. Kim *et al.*, “Drastic change of electric double layer capacitance by surface functionalization of carbon nanotubes,” *Appl. Phys. Lett.*, vol. 87, no. 23, p. 234106, 2005.
[53] P. R. Deshmukh, R. N. Bulakhe, S. N. Pusawale, S. D. Sartale, and C. D. Lokhande, “Polyaniline–RuO_2 composite for high performance supercapacitors: chemical synthesis and properties,” *RSC Adv.*, vol. 5, no.

36, pp. 28687–28695, 2015.
[54] H. Gao, J. Li, J. R. Miller, R. A. Outlaw, S. Butler, and K. Lian, “Solid-state electric double layer capacitors for ac line-filtering,” *Energy Storage Mater.*, vol. 4, pp. 66–70, 2016.
[55] H. Liu and G. Zhu, “The electrochemical capacitance of nanoporous carbons in aqueous and ionic liquids,” *J. Power Sources*, vol. 171, no. 2, pp. 1054–1061, 2007.
[56] A. Halama, B. Szubzda, and G. Pasciak, “Carbon aerogels as electrode material for electrical double layer supercapacitors - Synthesis and properties,” *Electrochim. Acta*, vol. 55, no. 25, pp. 7501–7505, 2010.
[57] E. Frackowiak, K. Metenier, V. Bertagna, and F. Beguin, “Supercapacitor electrodes from multiwalled carbon nanotubes,” *Appl. Phys. Lett.*, 2000.
[58] K. R. Prasad, K. Koga, and N. Miura, “Electrochemical deposition of nanostructured indium oxide: High-performance electrode material for redox supercapacitors,” *Chem. Mater.*, vol. 16, no. 10, pp. 1845–1847, 2004.
[59] G. Wang, L. Zhang, and J. Zhang, “A review of electrode materials for electrochemical supercapacitors,” *Chem. Soc. Rev.*, vol. 41, no. 2, pp. 797–828, 2012.
[60] J. Yan *et al.*, “Highly Oriented Two-Dimensional Formamidinium Lead Iodide Perovskite with a Small Bandgap of 1.51 eV,” *Mater. Chem. Front.*, 2017.
[61] G. A. Snook, P. Kao, and A. S. Best, “Conducting-polymer-based supercapacitor devices and electrodes,” *J. Power Sources*, vol. 196, no. 1, pp. 1–12, 2011.
[62] Y. Zhang *et al.*, “Progress of electrochemical capacitor electrode materials: A review,” *International Journal of Hydrogen Energy*. 2009.
[63] K. D. Fong, T. Wang, and S. K. Smoukov, “Multidimensional performance optimization of conducting polymer-based supercapacitor electrodes,” *Sustain. Energy Fuels*, vol. 00, pp. 1–18, 2017.
[64] M. S. Wu, Y. A. Huang, C. H. Yang, and J. J. Jow, “Electrodeposition of nanoporous nickel oxide film for electrochemical capacitors,” *Int. J. Hydrogen Energy*, vol. 32, no. 17, pp. 4153–4159, 2007.
[65] D. D. Zhao, S. J. Bao, W. J. Zhou, and H. L. Li, “Preparation of hexagonal nanoporous nickel hydroxide film and its application for electrochemical capacitor,” *Electrochem. commun.*, vol. 9, no. 5, pp. 869–874, 2007.
[66] M. Toupin, T. Brousse, and D. Bélanger, “Charge storage mechanism of MnO2 electrode used in aqueous electrochemical capacitor,” *Chem. Mater.*, vol. 16, no. 16, pp. 3184–3190, 2004.
[67] B. E. Conway, “Electrochemical Supercapacitors Scientific Fundamentals and Technological Applications,” *Journal of Chemical Information and Modeling*. 2013.
[68] X. Zhang, L. Ji, S. Zhang, and W. Yang, “Synthesis of a novel polyaniline-intercalated layered manganese oxide nanocomposite as electrode material for electrochemical capacitor,” *J. Power Sources*, vol. 173, no. 2 SPEC. ISS., pp. 1017–1023, 2007.
[69] T. Brousse, M. Toupin, R. Dugas, L. Athouël, O. Crosnier, and D. Bélanger, “Crystalline MnO[sub 2] as Possible Alternatives to Amorphous Compounds in Electrochemical Supercapacitors,” *J. Electrochem. Soc.*, vol. 153, no. 12,

p. A2171, 2006.
[70] Y. Liu, J. Wei, Y. Tian, and S. Yan, “The structure-property relationship of manganese oxides: Highly efficient removal of methyl orange from aqueous solution,” *J. Mater. Chem. A*, vol. 3, no. 37, pp. 19000–19010, 2015.
[71] B. Messaoudi, S. Joiret, M. Keddam, and H. Takenouti, “Anodic behaviour of manganese in alkaline medium,” *Electrochim. Acta*, vol. 46, no. 16, pp. 2487–2498, 2001.
[72] W. Wei, X. Cui, W. Chen, and D. G. Ivey, “Manganese oxide-based materials as electrochemical supercapacitor electrodes,” *Chem. Soc. Rev.*, vol. 40, no. 3, pp. 1697–1721, 2011.
[73] S.-C. Pang and M. A. Anderson, “Novel electrode materials for electrochemical capacitors: Part II. Material characterization of sol-gel-derived and electrodeposited manganese dioxide thin films,” *J. Mater. Res.*, vol. 15, no. 10, pp. 2096–2106, 2000.
[74] R. N. Reddy and R. G. Reddy, “Sol-gel MnO2as an electrode material for electrochemical capacitors,” *J. Power Sources*, vol. 124, no. 1, pp. 330–337, 2003.
[75] M. Toupin, T. Brousse, and D. Belanger, “Influence of Microstucture on the Charge Storage Properties of Chemically Synthesized Manganese Dioxide,” *Chem. Mater.*, vol. 14, no. 9, pp. 3946–3952, 2002.
[76] P. Ragupathy, H. N. Vasan, and N. Munichandraiah, “Synthesis and Characterization of Nano-MnO[sub 2] for Electrochemical Supercapacitor Studies,” *J. Electrochem. Soc.*, vol. 155, no. 1, p. A34, 2008.
[77] H. Y. Lee and J. B. Goodenough, “Supercapacitor Behavior with KCl Electrolyte,” *J. Solid State Chem.*, vol. 144, no. 1, pp. 220–223, 1999.
[78] S. Nagamuthu, S. Vijayakumar, and G. Muralidharan, “Synthesis of Mn_3O_4 /Amorphous Carbon Nanoparticles as Electrode Material for High Performance Supercapacitor Applications,” *Energy & Fuels*, vol. 27, no. 6, pp. 3508–3515, 2013.
[79] B. Babakhani and D. G. Ivey, “Anodic deposition of manganese oxide electrodes with rod-like structures for application as electrochemical capacitors,” *J. Power Sources*, vol. 195, no. 7, pp. 2110–2117, 2010.
[80] B. Babakhani and D. G. Ivey, “Effect of electrodeposition conditions on the electrochemical capacitive behavior of synthesized manganese oxide electrodes,” *J. Power Sources*, 2011.
[81] V. T. Le *et al.*, “Coaxial fiber supercapacitor using all-carbon material electrodes,” *ACS Nano*, vol. 7, no. 7, pp. 5940–5947, 2013.
[82] K. C. Tsay, L. Zhang, and J. Zhang, “Effects of electrode layer composition/thickness and electrolyte concentration on both specific capacitance and energy density of supercapacitor,” *Electrochim. Acta*, 2012.
[83] R. Gazia *et al.*, “Photodetection and piezoelectric response from hard and flexible sponge-like ZnO-based structures,” *Nano Energy*, 2013.
[84] V. Cauda, S. Stassi, A. Lamberti, M. Morello, C. Fabrizio Pirri, and G. Canavese, “Leveraging ZnO morphologies in piezoelectric composites for mechanical energy harvesting,” *Nano Energy*, 2015.
[85] N. Garino, A. Lamberti, R. Gazia, A. Chiodoni, and C. Gerbaldi, “Cycling behaviour of sponge-like nanostructured ZnO as thin-film Li-ion battery

anodes," *J. Alloys Compd.*, 2015.
[86] A. Jasmin, S. Porro, C. F. Pirri, C. Ricciardi, and A. Chiolerio, "Polymer coated ZnO nanowires for memristive devices," in *IEEE-NANO 2015 - 15th International Conference on Nanotechnology*, 2016.
[87] Z. L. Wang, "Zinc oxide nanostructures: Growth, properties and applications," *J. Phys. Condens. Matter*, 2004.
[88] T. Lu, Y. Zhang, H. Li, L. Pan, Y. Li, and Z. Sun, "Electrochemical behaviors of graphene–ZnO and graphene–SnO2 composite films for supercapacitors," *Electrochim. Acta*, 2010.
[89] M. Jayalakshmi, M. Palaniappa, and K. Balasubramanian, "Single Step Solution Combustion Synthesis of ZnO / carbon Composite and its Electrochemical Characterization for Supercapacitor Application," *Carbon N. Y.*, 2008.
[90] C. Pang, C. Lee, and K. Y. Suh, "Recent advances in flexible sensors for wearable and implantable devices," *Journal of Applied Polymer Science*. 2013.
[91] M. D. Lima *et al.*, "Biscrolling nanotube sheets and functional guests into yarns," *Science (80-.).*, 2011.
[92] C. Meng, C. Liu, L. Chen, C. Hu, and S. Fan, "Highly flexible and all-solid-state paperlike polymer supercapacitors," *Nano Lett.*, vol. 10, no. 10, pp. 4025–4031, 2010.
[93] X. Cai, M. Peng, X. Yu, Y. Fu, and D. Zou, "Flexible planar/fiber-architectured supercapacitors for wearable energy storage," *J. Mater. Chem. C*, 2014.
[94] D. P. Dubal, N. R. Chodankar, D. H. Kim, and P. Gomez-Romero, "Towards flexible solid-state supercapacitors for smart and wearable electronics," *Chem. Soc. Rev.*, vol. 47, no. 6, pp. 2065–2129, 2018.
[95] Y. Cheng, S. Lu, H. Zhang, C. V Varanasi, and J. Liu, "Synergistic E ff ects from Graphene and Carbon Nanotubes Enable Flexible and Robust Electrodes for High-Performance Supercapacitors," *Nano Lett.*, vol. 12, no. 8, p. 4206−4211, 2012.
[96] Y. He *et al.*, "Freestanding three-dimensional graphene/Mno2 composite networks as ultralight and flexible supercapacitor electrodes," *ACS Nano*, vol. 7, no. 1, pp. 174–182, 2013.
[97] D. Feng *et al.*, "Free-Standing Mesoporous Carbon Thin Films with Highly Ordered Pore Architectures for Nanodevices.pdf," *J. Am. Chem. Soc.*, vol. 133, pp. 15148–15156, 2011.
[98] V. L. Pushparaj *et al.*, "Flexible energy storage devices based on nanocomposite paper.," *Proc. Natl. Acad. Sci. U. S. A.*, vol. 104, no. 34, pp. 13574–7, 2007.
[99] Z. Cao and B. Wei, "A perspective: Carbon nanotube macro-films for energy storage," *Energy Environ. Sci.*, vol. 6, no. 11, pp. 3183–3201, 2013.
[100] J. Yu *et al.*, "Metallic Fabrics as the Current Collector for High-Performance Graphene-Based Flexible Solid-State Supercapacitor," *ACS Appl. Mater. Interfaces*, vol. 8, no. 7, pp. 4724–4729, 2016.
[101] A. Lamberti, M. Fontana, S. Bianco, and E. Tresso, "Flexible solid-state CuxO-based pseudo-supercapacitor by thermal oxidation of copper foils," *Int. J. Hydrogen Energy*, vol. 41, no. 27, pp. 11700–11708, 2016.
[102] Y. Wang *et al.*, "Polyhedron-core/double-shell CuO@C@MnO2decorated

nickel foam for high performance all-solid-state supercapacitors," *Electrochim. Acta*, vol. 246, no. February 2018, pp. 1065–1074, 2017.
[103] H. Xia *et al.*, "Hierarchically Structured Co 3 O 4 @Pt@MnO 2 Nanowire Arrays for High-Performance Supercapacitors," *Sci. Rep.*, vol. 3, pp. 1–8, 2013.
[104] J. G. Wang, Y. Yang, Z. H. Huang, and F. Kang, "A high-performance asymmetric supercapacitor based on carbon and carbon-MnO2nanofiber electrodes," *Carbon N. Y.*, vol. 61, pp. 190–199, 2013.
[105] N. R. Chodankar, D. P. Dubal, A. C. Lokhande, and C. D. Lokhande, "Ionically conducting PVA-LiClO4gel electrolyte for high performance flexible solid state supercapacitors," *J. Colloid Interface Sci.*, vol. 460, pp. 370–376, 2015.
[106] Y. He *et al.*, "Freestanding three-dimensional graphene/Mno2 composite networks as ultralight and flexible supercapacitor electrodes," *ACS Nano*, 2013.
[107] J. G. Wang, Y. Yang, Z. H. Huang, and F. Kang, "Effect of temperature on the pseudo-capacitive behavior of freestanding MnO2@carbon nanofibers composites electrodes in mild electrolyte," *J. Power Sources*, vol. 224, pp. 86–92, 2013.
[108] D. Qi, Y. Liu, Z. Liu, L. Zhang, and X. Chen, "Design of Architectures and Materials in In-Plane Micro-supercapacitors: Current Status and Future Challenges," *Adv. Mater.*, vol. 29, no. 5, pp. 1–19, 2017.
[109] N. Alayo, C. Fernández-Sánchez, A. Baldi, J. P. Esquivel, X. Borrisé, and F. Pérez-Murano, "Gold interdigitated nanoelectrodes as a sensitive analytical tool for selective detection of electroactive species via redox cycling," *Microchim. Acta*, 2016.
[110] C. Meng, J. Maeng, S. W. M. John, and P. P. Irazoqui, "Ultrasmall integrated 3d micro-supercapacitors solve energy storage for miniature devices," *Adv. Energy Mater.*, vol. 4, no. 7, pp. 1–7, 2014.
[111] L. Liu, B. Shen, D. Jiang, R. Guo, L. Kong, and X. Yan, "Watchband-Like Supercapacitors with Body Temperature Inducible Shape Memory Ability," *Adv. Energy Mater.*, vol. 6, no. 16, 2016.
[112] K. Jost, G. Dion, and Y. Gogotsi, "Textile energy storage in perspective," *Journal of Materials Chemistry A*. 2014.
[113] L. Li, Z. Wu, S. Yuan, and X.-B. Zhang, "Advances and challenges for flexible energy storage and conversion devices and systems," *Energy Environ. Sci.*, 2014.
[114] T. Huang *et al.*, "Flexible high performance wet-spun graphene fiber supercapacitors," *RSC Adv.*, 2013.
[115] L. Gao *et al.*, "Flexible Fiber-Shaped Supercapacitor Based on Nickel-Cobalt Double Hydroxide and Pen Ink Electrodes on Metallized Carbon Fiber," *ACS Appl. Mater. Interfaces*, 2017.
[116] A. Rafique, S. Bianco, M. Fontana, C. F. Pirri, and A. Lamberti, "Flexible wire-based electrodes exploiting carbon/ZnO nanocomposite for wearable supercapacitors," *Ionics (Kiel).*, vol. 23, no. 7, 2017.
[117] N. J. Welham, V. Berbenni, and P. G. Chapman, "Effect of extended ball milling on graphite," *J. Alloys Compd.*, 2003.
[118] Y. Saito, T. Yoshikawa, S. Bandow, M. Tomita, and T. Hayashi, "Interlayer spacings in carbon nanotubes," *Phys. Rev. B*, 1993.

[119] K. A. Alim, V. A. Fonoberov, M. Shamsa, and A. A. Balandin, “Micro-Raman investigation of optical phonons in ZnO nanocrystals,” *J. Appl. Phys.*, 2005.
[120] X. Zhao *et al.*, “Frequency-dependence of electric double layer capacitance of TiO2-based composite nanotube arrays,” *J. Electroanal. Chem.*, 2016.
[121] X. Li, J. Wang, F. Ge, S. Komarneni, and Z. Cai, “Facile fabrication of freestanding three-dimensional composites for supercapacitors,” *Chem. Commun.*, 2016.
[122] M. Selvakumar, D. Krishna Bhat, A. Manish Aggarwal, S. Prahladh Iyer, and G. Sravani, “Nano ZnO-activated carbon composite electrodes for supercapacitors,” *Phys. B Condens. Matter*, 2010.
[123] Y. Zhang, H. Li, L. Pan, T. Lu, and Z. Sun, “Capacitive behavior of graphene-ZnO composite film for supercapacitors,” *J. Electroanal. Chem.*, 2009.
[124] T. Lu *et al.*, “Microwave-assisted synthesis of graphene-ZnO nanocomposite for electrochemical supercapacitors,” *J. Alloys Compd.*, 2011.
[125] J. S. Bonso *et al.*, “Exfoliated graphite nanoplatelets-V 2O 5 nanotube composite electrodes for supercapacitors,” *J. Power Sources*, 2012.
[126] K. Jost *et al.*, “Knitted and screen printed carbon-fiber supercapacitors for applications in wearable electronics,” *Energy Environ. Sci.*, 2013.
[127] J. Ren, W. Bai, G. Guan, Y. Zhang, and H. Peng, “Flexible and weaveable capacitor wire based on a carbon nanocomposite fiber,” *Adv. Mater.*, 2013.
[128] V. T. Le *et al.*, “Coaxial fiber supercapacitor using all-carbon material electrodes,” *ACS Nano*, 2013.
[129] M. Zhi, C. Xiang, J. Li, M. Li, and N. Wu, “Nanostructured carbon-metal oxide composite electrodes for supercapacitors: A review,” *Nanoscale*, 2013.
[130] Rusi and S. R. Majid, “Electrodeposited Mn3O4-NiO-Co3O4 as a composite electrode material for electrochemical capacitor,” *Electrochim. Acta*, 2015.
[131] G. P. Wang, L. Zhang, and J. J. Zhang, “A review of electrode materials for electrochemical supercapacitors,” *Chem. Soc. Rev.*, 2012.
[132] Y. Luo *et al.*, “Self-assembly of well-ordered whisker-like manganese oxide arrays on carbon fiber paper and its application as electrode material for supercapacitors,” *J. Mater. Chem.*, 2012.
[133] S. Zhu, H. Zhou, M. Hibino, I. Honma, and M. Ichihara, “Synthesis of MnO2 Nanoparticles Confined in Ordered Mesoporous Carbon Using a Sonochemical Method,” *Adv. Funct. Mater.*, 2005.
[134] F. Su and M. Miao, “Asymmetric carbon nanotube-MnO2two-ply yarn supercapacitors for wearable electronics,” *Nanotechnology*, 2014.
[135] K. Wang, Q. Meng, Y. Zhang, Z. Wei, and M. Miao, “High-performance two-ply yarn supercapacitors based on carbon nanotubes and polyaniline nanowire arrays,” *Adv. Mater.*, 2013.
[136] A. Rafique *et al.*, “Highly Uniform Anodically Deposited Film of MnO2Nanoflakes on Carbon Fibers for Flexible and Wearable Fiber-Shaped Supercapacitors,” *ACS Appl. Mater. Interfaces*, 2017.
[137] D. Pletcher, “A first course in electrode processes,” *Journal of Applied Electrochemistry*. 2009.
[138] A. Massa, S. Hernández, A. Lamberti, C. Galletti, N. Russo, and D. Fino, “Electro-oxidation of phenol over electrodeposited MnOxnanostructures and the role of a TiO2nanotubes interlayer,” *Appl. Catal. B Environ.*, 2017.
[139] S. Hernández *et al.*, “Spin-coated vs. electrodeposited Mn oxide films as

water oxidation catalysts," *Materials (Basel).*, 2016.
[140] A. Ramírez and P. Hillebrand, "Evaluation of MnO x, Mn2O3, and Mn3O4 Electrodeposited Films for the Oxygen Evolution Reaction of Water," *J. Phys. Chem. C*, 2014.
[141] R. P. Gupta and S. K. Sen, "Calculation of multiplet structure of core p - vacancy levels. II," *Phys. Rev. B*, 1975.
[142] M. Oku, K. Hirokawa, and S. Ikeda, "X-ray photoelectron spectroscopy of manganese-oxygen systems," *J. Electron Spectros. Relat. Phenomena*, 1975.
[143] M. C. Biesinger, B. P. Payne, A. P. Grosvenor, L. W. M. Lau, A. R. Gerson, and R. S. C. Smart, "Resolving surface chemical states in XPS analysis of first row transition metals, oxides and hydroxides: Cr, Mn, Fe, Co and Ni," *Appl. Surf. Sci.*, 2011.
[144] H. W. Nesbitt and D. Banerjee, "Interpretation of XPS Mn(2p) spectra of Mn oxyhydroxides and constraints on the mechanism of MnO2precipitation," *Am. Mineral.*, 1998.
[145] M. Huang *et al.*, "Merging of kirkendall growth and ostwald ripening: CuO@MnO2core-shell architectures for asymmetric supercapacitors," *Sci. Rep.*, 2014.
[146] A. T. Kozakov *et al.*, "Valence state of manganese and iron ions in La<inf>1-x</inf>A<inf>x</inf>MnO<inf>3</inf> (A = Ca, Sr) and Bi<inf>1-x</inf>Sr<inf>x</inf>FeO<inf>3</inf> systems from Mn2p, Mn3s, Fe2p and Fe3s X-ray photoelectron spectra. Effect of delocalization on Fe3s sp," *J. Alloys Compd.*, 2015.
[147] G. A. M. Ali, M. M. Yusoff, Y. H. Ng, H. N. Lim, and K. F. Chong, "Potentiostatic and galvanostatic electrodeposition of manganese oxide for supercapacitor application: A comparison study," *Curr. Appl. Phys.*, 2015.
[148] G. A. M. Ali, M. M. Yusoff, H. Algarni, and K. F. Chong, "One-step electrosynthesis of MnO2/rGO nanocomposite and its enhanced electrochemical performance," *Ceram. Int.*, 2018.
[149] T. Brousse, D. Belanger, and J. W. Long, "To Be or Not To Be Pseudocapacitive?," *J. Electrochem. Soc.*, 2015.
[150] Chuizhou Meng, "A Review of Flexible and Weaveable Fiber-Like Supercapacitors," *J. Postdr. Res.*, 2013.
[151] Y. Zhang *et al.*, "Carbon nanotube-zinc oxide electrode and gel polymer electrolyte for electrochemical supercapacitors," *Journal of Alloys and Compounds*. 2009.
[152] Z. S. Wu, W. Ren, D. W. Wang, F. Li, B. Liu, and H. M. Cheng, "High-energy MnO2 nanowire/graphene and graphene asymmetric electrochemical capacitors," *ACS Nano*, 2010.
[153] M. S. Wu, Z. S. Guo, and J. J. Jow, "Highly regulated electrodeposition of needle-like manganese oxide nanofibers on carbon fiber fabric for electrochemical capacitors," *J. Phys. Chem. C*, 2010.
[154] K. Guo, Y. Ma, H. Li, and T. Zhai, "Flexible Wire-Shaped Supercapacitors in Parallel Double Helix Configuration with Stable Electrochemical Properties under Static/Dynamic Bending," *Small*, 2016.
[155] Y. Huang *et al.*, "Magnetic-Assisted, Self-Healable, Yarn-Based Supercapacitor," *ACS Nano*, vol. 9, no. 6, pp. 6242–6251, 2015.
[156] Y. Meng *et al.*, "All-graphene core-sheath microfibers for all-solid-state,

stretchable fibriform supercapacitors and wearable electronic textiles," *Adv. Mater.*, 2013.
[157] J. Ren *et al.*, "Twisting carbon nanotube fibers for both wire-shaped micro-supercapacitor and micro-battery," *Adv. Mater.*, 2013.
[158] Z. Yang, J. Deng, X. Chen, J. Ren, and H. Peng, "A highly stretchable, fiber-shaped supercapacitor," *Angew. Chemie - Int. Ed.*, 2013.
[159] Q. Chen *et al.*, "MnO2-modified hierarchical graphene fiber electrochemical supercapacitor," *J. Power Sources*, 2014.
[160] A. Russo, B. Y. Ahn, J. J. Adams, E. B. Duoss, J. T. Bernhard, and J. A. Lewis, "Pen-on-paper flexible electronics," *Adv. Mater.*, 2011.
[161] H. Yu *et al.*, "Improvement of the performance for quasi-solid-state supercapacitor by using PVA-KOH-KI polymer gel electrolyte," *Electrochim. Acta*, 2011.
[162] T. Zhai *et al.*, "Oxygen vacancies enhancing capacitive properties of MnO2nanorods for wearable asymmetric supercapacitors," *Nano Energy*, 2014.
[163] N. Jabeen, A. Hussain, Q. Xia, S. Sun, J. Zhu, and H. Xia, "High-Performance 2.6 V Aqueous Asymmetric Supercapacitors based on In Situ Formed Na0.5MnO2Nanosheet Assembled Nanowall Arrays," *Adv. Mater.*, 2017.
[164] K. L. Holland and J. R. Walker, "Crystal structure modeling of a highly disordered potassium birnessite," *Clays Clay Miner.*, 1996.
[165] Q. FENG, E.-H. SUN, K. YANAGISAWA, and N. YAMASAKI, "Synthesis of Birnessite-Type Sodium Manganese Oxides by Solution Reaction and Hydrothermal Methods," *J. Ceram. Soc. Japan*, 1997.
[166] H. Xia, Y. Wang, J. Lin, and L. Lu, "Hydrothermal synthesis of MnO2/CNT nanocomposite with a CNT core/porous MnO2sheath hierarchy architecture for supercapacitors," *Nanoscale Res. Lett.*, 2012.
[167] J. Zhang *et al.*, "δ-MnO<inf>2</inf>/holey graphene hybrid fiber for all-solid-state supercapacitor," *J. Mater. Chem. A*, 2016.
[168] N. Nagarajan and I. Zhitomirsky, "Cathodic electrosynthesis of iron oxide films for electrochemical supercapacitors," *J. Appl. Electrochem.*, 2006.
[169] H. Y. Lee, V. Manivannan, and J. B. Goodenough, "Electrochemical capacitors with KCl electrolyte," *Comptes Rendus l'Academie des Sci. - Ser. IIc Chem.*, vol. 2, no. 11–13, pp. 565–577, 1999.
[170] J. P. Zheng and T. R. Jow, "A New Charge Storage Mechanism for Electrochemical Capacitors," *J. Electrochem. Soc.*, 1995.
[171] R. Liu and B. L. Sang, "MnO2/poly(3,4-ethylenedioxythiophene) coaxial nanowires by one-step coelectrodeposition for electrochemical energy storage," *J. Am. Chem. Soc.*, 2008.
[172] Q. Huang, X. Wang, and J. Li, "Characterization and performance of hydrous manganese oxide prepared by electrochemical method and its application for supercapacitors," *Electrochim. Acta*, 2006.
[173] V. Subramanian, H. Zhu, and B. Wei, "Nanostructured MnO2: Hydrothermal synthesis and electrochemical properties as a supercapacitor electrode material," *J. Power Sources*, 2006.
[174] J. Wang, J. Polleux, J. Lim, and B. Dunn, "Pseudocapacitive Contributions to Electrochemical Energy Storage in TiO2 (Anatase) Nanoparticles," *J. Phys. Chem. C*, 2007.

[175] M. P. Yeager *et al.*, “Pseudocapacitive hausmannite nanoparticles with (101) facets: Synthesis, characterization, and charge-transfer mechanism,” *ChemSusChem*, 2013.
[176] M. Aghazadeh, M. Ghannadi Maragheh, M. R. Ganjali, and P. Norouzi, “One-step electrochemical preparation and characterization of nanostructured hydrohausmannite as electrode material for supercapacitors,” *RSC Adv.*, 2016.
[177] M. K. Song *et al.*, “Anomalous pseudocapacitive behavior of a nanostructured, mixed-valent manganese oxide film for electrical energy storage,” *Nano Lett.*, 2012.
[178] X. Han, T. Zhang, J. Du, F. Cheng, and J. Chen, “Porous calcium-manganese oxide microspheres for electrocatalytic oxygen reduction with high activity,” *Chem. Sci.*, 2013.
[179] Y. Liu *et al.*, “High-performance aqueous sodium-ion batteries with K0.27MnO2cathode and their sodium storage mechanism,” *Nano Energy*, 2014.
[180] C. Julien, M. Massot, R. Baddour-Hadjean, S. Franger, S. Bach, and J. P. Pereira-Ramos, “Raman spectra of birnessite manganese dioxides,” *Solid State Ionics*, 2003.
[181] S. Komaba, T. Tsuchikawa, A. Ogata, N. Yabuuchi, D. Nakagawa, and M. Tomita, “Nano-structured birnessite prepared by electrochemical activation of manganese(III)-based oxides for aqueous supercapacitors,” *Electrochim. Acta*, 2012.
[182] J. Y. Li *et al.*, “P2-type Na0.53MnO2nanorods with superior rate capabilities as advanced cathode material for sodium ion batteries,” *Chem. Eng. J.*, 2017.
[183] Y. Dai, K. Wang, and J. Xie, “From spinel Mn3O4to layered nanoarchitectures using electrochemical cycling and the distinctive pseudocapacitive behavior,” *Appl. Phys. Lett.*, 2007.
[184] Y. Liu *et al.*, “High-performance aqueous sodium-ion batteries with K0.27MnO2 cathode and their sodium storage mechanism,” *Nano Energy*, 2014.
[185] L. Athouël, F. Moser, R. Dugas, O. Crosnier, D. Bélanger, and T. Brousse, “Variation of the MnO2 birnessite structure upon charge/discharge in an electrochemical supercapacitor electrode in aqueous Na2SO 4 electrolyte,” *J. Phys. Chem. C*, 2008.
[186] A. A. Radhiyah, M. I. Izwan, V. Baiju, C. K. Feng, I. Jamil, and R. Jose, “Doubling of electrochemical parameters via the pre-intercalation of Na+ in layered MnO2 nanoflakes compared to a-MnO2 nanorods.,” *RSC Adv.*, 2015.
[187] C. Wei, C. Xu, B. Li, H. Du, D. Nan, and F. Kang, “Anomalous effect of K ions on electrochemical capacitance of amorphous MnO2,” *J. Power Sources*, 2013.
[188] Q. Qu *et al.*, “Electrochemical performance of MnO2 nanorods in neutral aqueous electrolytes as a cathode for asymmetric supercapacitors,” *J. Phys. Chem. C*, 2009.
[189] N. Jabeen, Q. Xia, S. V. Savilov, S. M. Aldoshin, Y. Yu, and H. Xia, “Enhanced Pseudocapacitive Performance of α-MnO2by Cation Preinsertion,” *ACS*

Appl. Mater. Interfaces, 2016.
[190] Z. Dai, C. Peng, J. H. Chae, K. C. Ng, and G. Z. Chen, "Cell voltage versus electrode potential range in aqueous supercapacitors," *Sci. Rep.*, 2015.
[191] J. W. Long, D. Bélanger, T. Brousse, W. Sugimoto, M. B. Sassin, and O. Crosnier, "Asymmetric electrochemical capacitors-Stretching the limits of aqueous electrolytes," *MRS Bull.*, 2011.
[192] Y. Gao *et al.*, "One-step solvothermal synthesis of quasi-hexagonal Fe2O3 nanoplates/graphene composite as high performance electrode material for supercapacitor," *Electrochim. Acta*, 2016.
[193] D. L. A. de Faria, S. Venâncio Silva, and M. T. de Oliveira, "Raman microspectroscopy of some iron oxides and oxyhydroxides," *J. Raman Spectrosc.*, 1997.
[194] M. Filippi and L. Calliari, "Measuring the energy of the graphite p + s plasmon peak," *Surf. Interface Anal.*, 2006.
[195] J. A. Leiro, M. H. Heinonen, T. Laiho, and I. G. Batirev, "Core-level XPS spectra of fullerene, highly oriented pyrolitic graphite, and glassy carbon," *J. Electron Spectros. Relat. Phenomena*, 2003.
[196] Y. S. Hu, A. Kleiman-Shwarsctein, A. J. Forman, D. Hazen, J. N. Park, and E. W. McFarland, "Pt-doped α-Fe2O3 thin films active for photoelectrochemical water splitting," *Chem. Mater.*, 2008.
[197] T. Yamashita and P. Hayes, "Analysis of XPS spectra of Fe2+ and Fe3+ ions in oxide materials," *Appl. Surf. Sci.*, 2008.
[198] H. Wang, Z. Xu, H. Yi, H. Wei, Z. Guo, and X. Wang, "One-step preparation of single-crystalline Fe2O3 particles/graphene composite hydrogels as high performance anode materials for supercapacitors," *Nano Energy*, 2014.
[199] S. Zhang, B. Yin, Z. Wang, and F. Peter, "Super long-life all solid-state asymmetric supercapacitor based on NiO nanosheets and α-Fe2O3nanorods," *Chem. Eng. J.*, 2016.
[200] Y. Wei *et al.*, "Facile synthesis of self-assembled ultrathin α-FeOOH nanorod/graphene oxide composites for supercapacitors," *J. Colloid Interface Sci.*, 2017.
[201] M. G. Verde, H. Liu, K. J. Carroll, L. Baggetto, G. M. Veith, and Y. S. Meng, "Effect of morphology and manganese valence on the voltage fade and capacity retention of Li[Li2/12Ni3/12Mn7/12]O2," *ACS Appl. Mater. Interfaces*, 2014.
[202] A. Gigot *et al.*, "Mixed 1T-2H Phase MoS2/Reduced Graphene Oxide as Active Electrode for Enhanced Supercapacitive Performance," *ACS Appl. Mater. Interfaces*, 2016.
[203] M. Acerce, D. Voiry, and M. Chhowalla, "Metallic 1T phase MoS2 nanosheets as supercapacitor electrode materials," *Nat. Nanotechnol.*, 2015.
[204] S. A. Ansari, H. Fouad, S. G. Ansari, M. P. Sk, and M. H. Cho, "Mechanically exfoliated MoS2sheet coupled with conductive polyaniline as a superior supercapacitor electrode material," *J. Colloid Interface Sci.*, 2017.
[205] J. N. Broughton and M. J. Brett, "Variations in MnO2 electrodeposition for electrochemical capacitors," *Electrochim. Acta*, 2005.
[206] S. Chou, F. Cheng, and J. Chen, "Electrodeposition synthesis and electrochemical properties of nanostructured ??-MnO2 films," *J. Power*

Sources, 2006.
[207] M. S. Wu, “Electrochemical capacitance from manganese oxide nanowire structure synthesized by cyclic voltammetric electrodeposition,” *Appl. Phys. Lett.*, 2005.
[208] M. W. Xu, D. D. Zhao, S. J. Bao, and H. L. Li, “Mesoporous amorphous MnO2 as electrode material for supercapacitor,” *J. Solid State Electrochem.*, 2007.
[209] S. S. Karade, D. P. Dubal, and B. R. Sankapal, “MoS<inf>2</inf> ultrathin nanoflakes for high performance supercapacitors: Room temperature chemical bath deposition (CBD),” *RSC Adv.*, 2016.
[210] X. Liu, K. Liu, W. Zhou, L. Li, K. Zhou, and S. Chen, “High-Performance Capacitors Based on MoS₂ Nanosheets Supported on Carbon Fibers,” *Sci. Adv. Mater.*, 2015.
[211] S. Qin, W. Lei, D. Liu, and Y. Chen, “In-situ and tunable nitrogen-doping of MoS2nanosheets,” *Sci. Rep.*, 2014.
[212] H. Lin, X. Chen, H. Li, M. Yang, and Y. Qi, “Hydrothermal synthesis and characterization of MoS2 nanorods,” *Mater. Lett.*, 2010.
[213] W. Yan *et al.*, “Mesoporous manganese oxide nanowires for high-capacity, high-rate, hybrid electrical energy storage,” *ACS Nano*, 2011.
[214] K. Brezesinski *et al.*, “Pseudocapacitive contributions to charge storage in highly ordered mesoporous group v transition metal oxides with iso-oriented layered nanocrystalline domains,” *J. Am. Chem. Soc.*, 2010.
[215] M. Wu, G. A. Snook, G. Z. Chen, and D. J. Fray, “Redox deposition of manganese oxide on graphite for supercapacitors,” *Electrochem. commun.*, 2004.
[216] J. M. Soon and K. P. Loh, “Electrochemical Double-Layer Capacitance of MoS[sub 2] Nanowall Films,” *Electrochem. Solid-State Lett.*, 2007.
[217] S. J. Rowley-Neale, D. A. C. Brownson, G. C. Smith, D. A. G. Sawtell, P. J. Kelly, and C. E. Banks, “2D nanosheet molybdenum disulphide (MoS_2) modified electrodes explored towards the hydrogen evolution reaction,” *Nanoscale*, 2015.
[218] H. Zhu *et al.*, “Design of two-dimensional, ultrathin MoS2 nanoplates fabricated within one-dimensional carbon nanofibers with thermosensitive morphology: High-performance electrocatalysts for the hydrogen evolution reaction,” *ACS Appl. Mater. Interfaces*, 2014.
[219] D. Voiry *et al.*, “Conducting MoS_2 nanosheets as catalysts for hydrogen evolution reaction.,” *Nano Lett.*, 2013.
[220] G. Li, D. Zhang, Y. Yu, S. Huang, W. Yang, and L. Cao, “Activating MoS 2 for pH-Universal Hydrogen Evolution Catalysis,” *J. Am. Chem. Soc.*, 2017.
[221] B. Zhang *et al.*, “Unraveling the different charge storage mechanism in T and H phases of MoS2,” *Electrochim. Acta*, 2016.
[222] M. F. Dupont and S. W. Donne, “Separating Faradaic and Non-Faradaic Charge Storage Contributions in Activated Carbon Electrochemical Capacitors Using Electrochemical Methods: I. Step Potential Electrochemical Spectroscopy,” *J. Electrochem. Soc.*, 2015.
[223] L. Mai *et al.*, “Fast ionic diffusion-enabled nanoflake electrode by spontaneous electrochemical pre-intercalation for high-performance supercapacitor,” *Sci. Rep.*, 2013.
[224] V. Kaushik *et al.*, “Textile-Based Electronic Components for Energy

Applications: Principles, Problems, and Perspective," *Nanomaterials*, 2015.
[225] W. Weng *et al.*, "Failure mechanism in fiber-shaped electrodes for lithium-ion batteries," *J. Mater. Chem. A*, 2015.
[226] T. D. Hatchard and J. R. Dahn, "In Situ XRD and Electrochemical Study of the Reaction of Lithium with Amorphous Silicon," *J. Electrochem. Soc.*, 2004.